Title

Single-Walled Carbon Nanotube-Based Biosensors: Engineering Near-Infrared Fluorescent Nanosensors for Oxytocin Imaging in the Brain

Author

Navarro, Nicole

Publication Date

2022

Single-Walled Carbon Nanotube-Based Biosensors: Engineering Near-Infrared Fluorescent Nanosensors for Oxytocin Imaging in the Brain

By

Nicole Navarro

A dissertation submitted in partial satisfaction of the

requirements for the degree of

Doctor of Philosophy

in

Chemistry

in the

Graduate Division

of the

University of California, Berkeley

Committee in charge:

Professor Markita P. Landry, Co-Chair
Professor Matthew B. Francis, Co-Chair
Professor Sabeeha Merchant
Professor Evan Miller

Fall 2022

Single-Walled Carbon Nanotube-Based Biosensors: Engineering Near-Infrared Fluorescent Nanosensors for Oxytocin Imaging in the Brain

Nicole Navarro

Abstract

Single-Walled Carbon Nanotube-Based Biosensors: Engineering Near-Infrared Fluorescent Nanosensors for Oxytocin Imaging in the Brain

by

Nicole Navarro

Doctor of Philosophy in Chemistry

University of California, Berkeley

Professor Markita P. Landry, Co-Chair

Professor Matthew B. Francis, Co-Chair

Oxytocin is a nonapeptide that plays an essential role in regulating our social and reproductive behavior. Synthesized predominantly in the hypothalamus, oxytocin functions both peripherally as a peptide hormone and centrally as a neuropeptide. Its actions in the brain and body are distinct but complementary. When released throughout the brain, neuropeptide oxytocin regulates complex emotions and social behaviors such as social recognition, pair and maternal bonding, and stress mitigation. Oxytocin is also involved in the pathogenesis of various social disorders, including generalized social anxiety disorder and autism spectrum disorder. Treatment with oxytocin has been demonstrated to alleviate some of the social impairments associated with these disorders. Oxytocin has thus garnered interest as both a potential therapy and therapeutic target. While neuropeptide oxytocin is known to play a critical role in regulating our social lives, our understanding of its function remains incomplete because we lack the tools to directly probe oxytocin signaling at the spatiotemporal resolution requisite to elucidate oxytocinergic communication. The gold standard for oxytocin detection involves invasive sampling via microdialysis followed by a quantification assay such as ELISA. These methods have been used extensively to study oxytocin but suffer from poor spatial and temporal resolution and significant variability across sample processing and quantification method. Recently, an optogenetic platform was developed to enable labeling of oxytocin sensitive neurons. This platform lacks specificity against oxytocin's structural analogue, vasopressin, and is transcription-dependent, and therefore cannot image oxytocin in real-time. Other OXTR-dependent imaging probes continue to face challenges related to vasopressin interference.

Real-time imaging platforms are required to fully characterize oxytocin function, and toward this end, we have developed two sensitive and reversible oxytocin nanosensors capable of imaging oxytocin in the brain. Both probes leverage the inherent tissue-transparent fluorescence of single-walled carbon nanotubes (SWCNT). SWCNT are biocompatible and photostable nanomaterials that can be functionalized with molecular recognition elements to develop sensors for targets of interest. As SWCNT photophysics is exciton-based, SWCNT fluorescence is modulated by the surrounding dielectric environment. We leveraged this dielectric sensitive to develop probes that increase in fluorescence upon interacting with oxytocin. In this dissertation, SWCNT, their optical properties, and their utility in bioimaging application are introduced. The development and validation of two SWCNT-based oxytocin imaging probes are then described. The first probe, a near-infrared oxytocin nanosensor (nIROx), is the first synthetic probe capable of imaging oxytocin in the brain without interference from its structural analogue, vasopressin. It is synthesized by covalently conjugating an oxytocin receptor peptide fragment (OXTp) to the SWCNT surface. To develop the second oxytocin imaging probe, we leveraged an evolution-based platform, SELEC, and identified a noncovalent nanosensor, nIROSE (near-infrared oxytocin nanosensor identified by SELEC). nIROSE nanosensors utilize an evolved ssDNA molecular recognition moiety noncovalently adsorbed to the surface of SWCNT. Preliminary imaging experiments in acute tissue slices suggest that nIROSE can reversibly image electrically stimulated oxytocin release in brains. nIROSE and nIROx are complementary tools with different limitations and advantages. Together, these imaging probes may enable real-time imaging of oxytocin signaling throughout the brain to fully characterize oxytocin's function in both neurological health and disease.

To my mom, Claudia, the most positive and loving person that I know.

To my dad, George, who never fails to understand and support me.

Contents

Acknowledgements

No one achieves anything alone. I have so many people to thank for supporting me, making me laugh when I needed it, being kind and patient, and helping me during these last four years.

First and foremost, I need to thank my PI and mentor, Professor Markita P. Landry. Thank you for your compassionate mentorship. You are the best PI I could have asked for, and I appreciate all the guidance and grace you've given me. I'd also like to thank my co-advisor and Department Chair Professor Matt Francis. Matt, thank you for teaching me what it means to lead with kindness and for *always* rooting for grad students. I will miss spilling the tea with you. Joel Adlen, you are every graduate student's favorite resource and advocate. Thank you for being patient with me, lending a supportive ear, and helping me whenever I needed it. Ellen Levitan, thank you for answering my numerous silly questions. I'll miss your emails. Thank you both, Joel and Ellen, for keeping the lights on.

Before I came to Berkeley, there were many educators and mentors who helped me get here. Thank you, Mr. Kunzel, for instilling my love of math and thank you, Ms. Thomas, for making chemistry fun and engaging. Your classrooms were a haven. It is because of teachers like you that I decided to pursue a career in science. At Boston College, there isn't a person I can thank more than my mentor, professor, and PI, Dr. Annunziato. I fell in love with research because of you. I miss our morning chats about music and film. Thank you for your mentorship and guidance for the last 7 years. I look forward to boogie boarding with you and Virginia for years to come. I also want to thank Trent, my manager at Apple. Thanks for taking a chance on me. Thanks to my entire team, Ed, Laila, Ben, Zach, and Alison, for making work a daily pleasure. You were the best coworkers I could have asked for, and I hope you still find my post-it notes around the office.

I also need to thank my friends, family, and lab mates, without whom I would be lost. Mom and Dad, I dedicate my thesis to you. These last four years have not been easy for us, but like always, we tackled them with grit and an unparalleled sensor of humor. I love you both. Thank you to my dearest friend, Sophie, the strongest person that I know. You are my compass and my source of optimism. I'll see you in Madrid, sister. Thank you to the entire Swain family – you are my second home. Thank you to all the friends I have made at Berkeley. Thank you to my best friend, therapist, future podcast co-host, and consigliere, Kayli. I would not have survived grad school without you. I can't wait to see what we get up to next. Thank you to the girls, Jamie, Kerry, Susanna, Marisol, and Michelle. I'll cherish the dinners, laughs, tears, and bottles of wine we shared together. Thank you to my 2018 cohort - I'll always remember our trips to Tahoe. Thank you to the Landry Lab who welcomed me with open arms. It took me 4 rotations and 1 calendar year to find you, and I'm so grateful I did. Thank you for making our lab the best place on campus. Thank you to my undergraduate researchers and mentees, Esther, Xiaoqi, Alexia, and Sebastiana. You are all so brilliant. I know you have remarkable things in store. Thank you to my lab mentors, Nat, Travis, Becca, and Linda. I hope I'm at least half the scientist and mentor you are. Thank you to the kiddos, Francis, Madeline, and Josh. Together we make a perfect motley crew. We've always been friends first, co-workers second, and I'll miss you all every day. Thank you to my co-authors, Nick, Jaewan, and Jaquesta for your guidance, hard work, and patience. And thank you to the staff at Saul's Restaurant and Half Priced Books, my favorite places in Berkeley.

Lastly, I want to thank Dr. Michael Joseph Bellino and his staff. Thank you for giving me my life back.

List of Figures

List of Tables

Chapter 1

Introduction

1.1 Single-Walled Carbon Nanotubes (SWCNT)

1.1.1 What are SWCNT?

Since Iijima and Ichihashi reported the discovery of single-walled carbon nanotubes (SWCNTs) in 1993[1, 2], these carbon materials have garnered interest in applications ranging from hydrogen storage to drug delivery and chemical sensing. Microscopically, SWCNT appear as cylindrical sheets of graphene consisting of a hexagonal, *sp*^{2}-hybridized carbon matrix. SWCNT have a high aspect ratio, with single nanometer diameters and lengths up to several micrometers, making them essentially one-dimensional materials (Figure 1.1). Every species of SWCNT can be identified by their diameter and their chirality. SWCNT chirality is defined by two integers (*n* and *m*), which correspond to the vectoral direction in which the graphene sheet is rolled relative to the point of origin within the lattice (Figure 1.2). The chirality and diameter of SWCNT also determine their electronic band structure and thus their classification as either metallic or semiconducting[3].

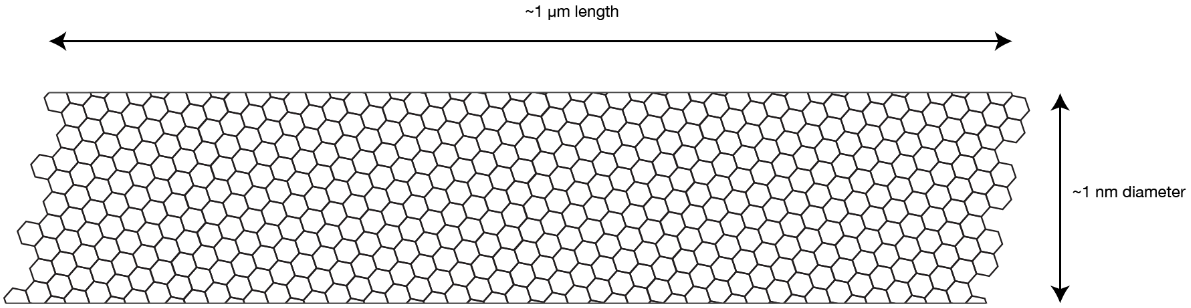

Figure 1.1 | Schematic depiction of single-walled carbon nanotubes (SWCNT). SWCNT consist of an *sp*^{2}-hybridized hexagonal carbon lattice and are essentially one-dimensional due to their high aspect ratio.

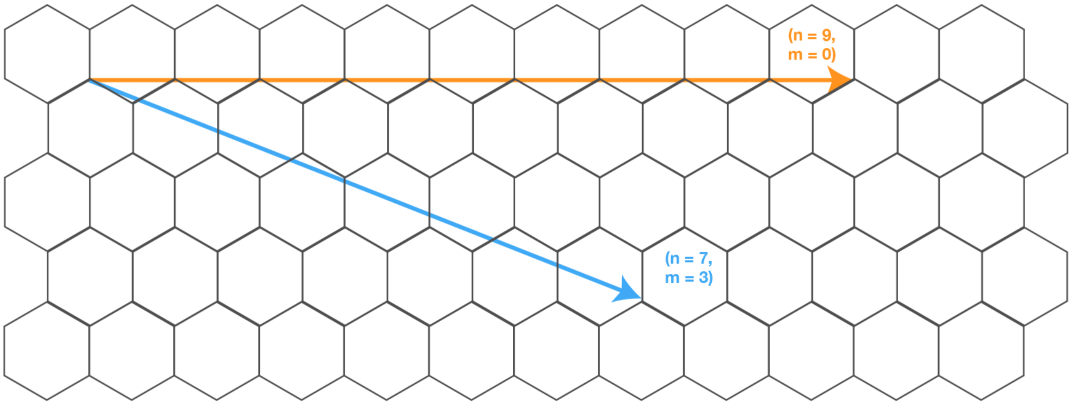

Figure 1.2 | Schematic depiction of SWCNT nomenclature. SWCNT are named by the vectoral direction, indicated by the indices *n* and *m*, in which the graphene lattice is rolled to produce them.

1.1.2 How are SWCNT made?

SWCNT are human-made materials that can be synthesized through various methods, including arc discharge, laser-abrasion, and catalytic chemical vapor deposition (CCVD)[4]. For all projects described in this dissertation, SWCNT were synthesized via high pressure CO disproportionation (HiPco). The HiPco process is a type of CCVD that produces high purity nanotubes, with minimal contamination from amorphous carbon[5, 6]. In this synthetic method, $Fe(CO)_5$ is used as a catalyst for SWCNT growth and injected into a stream of carbon monoxide gas at high pressure and high temperature. SWCNT grow on the metal catalyst, reaching a final length of ~500 nm and a diameter of ~1 nm. This process produces both metallic and semiconducting SWCNT of various chiralities. As different species of SWCNT have different electronic properties, and are thus useful for different applications, it is desirable to separate SWCNT by chirality and diameter. Methods such as aqueous two-phase (ATP) separation have been used successfully to isolate various SWCNT species, but often in low yield and with low efficiency[7]. Chirality-enriched SWCNT have also become commercially available but are often cost-prohibitive in academic research settings. Additional work is needed to develop inexpensive, efficient, and scalable methods to grow and sort individual SWCNT species[8]. This exciting and active area of research will undoubtedly expand the application and improve the performance of nanotube-based technologies.

1.1.3 Optical properties of semiconducting SWCNT

SWCNT have many outstanding thermal, mechanical, and electronic properties including high tensile strength, flexibility, high conductivity, and thermochemical stability. SWCNT are thus ideal materials for applications varying from reinforced conductors to field effect transistors to mechanical electronics, as illustrated in many comprehensive reviews of nanotube-based functional materials[9, 10]. For clarity and brevity, this dissertation will instead focus on the optical properties of semiconducting SWCNT and their bioimaging implications.

In 2002 the band-gap fluorescence of semiconducting SWCNT was discovered, enabling the development of SWCNT-based imaging platforms over the last 20 years[11, 12]. Semiconducting SWCNT fluoresce in near-infrared wavelengths, from 800-1600 nm, which fall in the tissue transparency window. As blood scatters and water absorbs primarily in visible and infrared wavelengths, respectively, SWCNT can fluorescence with minimal interference from tissue and are thus ideal for *in vivo* imaging applications (Figure 1.3). Unlike most fluorophores, organic and inorganic alike, which photobleach on the second-hour timescale, SWCNT neither blink nor photobleach even under hours of constant illumination[13, 14]. The stability of SWCNT emission suggests that SWCNT-based nanosensors can image indefinitely. Although raw, unfunctionalized SWCNT are insoluble and toxic to cells and tissue, noncovalent functionalization confers solubility and biocompatibility. Previous work has shown that functionalized-SWCNT do not affect cell viability[15], and intravenous administration of functionalized SWCNT do not affect acute or long-term health[16]. SWCNT do fluorescence with low quantum efficiency (η = $1.4x10^{-4}$) relative to other fluorophores[17], but their tissue-transparent fluorescence, photostability, and biocompatibility make them ideal materials for biological imaging probes.

Unlike most fluorophores, whose fluorescence can be understood by a single-electron depiction, SWCNT photophysics is exciton, not electron based. Excitons are photoexcited electron-hole pairs which are bound by Coulombic interactions[18]. Exciton effects dominate in semiconducting SWCNT because electron-hole attraction energies increase in one-dimensional materials. Due to their excitonic nature, the optical transition energy of SWCNT not only depends on their chirality, which defines their band gaps, but also the dielectric constant of the surrounding medium[13]. In other words, the surrounding environment can module SWCNT fluorescence, providing a mechanism for SWCNT-based optical sensing.

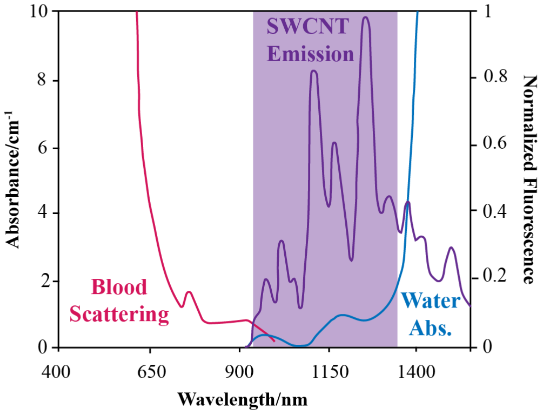

Figure 1.3 | Tissue-transparent fluorescence of SWCNT. SWCNT fluoresce in near-infrared wavelengths (800-1600 nm) which falls between the wavelengths at which blood scatters (visible) and water absorbs (infrared). Their tissue-transparent fluorescence makes SWCNT ideal for *in vivo* imaging applications. *Adapted from Boghossian et al.*[13]

1.1.4 SWCNT-based sensing

While SWCNT alone are insoluble, cytotoxic, and lack specificity for targets of interest, their surface can be functionalized to impart colloidal stability, biocompatibility, and molecular recognition. SWCNT-based sensors can thus be viewed as a two-component system containing a 1) molecular recognition element and 2) signal transducer.

Molecular recognition elements, such as peptides or ssDNA, can be either noncovalently adsorbed to the SWCNT surface, through probe-tip sonication[19] or ligand exchange[20], or covalently functionalized through triazine chemistry. In noncovalent adsorption, the hydrophobic and aromatic elements of functionalization polymers interact with the hydrophobic, elemental carbon surface of SWCNT, while their charged, hydrophilic, and polar elements interact with the aqueous environment to solubilize SWCNT constructs[21-23]. During covalent functionalization, molecular recognition elements are conjugated to SWCNT through a triazine handle. This synthetic strategy, developed by Setaro *et al.*, is currently the only strategy that enables covalent attachment to SWCNT without defects to the carbon lattice and thus maintains their inherent fluorescence[24, 25]. Covalent-SWCNT constructs often require further noncovalent functionalization to impart solubility.

Once SWCNT are functionalized with molecular recognition elements, they can selectively bind targets of interest. Furthermore, SWCNT can convert this binding event into a readable output because of their exciton-based photophysics. As described in Chapter 1.1.3, SWCNT fluorescence is sensitive to the surrounding dielectric environment. In the event of target binding, this dielectric sensitivity can be observed as an increase/decrease or solvatochromatic shift in SWCNT fluorescence[26]. In other words, SWCNT can transduce a target binding event through observable changes in their near-infrared fluorescence spectrum. Their unique photophysical properties thus provide a mechanism through which functionalized SWCNT can act as near-infrared fluorescent imaging probes.

1.2 Scope of dissertation

This dissertation contains three chapters, in addition to an introductory chapter and an appendix. In the introductory chapter, single-walled carbon nanotubes (SWCNT), their unique optical properties, and their application as signal transducers in nanosensors are introduced. The next chapter describes the current landscape of neuropeptide detection and motivates the development of SWCNT-based materials for neuropeptide imaging probes. The following two chapters focus on the development and testing of SWCNT-based probes for oxytocin imaging in the brain. In the appendix, a SWCNT-based nanosensor for SARS CoV-2 detection is presented.

Chapter 2 describes the current landscape of techniques for monitoring neuropeptides *in vivo*, from fast-scan cyclic voltammetry (FSCV) to microdialysis to G-protein coupled receptor (GPCR)-based probes. While these techniques have provided valuable insight into where neuropeptides act in the brain, they often lack the spatiotemporal resolution and/or selectivity to directly image or detect neuropeptide signaling events. The limitations of currently available assays motivate the development of synthetic probes for neuropeptide imaging, such as those described in Chapters 3 and 4.

Chapter 3 covers the development and validation of one SWCNT-based probe, called nIROx (near-infrared oxytocin nanosensor). nIROx are synthesized by covalent attachment of an oxytocin receptor peptide fragment to the SWCNT surface using a synthetic strategy that maintains the inherent fluorescence of SWCNT. These nanosensors are sensitive, reversible, and selective against oxytocin's structural analogue, vasopressin. nIROx nanosensors are the first real-time synthetic probe capable of imaging oxytocin release in the brain without vasopressin interference. Suggestions for improving nIROx performance in brains are also described.

Chapter 4 focuses on the use of an evolution-based platform, termed SELEC, for identifying ssDNA-SWCNT oxytocin nanosensors. For the first time, SELEC is used to evolve molecular recognition for a neuropeptide, demonstrating that SELEC can be adapted for larger, structurally complex neuro-targets. nIROSE (near-infrared oxytocin nanosensors identified by SELEC) are sensitive, reversible, and compatible with oxytocin receptor-targeted pharmacology. Preliminary results indicate that nIROSE can image oxytocin release in brain tissue, and, furthermore, suggest that nIROSE and nIROx are complementary oxytocin imaging tools with advantages for different applications. Next steps for nIROSE validation, both *in vitro* and *ex vivo*, are presented.

Appendix I introduces an ssDNA-SWCNT nanosensor for SARS CoV-2 detection. This nanosensor is synthesized through noncovalent adsorption of a Spike protein RBD-binding aptamer to SWCNT through a ligand-exchange strategy. These nanosensors respond optically to CoV-2 Spike RBD in a concentration-dependent manner. Although this project was unsuccessful due to reproducibility challenges, it provides a framework for synthesizing aptamer-SWCNT with ligand exchange and for developing SWCNT-based nanosensors with pre-existing molecular recognition elements.

Chapter 2

Techniques for monitoring neuropeptides *in vivo*

2.1 Abstract

Neuropeptides are a structurally and functionally distinct class of brain signaling molecules that pose unique challenges for detection *in vivo*. These molecules mediate a variety of critical processes, from social behavior to learning and stress response and are implicated in the pathogenesis of many neurological disorders and diseases including autism spectrum disorder and Alzheimer's disease. Without imaging probes with the selectivity, sensitivity, and spatiotemporal resolution requisite to capture endogenous signaling, our understanding of the central roles of neuropeptides remains incomplete. Well established techniques such as FSCV, microdialysis and radioimmunoassay have advanced our understanding of neuropeptides, and more recently developed GPCR-based probes have enabled *in vivo* imaging. Each of these detection platforms, however, have inherent limitations that motivate the development of synthetic probes for neuropeptide imaging. Recent advances in synthetic imaging probes and considerations for future development are also discussed herein.

2.2 Introduction

2.2.1 Distinct characteristics of neuropeptides

Since the discovery of Substance P by von Euler and Gaddum in 1931[27], over 100 mammalian neuropeptides have been identified and studied for their collective and individual characteristics[28, 29]. The ubiquity of neuropeptides in all animal groups possessing nervous systems, their ability to act as neurotransmitters, neuromodulators, and neurohormones, and the widespread central and peripheral distribution of neuropeptides and their receptors strongly implicate neuropeptides in regulating physiological processes[30-33].

Neuropeptides are a structurally distinct class of signaling molecules, ranging in size from a few to dozens of amino acid residues (Figure 2.1). Neuropeptides are thus smaller and less conformationally complex than most bio-active proteins but significantly larger than classical small molecule neurotransmitters. Their size and chemical complexity enable 10^3 higher affinities for their receptors (nanomolar K_d) compared to neurotransmitters (micromolar K_d)[32, 34]. Evidence has emerged over the last 40 years that neuropeptides are also functionally distinct from classical neurotransmitters. In the standard model of neurotransmission, chemical messengers are packaged into synaptic vesicles and released by axon terminals into the synaptic cleft where they act upon ionotropic receptors on postsynaptic dendrites; ionotropic receptors then rapidly hyperpolarize or depolarize the postsynaptic membrane. Alternatively, neuropeptides can be released nonsynaptically via volume transmission. Through this transmission scheme, neuropeptides are packaged into large dense-core vesicles (LDCVs) and released throughout the neuron, including dendritically, to bind their g-protein-coupled receptors (GPCRs) on target neurons.

Compared to ionotropic receptors, GPCRs mediate slow and tunable neurotransmission. By employing volume transmission, neuropeptides can function with lower spatial specificity (microns) compared to neurotransmitters (nanometers). While classic neurotransmitters, such as γ-aminobutyric acid (GABA) and glutamate, demonstrate millisecond half-lives due to specific uptake and degradation mechanisms, neuropeptides exhibit half-lives on the second to minute timescale[34]. For example, oxytocin and vasopressin neuropeptides can persist for ~20 minutes in cerebrospinal fluid (CSF)[35]. As a consequence of their extended lifetime and diffusion properties, neuropeptides can bind GCPRs with high affinity on distant neurons; furthermore, expression of a neuropeptide and its receptors may occur in mutually exclusive regions of the brain[36]. These characteristics hereby distinguish neuropeptides as their own class of signaling molecules with unique structural and functional properties.

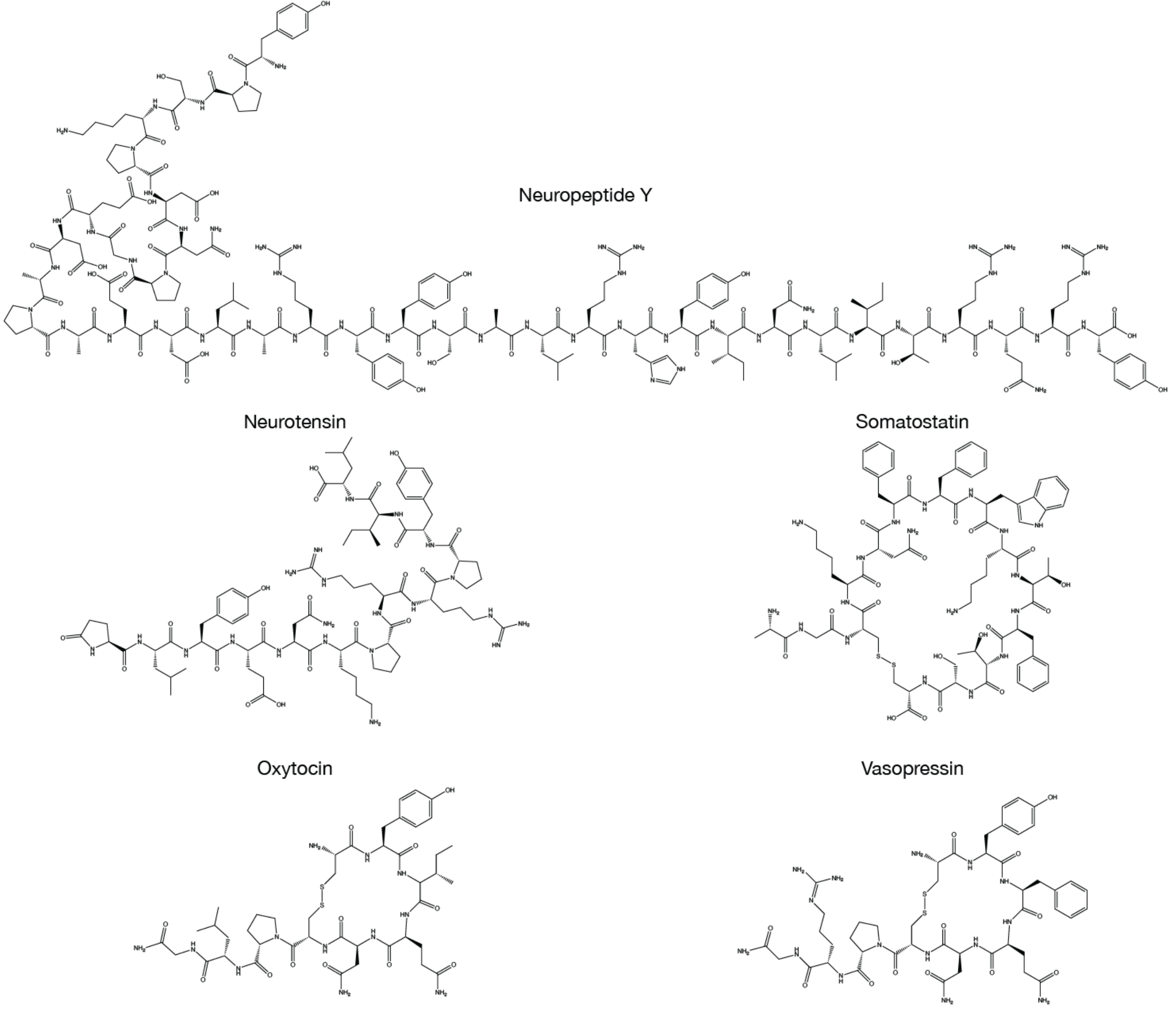

Neuropeptide Y

Neurotensin

Somatostatin

Oxytocin

Vasopressin

Figure 2.1 | Structures of neuropeptides. The chemical structures of neuropeptide Y, neurotensin, somatostatin, oxytocin and vasopressin are shown to illustrate the size and sequence diversity of neuropeptides.

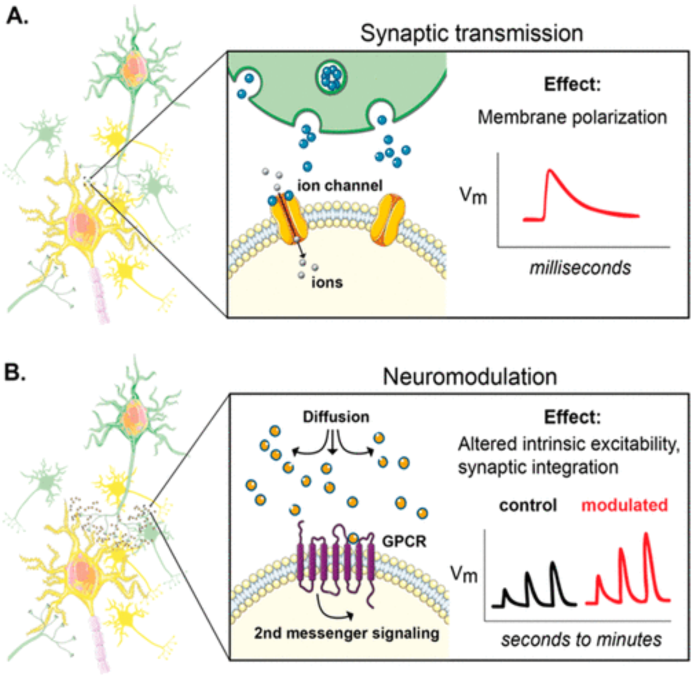

Figure 2.2 | Two major modes of chemical signaling in the brain. a, In fast synaptic transmission, neurotransmitter binds ligand-gated ion channels, allowing positively or negatively charged ions to flow into the cell. Ion flux rapidly changes the membrane potential (millisecond time scale). **b,** In neuromodulation, neuromodulators can escape the synaptic cleft and diffuse, allowing them to influence broader neural networks. GPCRs are the main targets of neuromodulators and do not pass current. GPCRs engage intracellular second-messenger pathways to modulate the function of pre- or postsynaptically expressed substrates through slower mechanisms (seconds to minutes). V_m is the membrane voltage. | *Reprinted from Beyene et al. to illustrate key difference between classical neurotransmitter and neuropeptide communication*[37].

2.2.2 Physiological and pathological roles of neuropeptides

Below, the currently understood functions of a subset of prominent neuropeptides are summarized to motivate the development of neuropeptide sensing technologies. While their central roles are not fully characterized, neuropeptides have been demonstrated to mediate social and sexual behavior, learning and memory processes, stress response, and energy homeostasis. Neuropeptides are also implicated in the pathogenesis of various neurological disorders and diseases such as anxiety, depression, autism spectrum disorder (ASD), posttraumatic stress disorder (PTSD), and Alzheimer's disease (AD).

Neuropeptide Y (NPY), the most centrally abundant neuropeptide, is widely distributed throughout the brain and is understood to play a role in the regulation of appetite, energy homeostasis, pituitary hormone release, and reproduction[38-40]. Single-nucleotide polymorphisms in NPY are associated with alcohol dependence in humans[38], and NPY and its many receptors may play a role in mood disorders, anxiety, and depression[41]. As deficits in NPY throughout the limbic brain have been shown to increase fear, anxiety, stress response, cognitive deficits in humans, NPY is strongly implicated in the pathophysiology of PTSD and may serve as a therapeutic for treatment of this disorder[42].

Somatostatin, another widely distributed neuropeptide in the CNS, plays a crucial role in modulating both cortical circuits and cognitive function. Multiple studies have reported a decrease in somatostatin expression in AD patients and AD mouse models[43], and changes in the expression of somatostatin and its receptors in cortical regions have been observed in Parkinson's disease. Attenuation of somatostatin concentration is further associated with Huntington's disease, major depressive disorder, and schizophrenia[44].

Oxytocin and vasopressin are small, structurally analogous neuropeptides that regulate many complementary behaviors and processes including learning, memory, pair bonding, social recognition, and anxiety[45, 46]. Oxytocin has been shown to regulate feeding behavior whereby exogenous administration can reduce food intake and body weight[39]. Numerous mutations in the V2 vasopressin receptor cause renal diabetes insipidus, while the vasopressin 1b receptor has been demonstrated as a viable target for the treatment of depression[32, 38]. Aberrations in oxytocin and vasopressin systems have been implicated in a variety social dysfunction disorders including ASD, social anxiety disorder, borderline personality disorder, and schizophrenia.[46] The therapeutic effect of oxytocin has been widely explored with many studies demonstrating the utility of exogenous oxytocin as a treatment for the core symptoms of ASD[47].

The neuropeptide neurotensin performs a variety of functions through the body, but primarily regulates dopaminergic and other neurotransmitter functions in the brain. Dysfunction of neurotensin systems is implicated in the pathogenesis of schizophrenia; central administration of neurotensin and an agonist for its NTR_1 receptor exhibit similar effects as antipsychotic drugs[41, 48].

While remarkable work has uncovered the vast and diverse functions of neuropeptides, much of our understanding is grounded in human and animal behavioral studies rather than direct study of neuropeptide signaling *in vivo*. Additionally, current links between neuropeptide function and neurological diseases are largely correlated, not causal, and have been largely evaluated by changes in neuropeptide concentration alone. Sensing technologies with the specificity and spatiotemporal resolution requisite to capture real-time neuropeptide signaling are requisite to fully characterize the modulations in neuropeptide function that underpin these conditions.

2.2.3 Challenges for neuropeptide sensing

Neuropeptides pose unique challenges for assay and sensor development. Although neuropeptide research has made important strides over the last few decades, the spatiotemporal dynamics and central functions of neuropeptides are not fully characterized. The traditional tools for probing small molecule neurotransmitter release are often incompatible with neuropeptides. For example, neurotransmitter release is traditionally studied indirectly by monitoring the immediate and local electrophysiological changes induced by synaptic transmission[49]. The release-response relationship of neuropeptides, however, is convoluted by both the mechanism of their release and actions of their target GPCRs. Endogenous neuropeptide transmission is slower and less spatially confined, making individual release events more challenging to quantify[30, 50]. Many neuropeptides are also co-transmitted with other signaling molecules in a state-dependent manner, enabling a single presynaptic neuron to have variable actions on different postsynaptic neurons[51, 52]. Some neuropeptides, such as peptide YY, demonstrate multiple functions or functions that are dependent on cell-type or neighboring receptors[53]. The same neuropeptide may also bind multiple GPCRs to induce different responses, as observed during neuropeptide Y transmission[30]. Direct methods are thus required to fully characterize the complicated actions and dynamics of neuropeptides.

Through quantitative assays of biological extracts, the concentrations of some neuropeptides have been determined. It is estimated that most neuropeptides are present in large dense-core vesicles at 3-10 mM[54]. Vasopressin and oxytocin are reported at 60 mM within these vesicles in the posterior pituitary[55], while in the CSF, these structural analogues are present at ~5 pM. The reported concentration of neuropeptides, however, vary significantly with both sample preparation and quantification technique[56, 57]. Interfering species in extracted samples and sensitivity limitations also impede the success of these assays[50].

While fast-scan cyclic voltammetry is traditionally used for rapid, real-time detection of signaling molecules, such as dopamine and serotonin, this technique is incompatible with many neuropeptides. Many neuropeptides either lack redox-active sites, a requisite for FSCV detection, or are present in sub nanomolar concentrations and are thus below the limit of detection for this method[58].

Direct detection of neuropeptides with optical probes offers an alternative to FSCV and *ex vivo* detection of biological extracts but faces additional challenges. Optical probes based on GPCR-neuropeptide recognition, for example, can lack specificity for their intended neuropeptide target. As many GPCRs bind with relatively high affinity to a variety of analogous neuropeptides, GPCR-based probes cannot differentiate between such analogues *in vivo*[59, 60]. GPCR-based probes may furthermore underestimate neuropeptide concentrations, as many neuropeptides exist naturally in distinct conformations and with different posttranslational modifications that demonstrate varying affinity for their endogenous receptor[61, 62]. These challenges motivate the development of probes with synthetic molecular recognition moieties that may circumvent the limitations of receptor-based probes.

2.3 Advances in neuropeptide analytical techniques

2.3.1 Radioimmunoassay

A radioimmunoassay (RIA) is an analytical tool that has been used to analyze the concentration of neuropeptides in animals and humans. This technique was first developed by Dr. Yalow, who was awarded the Nobel Prize for Physiology or Medicine in 1977 for this achievement[63]. In neuroscience, RIA has been used to study the functions and the distribution of neuropeptides. Despite significant improvements and usefulness of RIA, it still has some drawbacks that need to be further addressed. In this section, we discuss the working principles, applications, and advantages/limitations of RIA in characterizing neuropeptides.

RIA utilizes a specific interaction between antigens and antibodies. First, a certain quantity of an antigen is made radioactive with an isotope, such as iodine-125(^{125}I). Next, a known quantity of the antibody is mixed with the isotope-labeled antigen, which leads to the specific binding of the two. Then, a sample of interest containing an unknown quantity of the antigen is added to the above mixture. The radiolabeled antigen is displaced from the antibody by the unlabeled counterpart, due to competition between the two antigens. Finally, the mixture reaches an equilibrium state, where the relative binding of radiolabeled antigen is determined. Based on the radioactivity of the unbound antigen, the quantity of the antigen in the sample of interest can be calculated by generating a standard curve to quantify the relative binding as a function of known antigen quantities. All the same principles can be used with radiolabeled antibodies instead of antigens.

RIA has been one of the most widely used techniques to study neuropeptides in tissues and biological fluids, such as cerebrospinal fluid and plasma. For example, NPY, which plays an essential role in mammalian nervous systems, was examined via RIA[64-67]. While many applications of RIA to measure neuropeptides have been performed in plasma, blood, and tissue[66, 68, 69], a pioneering study by Allen et al. showed that NPY exists in various areas in the rat brain in abundance (hundreds of picomoles per gram of wet tissue)[67]. Specifically, forebrain regions contained the highest concentration of NPY, with NPY concentration gradually decreasing toward the brainstem.

Since the development of RIA, several strategies have been suggested to improve the technique. First, small molecular weight peptides (molecular weight < 4,000 Da) may have low immunogenicity, which could be resolved by coupling such peptides to a carrier protein[63]. Second, cross-reaction between molecules may occur, especially when they have similar structures. The cross-reaction may lead to low specificity of target antigen/antibody binding, which results in inaccurate concentration measurements. To avoid cross-reaction, pre-separation of the antigens may be performed via chromatographic methods[70, 71]. Lastly, separation between bound and unbound antigens requires careful optimization, as unsuccessful separation between the two may result in erroneous final concentration readings. Even with the above potential drawbacks, RIA is still an undoubtedly invaluable method in characterizing neuropeptides due to its high sensitivity.

Generally immunoassay techniques are valuable tools predominately used for quantifying neuropeptide concentrations in biological fluids such as plasma and saliva, yet it is still an active area of research as to whether these peripheral samples can serve as biomarkers for physiology and pathology relevant to central neuropeptide activity[72]. Regardless, immunoassay techniques as they currently stand disallow understanding of *in vivo* neuropeptide dynamics at timescales relevant to endogenous signaling in the brain and additionally have poor spatial resolution.

2.3.2 Microdialysis

Microdialysis is a method to quantify neurotransmitters, peptides, and hormones in the extracellular fluid. Microdialysis probes have semipermeable membranes, through which molecules of interest can flow as a function of the membrane size cutoff. Microdialysis membrane thresholds vary from ~20,000 Da, up to ~100,000 Da for large molecules such as neuropeptides[73]. Post-collection, several analytical techniques can be used to quantify the collected substances, such as RIA, enzyme immunoassays, or high-performance liquid chromatography.

Microdialysis has a few unique advantages over other techniques. First, microdialysis can be adapted to measure neuropeptides of freely moving animals *in vivo*[73-75]. In this respect, the semipermeable membrane's direct interaction with the extracellular fluid can be used to deliver drugs and other molecules through a process known as retrodialysis. Thus, the effects of such substances can be readily studied[58]. Second, unlike fast-scan cyclic voltammetry (FSCV), samples do not need to be electroactive, and any analysis techniques can be used after the collection based on which would be optimal for each particular analyte. Third, multiple samples can be collected simultaneously, enabling detailed analysis on the relationship between them[76].

Several studies have utilized microdialysis to investigate the change of neuropeptides. For instance, Neumann *et al.* studied the release of oxytocin and vasopressin in female rats before and after parturition and showed that oxytocin is released during both parturition and lactation, which may further promote oxytocin release[77]. Al-Hasani *et al.* examined the release of opioid peptides that are known to regulate motivated behaviors in behaving rodents *in vivo*[78]. The optogenetically-evoked neuropeptides were quantified with a custom microdialysis probe and nanoflow liquid chromatography-mass spectroscopy, which revealed the regional differences in the neuropeptide release between ventral and dorsal nucleus accumbens shell.

Despite its widespread use, some limitations make microdialysis less practical. In particular, the time resolution of microdialysis is difficult to improve beyond several minutes[58]. Therefore, subtle changes in extracellular fluid within seconds or minutes are difficult to quantify. Second, the measured concentration in dialysate is usually less than 40% of the true *in vivo* value[79]. This ratio is called extraction fraction or relative recovery. Therefore, the extraction fraction should be accurately measured with known concentration of analytes. Also, sensitive samples may degrade rapidly after microdialysis, which hinders their post-analysis[76]. Finally, microdialysis is an invasive technique requiring removal of the bone and tissue for a microdialysis probe to access the brain's extracellular fluid. Microdialysis has been noted for its unsuitability for human study[80], whereby thinner probes are generally preferred to reduce the tissue damage.

2.3.3 Fast-scan cyclic voltammetry

Fast-scan cyclic voltammetry (FSCV) is a technique that detects target analytes by inducing redox reactions at implanted electrodes. Carbon-fiber microelectrodes are mostly widely used, due to their small size, low resistor-capacitor (RC) time constant, and high biocompatibility[80]. A high voltage scan rate (>100 V s^{-1}) is used for FSCV, which allows for real-time measurements of neuropeptides with high temporal resolution[81]. Furthermore, each electroactive analyte shows different electrical responses depending on their unique redox potentials, so most redox-active samples can be distinguished via FSCV. FSCV also offers a low limit of detection; for example, a well-known neurotransmitter dopamine with nanomolar concentrations can be detected via FSCV[82], however, neuropeptides may be present at even lower concentrations[58]. Therefore, FSCV may require further improvements to achieve requisite sensitivity and signal-to-noise ratios to detect neuropeptides in the brain. To this end, several parameters such as FSCV waveform, electrochemical properties of microelectrodes, and data processing techniques, have been optimized to enable the detection of neuropeptides[80]. For example, Calhoun *et al.* performed real-time detection of an endogenous opioid peptide, Met-Enkephalin (M-ENK)[83], by implementing an optimized sawhorse waveform to enhance selectivity and sensitivity for M-ENK.

Several drawbacks still limit the use of FSCV in neuroscience. Predominately, FSCV can only characterize electroactive analytes, which restricts its versatility. Although amino acids such as tyrosine, tryptophan, methionine, and cysteine are indeed electroactive[81], widespread use of FSCV for neuropeptide sensing necessitates that the neuropeptide of interest contain redox active amino acids. Additionally, the neuropeptide cannot contain so many oxidizable amino acids such that the competing signals convolute the readout[82]. It is possible that neuropeptides, having larger and more complex structures, may have variable redox values that could make them more difficult to detect with FSCV in complex biological samples. Another limitation is that FSCV has relatively low spatial resolution because large probe implantation is required for the readings[58]. As FSCV captures readings averaged over multiple neurons surrounding the point at the tip of the probe, FSCV is currently unable to capture *in vivo* dynamics at single-cell or -synapse resolution[83]. While tissue damage expected from carbon-fiber microelectrodes is usually less than that from microdialysis probes[84, 85], implanted electrodes may damage surrounding brain tissue.

2.4 Advances in neuropeptide optical sensors

In recent years, interest in neurochemical imaging has grown with the introduction of a variety of techniques for neuropeptide sensing. These techniques have moved beyond the use of analytical instruments and towards the development of genetically encoded fluorescent sensors and synthetic chemical and nanomaterial-based probes. Optical approaches have the potential to interrogate central neuropeptide activity *in vivo* with greater specificity and higher spatiotemporal resolution than the previously discussed analytical techniques. Fluorescence-based approaches to image neurochemicals include cell-based neurotransmitter fluorescent engineered reporters (CNIFERs)[84] and neuropeptide release reporters (NPRRs)[50]. Fluorescence CNIFERS are useful tools for optical detection of volume transmission, a key facet of neuropeptide release, with high spatial resolution and the potential as a generalizable platform for any GPCR. Similarly, NPRRs are fused from a neuropeptide precursor to target dense core vesicles and a calcium sensor, GCaMP6s[86], to provide the fluorescent readout. The NPRRs are then taken up by dense core vesicles and released upon stimulation into the extracellular space, where their fluorescence can be measured and correlated with neuropeptide release. GPCR-based and NPRR-based probes are the two most common approaches for fluorescence-based detection and imaging of neuromodulators. Lastly, as discussed previously, GPCRs for neuropeptides can exhibit a high degree of intrinsic binding promiscuity to multiple targets[85, 86], and as such, generating selective probes based on GPCRs can be challenging. The development of synthetic chemical or nanomaterial-based probes to image neuropeptides is therefore an attractive alternative that could generate probes with high selectivity for a single target neuropeptide.

2.4.1 Genetically encoded fluorescent biosensors

Genetically encoded fluorescent biosensors are one potential approach to image neuropeptide dynamics. These methods exploit intrinsic cellular machinery to express protein-based probes in which fluorescent proteins generate a signal detectable by microscopy in response to a molecular event in particular neuronal populations. Genetically encoded probes can be targeted with cell-specificity to achieve highly specific and sensitive tracking of neurotransmission and neuromodulation. The basic design principles of a genetically encoded probe include (1) a sensing domain capable of binding the analyte of interest and (2) either one or two fluorophores, which will modulate their fluorescence in response to analyte-binding and conformational change.

In the case of a single fluorophore, the predominant strategy of biosensing involves rearrangement of the protein fluorophore into a circular permutant (cpFP). This rearrangement retains protein secondary structure, but temporarily disrupts the protein structure responsible for fluorescence, which is to be restored only upon analyte binding to the sensing domain. With two fluorophores, biosensors are based on the concept of Förster (or fluorescence) resonance energy transfer (FRET). The analyte-binding domain is sandwiched between two fluorophores, a donor and acceptor, and conformational change of this domain upon analyte interaction affects the distance and orientation between the donor and acceptor and thus their FRET efficiency, a distance-dependent measurement of how much excitation energy has been transferred from the donor fluorophore to the acceptor fluorophore. For both single- and multiple-fluorophore approaches, the molecular recognition element is usually provided by GPCR receptors or fragments thereof as the probe sensing domain. Several reviews further detail design approaches for generic genetically encoded biosensors including ways in which they may be used for neurochemical and neuropeptide imaging[58, 87-92].

Protein-based probes developed in recent years have accomplished molecular specificity and the ability to capture transient and prolonged signals with subsecond temporal resolution and in freely moving models such as mice and flies. However, with regards to neurochemicals, this work has primarily been accomplished for neurotransmitters, such as glutamate[93] and GABA[94, 95], and non-peptide neuromodulators, such as dopamine.

GRAB_{DA}[96] and dLight1[97], developed by Patriarchi *et al.* and Sun *et al.,* respectively, demonstrated an ability to detect dopamine *in vitro*, *ex vivo*, and *in vivo* in multiple model organisms with excellent performance. Both probes were developed by coupling a circular permutated EGFP (cpEGFP) to a human DA receptor and optimizing the chimera's performance to attain subsecond temporal resolution, cellular spatial resolution, and sub-micromolar affinity for dopamine with 10-fold and 70-fold selectivity over structurally similar catecholamine norepinephrine at physiologically relevant concentrations. Genetically encoded fluorescent probes have also been recently developed for neurotransmitters acetylcholine[98] and serotonin[99].

Despite these advantages of genetically encoded probes over traditional techniques such as microdialysis and FSCV, application of GPCR-based probes to neuropeptides remains a developing but promising area of research. Patriarchi *et al.* recently published on a genetically encoded orexin sensor, OxLight1[100]. For oxytocin, recent developments by Kwon *et al.* and Li *et al.,* respectively, have introduced OCTR-iTango2[101] and $\text{GRAB}_{\text{OT1.0}}$[102]. Furthermore, Li *et al.* have developed a suite of neuropeptide GRAB sensors[103].

Key considerations for genetically encoded sensors remain that the reliance on GPCR receptors as sensing elements can be problematic if probe activity affects endogenous G protein signaling pathways, or in cases where the endogenous GPCR has affinity for multiple neuropeptides.

2.4.2 Synthetic probes

Synthetic (non-protein-based) probes include both small molecule and chemical probes, and nanomaterial-based probes. Unlike genetically encoded probes, synthetic probes often do not rely on endogenous receptors for functionality. Depending on the probe design, the synthetic region can either serve as the recognition element for a particular analyte, can be coupled to a fluorophore for signal transduction, or the synthetic material itself can serve as the signal transducer necessitating a moiety which can detect the analyte of interest with appropriate selectivity.

When materials are scaled from macroscopic to microscopic, unique chemical, electrical, mechanical, and optical properties emerge, which may be leveraged towards biosensor development. For these reasons, nanomaterials are a highly useful platform with widespread biomedical potential for applications in drug delivery, therapeutics, and biosensing[104-106]. In addition to ease of synthesis and chemical tunability, their size scale can be similar to or smaller than above-mentioned fluorescent protein reporters, enabling their use in the brain microenvironment. Compared to classical fluorophores, nanoparticles tend to promote improved fluorescence properties including higher quantum yields, increased tissue transparency near-infrared emission wavelengths, and increased stability against photobleaching[107]. Nanoparticle-based fluorescent, plasmon-based, and electrochemical sensors have been developed using materials such as carbon nanotubes, graphene, quantum dots, metals, and silica[108-110], several of which have been developed for neurotransmitters[111-113]. As with protein-based probes, few of these nanoparticle-based techniques have demonstrated applicability for neuropeptide imaging and have been limited to classical small-molecule neurotransmitters or non-peptide neuromodulators, such as serotonin and dopamine.

Many synthetic probes developed to study neuropeptides to-date focus on identifying and quantifying neuropeptides in *ex vivo* biofluids as biomarkers[114, 115]. For instance, gold nanoparticles and zinc oxide nanotubes, respectively, have been used to detect dopamine in biological fluids such as serum and urine[116]. There also exist chemical and nanomaterial-based sensing techniques which enable measuring neuropeptide dynamics as well: Kim *et al.* prepared nanosensors from conjugated polymer dots and magnetic nanoparticles to sense neuropeptide cathepsin L *in vitro* and *in vivo* through a fluorescence quenching mechanism[117].

Carbon nanotubes (CNT), particularly the intrinsically fluorescent varietal single-walled carbon nanotubes (SWCNT), are increasingly being used as signal transducers in optical probes[118]. SWCNT fluoresce in the near-infrared spectrum, roughly between 1000 - 1300 nm, which is maximally transparent to biological tissues. Due to tissue autofluorescence, photon absorption, and photon scattering in visible wavelengths, near-infrared emitters are often preferred for the construction of biological probes. Optical probes based on SWCNT derive their molecular selectivity towards an analyte based on a synthetic corona phase which can be engineered via surface-adsorbed polymers to recognize particular analytes based on modification of SWCNT brightness of fluorescence band gap. Furthermore, this SWCNT-based sensing can be optimized for selectivity, sensitivity, and dynamic range, and further exhibit reversibility and non-photobleaching signals unlike most conventional fluorophores and fluorescent proteins whose signals degrade over time. The recent decade has introduced a variety of SWCNT-based sensors for biomolecule analytes, including neurotransmitters such as dopamine and serotonin[19, 119, 120].

Another signal transducer of interest for biosensing is the quantum dot (QD). QD optical properties, such as bright and stable fluorescence, grant them certain advantages over common organic dyes and genetically engineered fluorescent proteins. Recently, QDs have been synthesized to self-illuminate by coupling the QD to a mutant of bioluminescent protein, *Renilla reniformis* luciferase[121]. Conjugate QD655-Luc8 further demonstrated the ability to detect bioluminescence resonance energy transfer (BRET) emission in mice model deep tissue[122]. However, QDs, like SWCNT and most other synthetics materials, may not be intrinsically biocompatible. For instance, QDs necessitate surface modification with proteins, peptides, or polymers to bestow biocompatibility, stability against fouling, and functionality necessary for the potential applications in *in vivo* imaging.

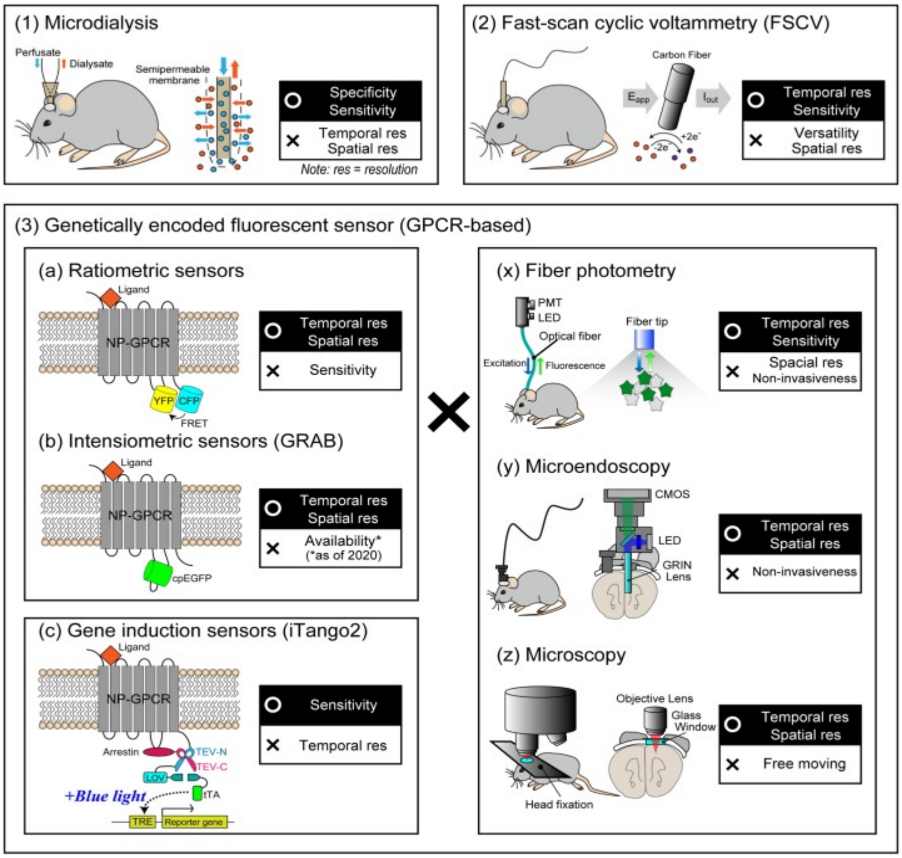

Figure 2.3 | Current and upcoming methods for detection of neuropeptides *in vivo*. The design principle is illustrated on the left of each box, and the advantages and disadvantages of each method are summarized on the right. The upper black boxes show advantages, and the lower white boxes show disadvantages. Microdialysis (1), fast-scan cyclic voltammetry (2), and genetically encoded fluorescent sensors (3) are shown. In the box of (3), subtypes of fluorescent sensors and subtypes of observation methods are classified. Ratiometric sensors (a), intensiometric sensors (b), gene induction sensors (c), fiber photometry (x), microendoscopy (y), microscopy (z). Further details are provided in the text. FSCV, fast-scan cyclic voltammetry; GPCR, G protein-coupled receptor; FRET, fluorescence resonance energy transfer. PMT, photomultiplier tube.| *Reprinted from Inutsuka et al. to illustrate the main contemporary techniques of neuropeptide detection*[58].

2.5 Direction of future neuropeptide probes

Analytical and optical tools for *in vivo* neurotransmitter and neuromodulator study have increased in recent decades, but neuropeptide-specific tools compatible with endogenous neuropeptide spatiotemporal signaling remain to be realized. Distinct from more classical neurochemicals in terms of size, structure, synthesis, release kinetics, and function, neuropeptide imaging will require significant modifications to these approaches toward accurately measuring their central and peripheral concentrations and signaling dynamics.

Herein several analytical and optical approaches typically used to study neurotransmitters and neuromodulators were described. Furthermore, recent translations of these technologies to study neuropeptides and/or considerations which must be made to refine these approaches to enable imaging of neuropeptide signaling in the brain were highlighted. Of particular interest are the areas of genetically encoded fluorescent sensors and synthetic probes, which have recently made progress in demystifying endogenous neurochemical signaling. These two approaches to generating optical probes have grown considerably in the past decade, taking vastly different approaches to sensor development and implementation with resulting complementary strengths and benefits.

Heretofore, protein-based probes have exhibited several advantages over synthetic probes. First, the level of specificity capable with genetically encoded probes is high and often difficult to achieve with purely synthetic probes, such as nanoparticles, as the level of analyte specificity evolved by biological receptors is challenging to replicate synthetically. Second, the ability to genetically encode and express protein-based probes enables cell specificity. Expressing these probes in specific cell types enables greater anatomical control during experimentation. Third, barring residual signaling from GPCR-based probes, protein-based probes are biocompatible when expressed in biological systems, enabling *in vivo* imaging of the target neurochemical.

Disadvantages of protein-based probes include relatively rapid photobleaching and challenges in red-shifting the emission of these probes to the tissue transparency window. Further, the reliance on their genetic expression can limit the study of non-model organisms, complex disease models, or young animals since expression of protein-based probes requires several weeks for expression. Genetically encoded probes can also interfere with endogenous GPCR signaling[98], may overexpress protein to deleterious extents and alter cellular physiology, and are often incompatible with pharmacology that interact with the native receptors from which the protein-based probes are derived. Depending on the evolved sensor, much work may be requisite to ensure protein expression remains orthogonal to biological processes. Genetically encoded probes are also often not spectrally distinct from probes for neuronal activity such as calcium dyes, posing the challenge toward simultaneous imaging of neuron activity and neurochemical signaling. Provided these factors are accounted for, genetically encoded fluorescent biosensors can be seamlessly integrated into existing biological toolsets and remain an incredibly important asset to the techniques available to neuroscientists probing neuropeptide signaling.

With characteristics complementary to protein-based probes, synthetic and nanomaterial-based probes exhibit several advantages. Specifically, biocompatible synthetic probes can be deployed seamlessly in non-model organisms and young animals with protocols similar to their demonstrated use in model organisms. Additionally, synthetic probes boast the tunable fluorescence of nanomaterials, often intrinsic in the deep tissue near infrared region. Synthetic sensors are advantageous in that there exist certain materials which can minimize issues such as tissue scattering and phototoxicity, problems relevant to optical based approaches depending on the relevant excitation and emission windows. While some synthetic probes are prone to the same issue, others such as SWCNT-based probes and quantum dot-based probes can emit in the NIR region mitigating those phenomena.

Despite their promise for sensor development, synthetic probes will be perceived by organisms as foreign materials and thus can provoke adverse effects such as toxicity and immunogenicity. The tunability of nanoparticle surfaces may facilitate improved biocompatibility; this area of study is therefore critical to synthetic probe development. It will also be important to address issues such as biofouling which can deteriorate sensor performance *in vivo*. Lastly, genetically encoded probes are expressed on cell membranes and thus confined to a particular locale of activity; however, synthetic nanoparticle-based probes are often deployed more broadly in the extracellular space of the brain.

Progress in both areas of optical probe development is key to expanding the toolkit of highly rapid and specific approaches to *in vivo* neuropeptide imaging. We have much yet to be understood regarding neuropeptide concentration, release, and dynamics, plenty of questions remain to be addressed, but it is also of great interest how the landscape of contemporary tools for neuropeptide detection *in vivo* will shift and the fundamental and translational discoveries which will be made.

Chapter 3

Near-infrared fluorescent nanosensor enables oxytocin imaging without vasopressin interference in brain tissue

This chapter is based on the following publication: Navarro, N.*; Jeong, S.*; Ouassil, N.; Mun, J.; Leem, E.; Landry, M. P., Near Infrared Nanosensors Enable Optical Imaging of Oxytocin with Selectivity over Vasopressin in Acute Mouse Brain Slices. *bioRxiv* **2022**, 2022.10.05.511026.[123]

3.1 Abstract

Oxytocin plays a critical role in regulating social behaviors, yet our understanding of its role in both neurological health and disease remains incomplete. Real-time imaging probes with the spatiotemporal resolution relevant to oxytocin endogenous signaling are required to fully elucidate oxytocin function in the brain. Towards this end, we developed a near-infrared oxytocin nanosensor (nIROx), a synthetic probe capable of imaging oxytocin in the brain without interference from its structural analogue, vasopressin. nIROx leverages the inherent tissue-transparent fluorescence of single-walled carbon nanotubes (SWCNT) and the molecular recognition capacity of an oxytocin receptor peptide fragment (OXTp) to selectively and reversibly image oxytocin. We employ these nanosensors to monitor electrically stimulated oxytocin release in brain tissue, revealing oxytocin release sites with a median size of 3 μm which putatively represents the spatial diffusion of oxytocin from its point of release. These data demonstrate that covalent SWCNT constructs such as nIROx are powerful optical tools that can be leveraged to measure neuropeptide release in brain tissue.

3.2 Introduction

Oxytocin is a nonapeptide[124] that plays essential roles in mammalian social and reproductive behavior[125]. Synthesized predominantly in the hypothalamus, oxytocin acts both peripherally as a peptide hormone and centrally as a neuropeptide to perform distinct but complementary functions[126]. When released throughout the brain, neuropeptide oxytocin regulates complex emotions and social behaviors[127], including recognition[128, 129], bonding[130], and anxiolysis[131, 132]. Oxytocin is also implicated in the pathogenesis of various social impairment disorders such as generalized social anxiety disorder (GSAD)[133, 134] and autism spectrum disorder (ASD)[135, 136] and has thus garnered interest as a potential therapy and therapeutic target.

While neuropeptide oxytocin has been studied extensively, we lack the tools to directly probe oxytocin signaling at the spatial (μM) and temporal (s) scales at which it is hypothesized to signal, precluding elucidation of its function in oxytocinergic communication. The gold standard for central oxytocin detection involves sampling with microdialysis followed by quantification with radioimmunoassay (RIA) or enzyme-linked immunosorbent assays (ELISA). The limitations of microdialysis include poor spatiotemporal resolution and significant variability in reported oxytocin concentration with different sample processing methods and quantification assays[56, 57, 137]. While fast-scan cyclic voltammetry (FSCV) can be used to directly measure neurotransmitter release with nanomolar sensitivity and high temporal resolution[138], FSCV-based detection of neuropeptides has heretofore proved challenging.

Einaga *et al.* developed a boron-doped diamond electrode for oxytocin detection[139], but the method remains limited to use in expert laboratories.

More recently, Kwon and colleagues developed a genetically-encoded oxytocin sensor, OXTR-iTango2, which enables EGFP expression in the presence of both oxytocin and blue light[101]. Utilizing the endogenous oxytocin receptor (OXTR)[140] as a sensing moiety, which binds both oxytocin and vasopressin, OXTR-iTango cannot distinguish between these two structurally analogous neuropeptides. This optogenetic platform enables labeling of oxytocin sensitive neurons for post-experimentation analysis of oxytocinergic cell activation but lacks the temporal resolution requisite for real-time oxytocin imaging. Selectivity, particularly against vasopressin, and slow temporal resolution limitations continue to pose a challenge for OXTR- and expression-dependent sensors, respectively[141].

The selectivity and spatiotemporal limitations of current techniques motivate this study, whereby we employ single-walled carbon nanotube (SWCNT)-based probes to image oxytocin in the brain. SWCNT are inherently fluorescent in near-infrared tissue-transparent wavelengths, biocompatible, photostable, and functionalizable with biopolymers to impart molecular recognition towards targets of interest[120, 142]. In prior work using SWCNT to image neuromodulators, Beyene *et al.* developed a catecholamine nanosensor non-covalently functionalized with short oligonucleotides to image dopamine release both in striatal brain tissue[19, 143] and at the level of single dopamine release sites in neuronal soma and dendrites[144].

Until recently, covalent modification of the SWCNT surface for nanosensor development remained intractable. Such covalent modifications normally introduce defects that quench SWCNT fluorescence, however, Setaro and colleagues developed a strategy to enable direct covalent functionalization of SWCNT while retaining the sp^2 carbon network and ergo their fluorescence[24, 25]. As described below, we leveraged this strategy and the recognition capacity of an oxytocin receptor peptide fragment (OXTp)[145] to develop real-time oxytocin imaging probes.

3.3 Results and discussion

3.3.1 Oxytocin nanosensor development and in vitro validation

Near-infrared oxytocin nanosensors (nIROx) were prepared from SWCNT as follows: (1) chemical re-aromatization of pristine SWCNT followed by conjugation with glycine to generate carboxylated triazine SWCNT (COOH-Trz-SWCNT), (2) covalent attachment of the oxytocin receptor peptide fragment (OXTp) via amide bond formation to make OXTp-modified SWCNT (OXTp-SWCNT), and (3) noncovalent adsorption of poly-cytosine (C_{12}) to produce nIROx (Figure 3.1). Defect-free fluorescent Trz-SWCNT were generated from pristine HiPCo SWCNT and subsequently reacted with glycine to form COOH-Trz-SWCNT by following previously reported protocols[24, 25, 146]. This synthetic strategy does not disrupt the sp^2 carbon network of SWCNT, thus retaining their near-infrared fluorescence. COOH-Trz-SWCNT were conjugated to the oxytocin peptide by amide bond formation between the N-terminal amine of the oxytocin peptide and the carboxyl group in COOH-Trz-SWCNT. The oxytocin peptide contains both a spacer region (GPGSG) at the N-terminus and a peptide sequence derived from the transmembrane VI domain of the human oxytocin receptor (MTFIIVLAFIVCWTPFFFV). Previous work demonstrates that the oxytocin peptide binds to oxytocin with high affinity[145]. Attachment of the oxytocin peptide to the SWCNT surface was verified through X-ray photoemission spectroscopy (XPS). The sulfur 2p/carbon 1s ratio increased from 0.05 to 0.12 after oxytocin peptide attachment to the carboxylated triazine ring due to the cysteine residue in the oxytocin peptide, while the peak area ratio of nitrogen 1s/carbon 1s was unchanged (Figure 3.6). To impart colloidal stability to OXTp-SWCNT, we leveraged a previously established protocol to noncovalently pin C_{12} DNA to the SWCNT surface. The C_{12} sequence was selected for its stable noncovalent adsorption to the SWCNT surface and low affinity for oxytocin (Figure 3.2d)[147].

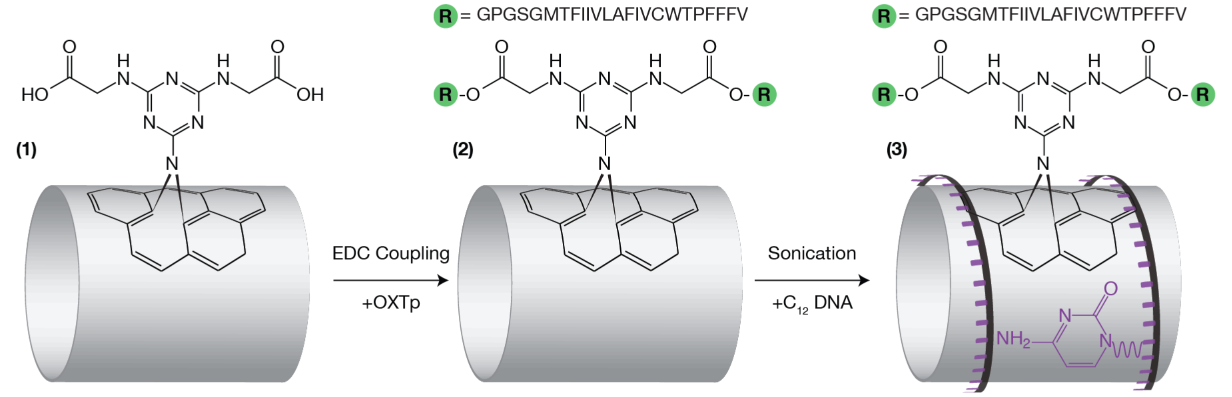

Figure 3.1 | Synthesis scheme of near-infrared oxytocin nanosensors (nIROx). The first product, COOH-Trz-SWCNT, was synthesized through covalent attachment of triazine to pristine SWCNT followed by glycine conjugation. The oxytocin receptor peptide (OXTp) was subsequently attached via EDC coupling. OXTp-SWCNT were noncovalently functionalized with C_{12} DNA to form colloidally stable nIROx.

The resulting nanosensor, nIROx, exhibits a chirality-dependent fluorescence response to oxytocin, where the maximum turn-on response is observed at the center wavelength of the (9,4) SWCNT chirality (~1126 nm) (Figure 3.2a). nIROx demonstrates a maximum peak fluorescence response ($\Delta F/F_o$) of 5.2 ± 0.10 (mean ± SD) to 2 mM oxytocin *in vitro* and responds to oxytocin in a concentration-dependent manner with a 235 nM limit of detection (LOD)[148] (Figure 3.2c, Chapter 3.6.1 Supporting Equations). We next calculated the nIROx kinetic parameters by fitting nIROx response versus oxytocin concentration to a cooperative binding model[149], resulting in an equilibrium dissociation constant (K_d) of 5.73 μM (Figure 3.2c, Chapter 3.6.1 Supporting Equations). As positive controls, we constructed SWCNT-peptide conjugates from two scrambled oxytocin peptide sequences, and one SWCNT without peptide altogether (Figure 3.2d). These negative controls, C_{12}-COOH-Trz-SWCNT, C_{12}-Scrambled OXTp 1-SWCNT, and C_{12}-Scrambled OXTp 2-SWCNT responded to 50 μM oxytocin with normalized $\Delta F/F_o = 0.11 \pm 0.02$, 0.030 ± 0.004, and 0.10 ± 0.02 (mean ± SD), respectively, relative to nIROx. The insensitivity of these constructs to oxytocin confirms that nIROx response to oxytocin occurs via molecular recognition between the oxytocin peptide sensing moiety and oxytocin, and that this molecular recognition is perturbed when the peptide is scrambled or outright omitted, as expected.

To characterize nIROx selectivity, nanosensor response was evaluated for a panel of neurochemicals including: glutamate, γ-aminobutyric acid (GABA), vasopressin, and thyrotropin-releasing hormone (TRH), where nIROx was found to be insensitive to these analytes (Figure 3.2b). As thyrotropin-releasing hormone is released in hypothalamus alongside oxytocin, nIROx selectivity to oxytocin over thyrotropin-releasing hormone [$\Delta F/F_o = 0.046 \pm 0.025$ (mean ± SD)] suggests that nIROx may be used as a selective oxytocin imaging probe in hypothalamic brain tissue [150, 151].

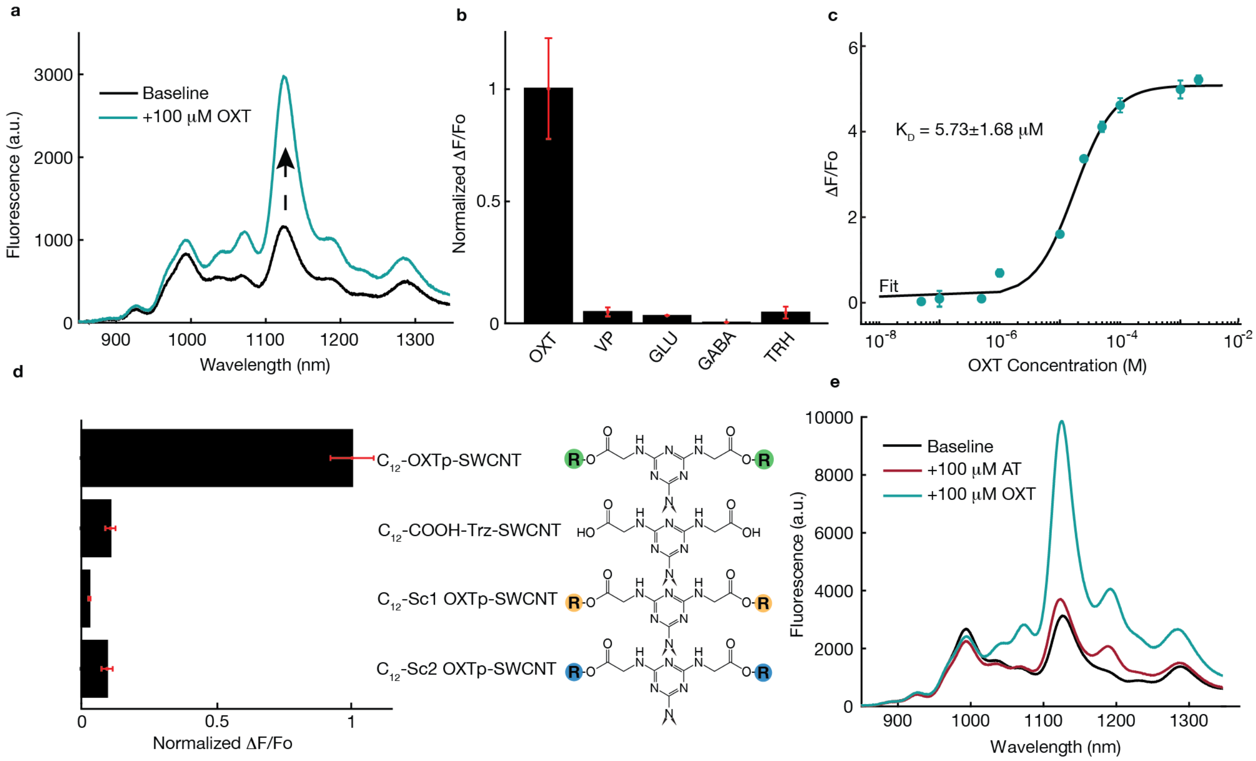

Figure 3.2 | nIROx *in vitro* validation. a, The full fluorescence spectrum of nIROx before (black) and after (blue) the addition of 100 µM oxytocin (OXT) in PBS. The maximum turn-on fluorescence response is observed at the center wavelength of the (9,4) SWCNT chirality (~1126 nm). **b,** nIROx selectivity screening at 50 µM oxytocin (OXT), vasopressin (VP), glutamate (GLU), γ-aminobutyric acid (GABA), and thyrotropin-releasing hormone (TRH). Black bars represent the mean $\Delta F/F_o$ at 1126 nm from n=3 replicates normalized to OXT response, with standard deviation of these replicates shown in red. **c,** Dose response curve of nIROx for OXT. Blue circles and error bars represent the mean of n=3 experimental measurements and the standard deviation of these measurements, respectively. $\Delta F/F_o$ is calculated from the normalized change in peak intensity at 1126 nm. The black line represents the cooperative binding model fit to experimental data. The K_d value is reported with 95% confidence intervals using the t-distribution. **d,** Response of various nanosensor constructs to 50 µM OXT, demonstrating that the oxytocin peptide sequence is requisite for OXT response and C_{12} DNA has low affinity for OXT. Black bars represent the mean $\Delta F/F_o$ at 1126 nm from n=3 replicates normalized to nIROx response, with standard deviation of these replicates shown in red. **e,** Full fluorescence spectra of nIROx before (black) and after the addition of 100 µM atosiban (red), followed by the addition of 100 µM OXT (blue). Atosiban reduces nIROx response to OXT by ~30% *in vitro* by competitively inhibiting oxytocin analyte binding.

nIROx also exhibits selectivity for oxytocin over carbetocin [$\Delta F/F_o$ = -0.059 ± 0.021 (mean ± SD)] (Figure 3.7a), a synthetic analogue with nanomolar binding affinity for the oxytocin receptor [152]. Most notably, nIROx respond minimally to vasopressin with $\Delta F/F_o$ = 0.050 ± 0.019 (mean ± SD) relative to oxytocin. Vasopressin binds the endogenous oxytocin receptor with high affinity[153] and differs from oxytocin by only 2 amino acid residues[154]. To date, our nanosensor is the first oxytocin imaging probe capable of distinguishing between these structurally analogous neuropeptides.

Prior to testing our probe in brain tissue, we evaluated nIROx reversibility by immobilizing nanosensors to the surface of a glass slide, enabling sequential oxytocin addition and removal from surface-adsorbed nIROx. We immobilized nIROx on a glass substrate using a previously described drop-casting method[149] and tracked the integrated fluorescence of nIROx during multiple oxytocin washes. Nanosensor response was immediate upon addition of 100 µM oxytocin (Figure 3.3). Washing the glass surface with phosphate buffered saline (PBS) to remove oxytocin resulted in an immediate decrease in integrated fluorescence, while subsequent additions of 100 µM oxytocin restored nIROx response. Each nanosensor, represented by grey traces in Figure 3.3a, maintained its fluorescence over continuous laser illumination over the course of the 300 second experiment without photobleaching. These data suggest that nIROx can reversibly bind and respond to oxytocin without signal attenuation.

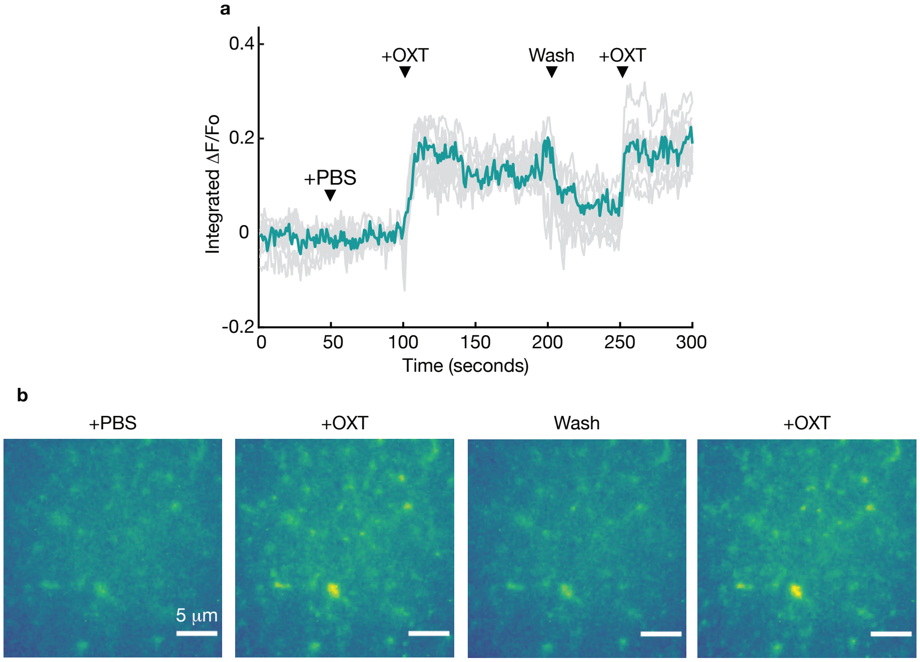

Figure 3.3 | Reversible oxytocin imaging on solid substrates. a, In vitro integrated $\Delta F/F_o$ traces from single ROIs (gray) and the mean $\Delta F/F_o$ trace (blue) from two washes of 100 µM OXT on glass-immobilized nIROx (n = 12). nIROx nanosensor retains its sensitivity to oxytocin after substrate immobilization and demonstrates a reversible turn-on fluorescence response upon repeated oxytocin washes. **b,** In vitro three intensity heat maps within the same field of view from two washes of 100 µM OXT on glass-immobilized nIROx. Four frames are represented: "+PBS" after addition of PBS, "+OXT" after addition of 100 µM OXT, "Wash" after washing the glass with PBS, and "+OXT" after the second addition of 100 µM OXT. Scale bars represent 10 µm.

3.3.2 Oxytocin imaging in acute brain slices

We next verified that nIROx can reversibly image oxytocin release in *ex vivo* brain tissue. Acute coronal mouse brain slices were prepared as previously described[155] and incubated with 2 mg/L nIROx in oxygen-saturated artificial cerebrospinal fluid (ACSF). Slices were then rinsed with ACSF to remove unlocalized nanosensor and transferred to an ACSF-perfused chamber for 15 minutes prior to imaging. This labeling protocol was previously demonstrated by Beyene *et al.* to enable even, widespread SWCNT labeling within brain tissue[19] and shown by Godin *et al.* to enable SWCNT localization in the extracellular space (ECS)[156] (Figure 3.9). To image nIROx, we used a custom-built visible (400-725 nm) and near-infrared (750-1700 nm) microscope capable of serial imaging on the same detector. A 785-nm laser was employed to excite nanosensor fluorescence, while a mercury bulb was used for bright-field imaging. Imaging channels were selected via sliding mirror, and both near-infrared and brightfield images were collected serially with a Ninox VIS-SWIR broadband camera (Raptor Photonics) with the corresponding dichroic filters and a 60x water-dipping objective (Nikon).

To confirm nIROx nanosensors are capable of responding to oxytocin in brain tissue, nIROx was first introduced in the dorsal striatum of acute brain slices and nanosensor response was characterized upon addition of 100 μM of exogenous oxytocin. After collecting ~30 seconds of baseline nIROx fluorescence in slice, oxytocin was manually injected into the 3 mL recording chamber containing ACSF. Exogenous oxytocin injection yielded an increase in nanosensor fluorescence [$\Delta F/F_o = 0.36 \pm 0.10$ (mean ± SD)] and thus validated nanosensor utility for imaging oxytocin in *ex vivo* brain slices (Figure 3.8a,b). Nanosensor response to exogenous oxytocin was not immediate and likely attributable to slow diffusion of the oxytocin injection through the recording chamber and into the acute slice bath. Washing of the chamber with ASCF gradually reduced nIROx fluorescence, demonstrating the reversibility of nanosensor binding to oxytocin in brain tissue and supported by our *in vitro* reversibility experiments.

nIROx were then introduced into the paraventricular nucleus (PVN) of mouse brain slices to evaluate their utility as endogenous oxytocin imaging probes. Oxytocin neurons are predominantly found in the supraoptic nucleus (SON), PVN, and accessory nuclei of the hypothalamus. Oxytocin is synthesized by magnocellular and parvocellular neurons, which differ in size, function, projection sites, and mode of oxytocin release[157]. The PVN was selected for oxytocin nanosensor imaging experiments owing to its distinct, identifiable structure and relatively high concentration of oxytocin, as reported previously in brain tissue by both microdialysis[158] and mRNA expression[159] studies. The imaging field of view of our custom microscope (178 μm by 142 μm) was capable of imaging multiple oxytocin release events within the PVN, where the somatic diameters of parvocellular and magnocellular neurons are roughly 15 μm and 25 μm, respectively[160]. To investigate nIROx imaging efficacy following electrically stimulated oxytocin release, we employed a bipolar stimulating electrode and applied a 0.5 mA, 1 millisecond single square pulse within the PVN for 2 biological replicates per experiment. Electrical stimulation evoked an instantaneous increase in nIROx fluorescence [$\Delta F/F_o = 0.41 \pm 0.038$ (means ± SD); $n = 3$] as shown in Figure 3.4a, Figure 3.10a, and Figure 3.13.

Upon demonstration that atosiban, a nonapeptide oxytocin analogue, decreases nanosensor response to oxytocin *in vitro* (Figure 3.2e and Figure 3.7b,c) we sought to recapitulate this effect in viable brain tissue as a positive control. Acute brain slices containing the PVN were labeled with nIROx and incubated in 1 μM atosiban for 15 minutes prior to repeating the above-mentioned stimulated oxytocin release imaging across 2 biological replicates. Incubation with atosiban, followed by electrical stimulation of acute tissue slices, yielded a lower nanosensor response relative to atosiban-free slices, with atosiban $\Delta F/F_o = 0.23 \pm 0.05$ (means ± SD) and a post-drug to pre-drug $\Delta F/F_o$ amplitude ratio of 0.56 ± 0.12 (means ± SD) across three stimulations (Figure 3.4b-d and 3.10). These data are consistent with *in vitro* experiments which revealed a $28 \pm 7.9\%$ decrease in peak $\Delta F/F_o$ upon incubation with atosiban compared to the atosiban-free control (Figure 3.7c). As atosiban attenuates nanosensor response similarly upon both exogenous oxytocin addition *in vitro* and electrical stimulation *ex vivo*, our results suggest nIROx response in brain tissue is largely attributable to endogenous oxytocin release. These data also provide insights into the mechanism by which atosiban reduces nIROx nanosensor response. Atosiban likely binds the oxytocin peptide sensing moiety of nIROx to competitively inhibit analyte binding and consequently reduces nanosensor response to oxytocin. While atosiban is known to antagonize the oxytocin receptor *in vivo*[161], the oxytocin receptor is minimally expressed within the PVN[162], and atosiban has not been reported to modulate oxytocin release within the hypothalamus. The effect of atosiban *ex vivo* is therefore likely due to competitive inhibition of nIROx rather than physiological changes in oxytocin release.

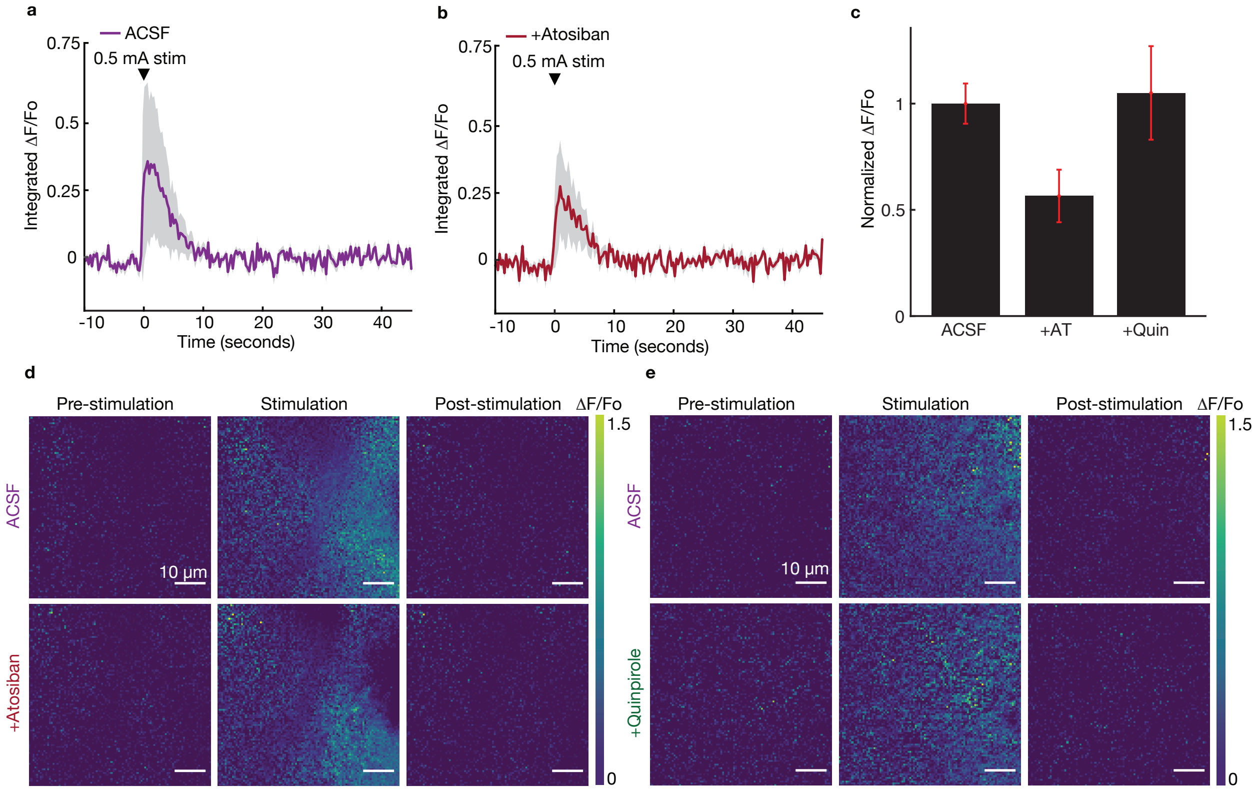

Figure 3.4 | Reversible oxytocin imaging in acute brain slices. a, *In brain slice* mean $\Delta F/F_o$ time trace (purple) and standard deviation (gray) following a single 0.5 mA electrical pulse stimulation in standard ACSF in the paraventricular nucleus (PVN). **b,** *In brain slice* mean $\Delta F/F_o$ time trace (red) and standard deviation (gray) following a single 0.5 mA electrical pulse stimulation in 1 μM atosiban in ACSF in the PVN. **c,** Integrated $\Delta F/F_o$ following 0.5 mA electrical pulse stimulations in ACSF, 1 μM atosiban (AT), and 1 μM quinpirole (Quin) normalized to $\Delta F/F_o$ in ACSF. Black bars represent the mean integrated $\Delta F/F_o$ across 3 stimulations with the standard deviations from these stimulations shown in red. **d,e** *In brain slice* $\Delta F/F_o$ of oxytocin nanosensor within the same field of view following 0.5 mA electrical stimulation in standard ACSF and either 1 μM atosiban (f) or 1 μM quinpirole (g) in the PVN. Three frames are represented for each: "pre-stimulation" is the baseline nanosensor fluorescence before electrical stimulation, "stimulation" is immediately following electrical stimulation, and "post-stimulation" is after nanosensor fluorescence has returned to baseline. The white scale bars represent 10 μm.

Concurrent monitoring of multiple neurotransmitters, neuromodulators, and neuropeptides, and their pharmacological agents often used in neurobiology research, is an important goal. To this end, coronal slices were also incubated in quinpirole, a D2 receptor agonist that inhibits presynaptic dopamine release[163, 164]. Quinpirole treatment was used to verify that off-target pharmacological agents have a minimal effect on nIROx response, motivating potential future use of nIROx concurrently with other neuromodulator probes. Upon demonstrating that quinpirole treatment does not modulate nIROx fluorescence *in vitro* (Figure 3.7a), slices were incubated in 1 μM quinpirole for 15 minutes prior to imaging. As expected, quinpirole had a negligible effect on nIROx $\Delta F/F_o$ across 2 biological replicates, yielding a post-drug to pre-drug $\Delta F/F_o$ amplitude ratio of 1.05 ± 0.220 (means ± SD) across three stimulations (Figure 3.4e, Figure 3.11, and Figure 3.12). These results indicate that nIROx do not interact with off-target but broadly utilized pharmacological agents such as quinpirole in brain tissue. Taken together, the results from atosiban and quinpirole treatment suggest that nIROx response in PVN-containing brain tissue slices is attributable to oxytocin release.

3.3.4 Oxytocin release site analysis

Using image stacks from nIROx-labeled and PVN-containing brain tissue slices subject to electrical stimulation, we employed custom MATLAB software to identify oxytocin release sites, termed regions of interest (ROIs), where post-stimulation $\Delta F/F_o$ is high. Overlay of ROIs with pre-stimulation images show that $\Delta F/F_o$ hotspots are not correlated to nanosensor labeling density of brain tissue (Figure 3.5a), as we had previously determined for nanosensors of this class. This observation suggests that $\Delta F/F_o$ hotspots correspond to greater oxytocin release rather than greater nanosensor localization and is consistent with the findings of Beyene *et al.* upon imaging catecholamine release with DNA-SWCNT nanosensors[19]. More recently, Bulumulla and colleagues utilized a SWCNT-based nanofilm to image dopamine release with synaptic resolution and demonstrated that ROIs represent individual neurochemical release sites with reported ROI size as a proxy for the spatial spread, or volume transmission element, of dopamine release[144]. We conducted similar analyses with nIROx brain slice imaging data and found that stimulations repeated in triplicate within the same field of view and across biological replicates yielded comparable putative oxytocin release site size distributions and a median ROI size of 3 μm (Figure 3.5b). Based on the findings of Bulumulla *et al.*, ROIs in our data likely correspond to single oxytocin release sites in the PVN while ROI size represents the spatial diffusion of oxytocin from these release sites. We quantified this putative oxytocin release site density by calculating the number of release sites per unit of PVN brain tissue area. This analysis revealed a median of 3 putative oxytocin release sites per 1000 μm^2 of brain tissue area.

While atosiban treatment did not significantly alter the ROI size distribution or median ROI size, as expected, atosiban did attenuate the number and release intensity of oxytocinergic ROIs. These results suggest that atosiban does not affect oxytocin diffusion from release sites for instances when oxytocin is successfully released, but rather interacts with nIROx to reduce nanosensor oxytocin sensitivity. Upon atosiban treatment, the post-drug field of view exhibits ~20% fewer ROIs relative to drug-free brain tissue stimulation. The total number of ROIs across all stimulations and biological replicates decreased from 366 to 297 following atosiban treatment, and the mean number of ROIs per stimulation decreased from 61± 25 to 49 ± 14 (means ± SD) with atosiban treatment (Figure 3.5c and Figure 3.14). These results suggest that atosiban "turns-off" a subpopulation of nIROx rendering these nanosensors non-responsive to oxytocin. We also compared $\Delta F/F_o$ values of ROIs before and after atosiban drug treatment. As the location and number of ROIs differs across stimulations, all 500

ROIs in the field of view were included in this analysis. This analysis revealed a post- to pre-drug ratio $\Delta F/F_0$ amplitude ratio of 0.75 ± 0.31 (means ± SD) across 3 stimulations (Figure 3.5d). These analyses provide further insight into the mechanism by which atosiban affects nanosensor response, suggesting that atosiban reduces nIROx response to oxytocin in 2 ways: by both reducing the number of responsive nIROx nanosensors and simultaneously reducing the sensitivity of responsive nIROx nanosensors to oxytocin. These data in slice are consistent with *in vitro* nIROx reduction in sensitivity and support our hypothesis that nanosensor response in slice is attributable to oxytocin release.

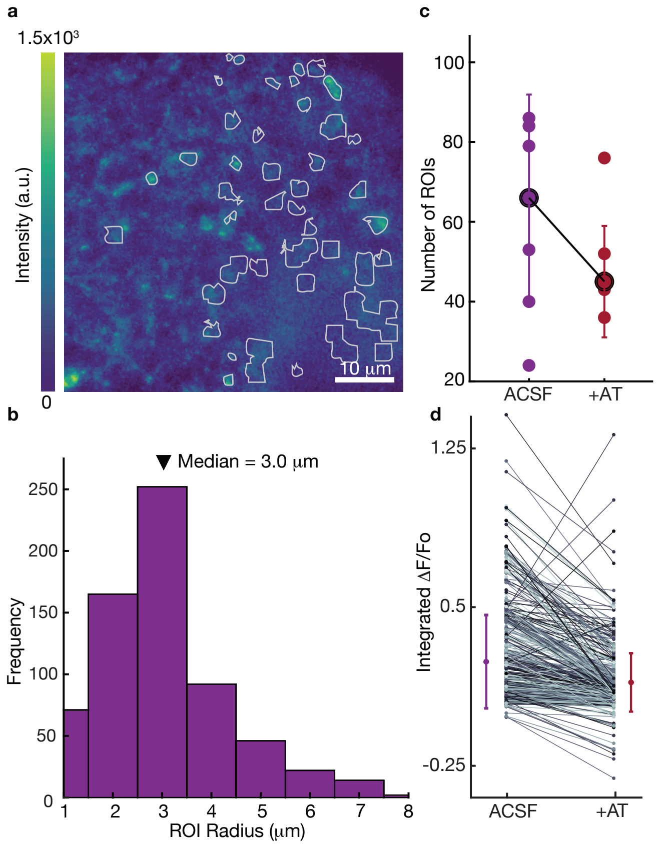

Figure 3.5 | Oxytocin release site analysis of nIROx-labeled acute brain slices. a, A single frame from an image stack acquired in the paraventricular nucleus (PVN). The field of view is overlaid with ROIs (gray) identified programmatically by calculating $\Delta F/F_0$ time traces of the image stack. Color bar represents nanosensor labeling fluorescence intensity. Scale bar represents 10 µm. **b,** Frequency histogram of ROI sizes across 4 biological replicates and 12 stimulations of the PVN in ACSF with median ROI size of 3 µm. **c,** Distribution of the number of ROIs across 6 stimulations in ACSF (purple) and 1 µM AT in ASCF (red). Mean (black) and error bars representing standard deviation of these stimulations. **d,** Integrated $\Delta F/F_0$ and standard deviation for all 500 ROIs across all biological replicates in ACSF and 1 µM AT in ACSF where $\Delta F/F_0$ values represent experimental means across 3 stimulations.

3.4 Conclusions

Imaging oxytocin in brain tissue with form factors compatible for use with existing neurobiological tools are needed to map the chemical activity of oxytocinergic neural circuits. In particular, neuropeptides such as oxytocin are posited to influence broad networks of neuronal activity through diffusion beyond the synapse during neurotransmitter release and are hypothesized to play key roles in social and maternal behaviors. Importantly, oxytocin signaling disruption is a likely contributor to autism spectrum disorders based on studies observing amelioration in social behavior upon administration of oxytocin to autistic patients. However, tools to image oxytocin at spatial and temporal scales of relevance to its endogenous signaling, and with requisite selectivity over its vasopressin analog, remain non-existent.

As described above, we developed and utilized nIROx, an oxytocin imaging probe for use in acute brain tissue slices containing oxytocinergic brain regions. nIROx was synthesized through covalent attachment of an oxytocin receptor peptide fragment (OXTp) to pristine SWCNT using a strategy that maintains SWCNT near-infrared fluorescence. Our successful nIROx synthesis demonstrates that SWCNT re-aromatization chemistries can covalently incorporate molecular recognition elements on the SWCNT surface, a concept that could be extended to other neuropeptide, neurohormone, and neurotransmitter targets. The resulting nanosensor, nIROx, responds fluorescently to oxytocin in near-infrared wavelengths with a peak $\Delta F/F_o$ >500% *in vitro*. We further show that nIROx synthesized with scrambled OXTp sequences or without a peptide do not respond to oxytocin, confirming that our nanosensor response occurs through molecular recognition of oxytocin via the oxytocin peptide moiety. Response screens against physiologically relevant neurochemicals, such as thyrotropin releasing hormone (TRH) and oxytocin's structural analogue, vasopressin, reveal nIROx selectivity for oxytocin. To date nIROx is the only oxytocin imaging probe developed that can distinguish between oxytocin and vasopressin for use in brain tissue.

Reversibility experiments both on solid substrates and in brain tissue revealed that nIROx responds reversibly to oxytocin and is capable of repeated imaging without signal attenuation and with no photobleaching. We also introduced our nIROx nanosensor into the PVN of acute brain slices and demonstrated that our nanosensor can image electrically stimulated release of oxytocin with an integrated $\Delta F/F_o$ of up to ~40%. From these imaging experiments, we identified ROIs, putative oxytocin release sites, measuring 3 μm in median diameter with a calculated density of 3 ROIs per 1000 μm^2 in PVN tissue. Based on previous studies with SWCNT-based neuroimaging probes, it is likely that these ROIs likely represent oxytocin release sites while their size is an approximate measurement of oxytocin's volume transmission upon release. To our knowledge, these data represent the first direct visualization of oxytocin in brain tissue with frame rate temporal and micron-scale spatial resolution. Lastly, we confirmed that nIROx nanosensor response *ex vivo* is insensitive to incubation with quinpirole, a D2 receptor agonist, but attenuated upon incubation with atosiban, a positive control that reduced nIROx response to oxytocin *in vitro*. We thus confirmed that nIROx response in brain tissue is attributable to oxytocin release and insensitive to off-target pharmacological agents. Importantly, the synthetic nature of nIROx and of all SWCNT-based probes potentiates their use in non-model organisms or young animals in which genetic manipulation is intractable or undesirable, which is of particular relevance for oxytocin given its presumed central role in early-age social development. Taken together, our results show that nIROx represents a near-infrared fluorescent, non-photobleaching nanosensor selective for oxytocin imaging in acute tissue slices containing oxytocinergic regions of the brain.

3.5 Materials and methods

3.5.1 Reagents

Small diameter HiPCo™ single-walled carbon nanotubes (SWCNT) were purchased from NanoIntegris (Batch #27-104). Oxytocin acetate salt hydrate, [Arg^8]-vasopressin acetate salt, dopamine-HCl, thyrotropin-releasing hormone (TRH), glutamate, γ-aminobutyric acid, and atosiban were purchased from Millipore Sigma. Quinpirole and carbetocin were purchased from Tocris Bioscience. Peptide sequences were purchased from Thermo Fisher Scientific, and DNA sequences were purchased with standard desalting purification from Integrated DNA Technologies, Inc.

3.5.2 nIROx synthesis

Nanosensors were fabricated by (1) the surface modification of SWCNT to form carboxylated SWCNT, (2) the conjugation of oxytocin binding peptide (OXTp) to carboxylated SWCNT to produce OXTp-conjugated SWCNT, and (3) DNA-wrapping of OXTp-conjugated SWCNT to form colloidally stable nIROx.

(1) *Carboxylated SWCNT fabrication:* Fabrication of fluorescent carboxylated SWCNT was adapted from previous literature[24, 25]. In brief, SWCNT (1 g) were dispersed in N-methyl-2-pyrrolidone (150 mL) in a round bottom flask and bath sonicated (Branson Ultrasonic 1800) for 1 h. The dispersion was stirred for 1 h at 25 °C and cooled to 0 °C. 2,4,6-1,3,5-trichloro-triazine (10 g, 54 mmol) was dissolved in N-methyl-2-pyrrolidone (50 mL) and slowly added to the SWCNT dispersion at 0°C. Sodium azide (1.76 g, 27 mmol) was added to the mixture and stirred for 2 h at 0°C followed by 12 h stirring at 70°C to yield triazine-functionalized SWCNT (Trz-SWCNT). The product was purified by centrifugation, washed with water and organic solvents (acetone, toluene, then chloroform), and lyophilized for storage and characterization. Trz-SWCNT (100 mg) were dispersed in dimethylformamide (DMF) (50 mL) and bath sonicated for 15 min at room temperature. Next glycine (10 mg) and a 1.5 molar excess of triethylamine were added to the mixture and stirred at 65 °C for 2 days. The product was purified by centrifugation and sequentially washed with DMF (2 × 4 mL) and water (2 × 4 mL). The carboxylated SWCNT product was lyophilized for characterization and stored at room temperature.

(2) *OXTp-conjugated SWCNT fabrication:* Carboxylated SWCNT (21.7 mg) were dispersed in DMF (0.5 mL) and bath sonicated for 15 min at room temperature. 1-Ethyl-3-(3-dimethylaminopropyl)carbodiimide (EDC) (1 µmol) and N-hydroxysuccinimide (NHS) (2 µmol) were added to the mixture and vortexed for 20 min. The mixture was centrifuged, the supernatant was discarded to remove excess EDC and NHS, and the precipitate was subsequently re-dispersed in DMF (4 mL). OXTp (GPGSGMTFIIVLAFIVCWTPFFFV) (100 nmol) and 1.5 molar excess of N,N-diisopropylethylamine (DIPEA) were added to the mixture solution and vortexed for 12 h at room temperature. For constructs prepared with scrambled OXTp sequences, either Scrambled OXTp 1 (GPGSGWLIFTVMCTIPAFVFFIFV) or Scrambled OXTp 2 (GPGSGITFILVMFFVWFVAICTPF) peptides were used instead of OXTp. The product was

purified by centrifugation and subsequent re-dispersion in washes of DMF (2 × 4 mL) followed by washes of water (2 × 4 mL). The OXTp-SWCNT product was lyophilized for characterization and stored at room temperature.

(3) *DNA-wrapping of OXTp-conjugated SWCNT for oxytocin nanosensor:* OXTp-conjugated SWCNT (0.1 mg) was added to PBS (0.99 mL) and mixed with poly-cytosine (C_{12}) (10 μL, 1 mM). The resulting mixture was first bath sonicated for 2 min and then probe-tip sonicated (Cole-Parmer Ultrasonic Processor, 3-mm tip in diameter) for 10 min at 5 W power in an ice bath. The suspension was centrifuged for 30 min at 16,100 g to precipitate non-dispersed SWCNT, and the supernatant containing colloidal C_{12}-wrapped OXTp-SWCNT (nIROx) was collected. The concentration of the nIROx suspension was calculated by measuring absorbance at 632 nm (NanoDrop One, Thermo Scientific) with an extinction coefficient of $\varepsilon = 0.036\ (\mathrm{mg/L})^{-1}\ \mathrm{cm}^{-1}$[142]. Nanosensors were stored for up to 8 days at 4°C.

3.5.3 Optical characterization and analyte screening

Near-infrared fluorescence spectra were collected using a custom built spectrometer and microscope as described previously[165]. Measurements were obtained with a 20X objective on an inverted Zeiss microscope (Axio Observer.D1) coupled to a spectrometer (SCT 320, Princeton Instruments) and liquid nitrogen cooled InGaAs linear array detector (PyLoN-IR, Princeton Instruments). Nanosensor suspensions were excited with a 721 nm laser (OptoEngine LLC) inside a polypropylene 384 well-plate (Greiner Bio-One microplate).

For analyte screening, the baseline near-infrared fluorescence spectrum of each nanosensor-containing well was collected. Either PBS or analyte diluted in PBS was added, and post-analyte fluorescence spectra were collected at 10-minute time points until the maximum oxytocin fluorescence response was achieved (~60 minutes). Responses were calculated and reported as $\Delta F/F_o = (F- F_o)/ F_o$, where F_o is the peak fluorescence after PBS incubation, and F is the peak fluorescence after analyte incubation. The peak fluorescence corresponds to the (9,4) SWCNT chirality, which has a maximum near-infrared fluorescence at ~1126 nm.

For selectivity screening, all analytes were added at a final concentration of 50 μM. During oxytocin screening of various nanosensor constructs, oxytocin was added at a final concentration of 50 μM. For dose response experiments, final oxytocin concentration ranged from 50 nM to 2 mM.

For drug screening, the baseline near-infrared fluorescence spectrum of nIROx was first collected. Atosiban was subsequently added and incubated for 10 minutes before collecting post-drug fluorescence spectra. Finally, oxytocin was added and incubated for 10 minutes before collecting post-neuropeptide fluorescence spectra. Responses were calculated and reported as $\Delta F/F_o = (F- F_o)/ F_o$, where F_o is the peak fluorescence after atosiban incubation, and F is the peak fluorescence after oxytocin incubation. Both atosiban and oxytocin were added at a final concentration of 100 μM.

For *in vitro* experiments, nIROx suspensions were prepared at 5 mg/L in PBS. All measurements were obtained in triplicate, and reported results include the means and standard deviations of these measurements. All nanosensor batches were validated for oxytocin response *in vitro* prior to brain tissue imaging.

For reversibility experiments on glass, nIROx were immobilized on MatTek glass-bottom microwell dishes (35 mm petri dish with 10 mm microwell). To immobilize nanosensors, the dish was washed twice with PBS (150 μL). Nanosensors (100 μL, 2.5 mg/L in PBS) were then added, incubated for 10 minutes, and removed. The dish was washed twice again with PBS (150 μL). Surface-immobilized nIROx were imaged on an epifluorescence microscope (100x oil immersion objective) and a Ninox VIS-SWIR 640 camera (Raptor) and excited with a 721 nm laser. For each imaging experiment, the z-plane was refocused and 120 μL PBS was added prior to recording. Image stacks were collected with a 950 ms exposure time and 1 Hz frame rate for 5 minutes. PBS was added at frame 50 and oxytocin was added a final concentration of 100 μM at frame 100. At frame 200, the dish was washed with PBS, and at frame 250, oxytocin was added again at a final concentration of 100 μM. Image stacks were processed in ImageJ by applying a median filter (0.5-pixel radius) and rolling ball background subtraction (300-pixel radius). ROIs were manually identified and characterized using the ROI analyzer tool. Responses were calculated and reported as $\Delta F/F_o = (F- F_o)/ F_o$, where F_o is the mean integrated fluorescence after PBS incubation, and F is the peak fluorescence at each timepoint after oxytocin addition. The means and standard deviation of all 12 ROI $\Delta F/F_o$ values are reported.

3.5.4 Acute slice preparation and nanosensor labeling

The mice used for acute slice imaging experiments were male, 14-17 weeks old, C57BL/6 strain, and purchased from Jackson Laboratory. After weaning at postnatal day 21 (P21), mice were group-housed with nesting material on a 12:12 light cycle. All animal procedures were approved by the UC Berkeley Animal Care and Use Committee (ACUC). Acute brain slices were prepared using established protocols[155]. Mice were first anesthetized with an intraperitoneal injection of ketamine and xylazine, followed by transcardial perfusion with cutting buffer (119 mM NaCl, 26.2 mM $NaHCO_3$, 2.5 mM KCl, 1mM NaH_2PO_4, 3.5 mM $MgCl_2$, 10 mM glucose). The brain was subsequently extracted, and its connective tissues were trimmed. The brain was mounted on a vibratome cutting stage (Leica VT 1000) to prepare 300 μm thick coronal slices containing the putative paraventricular nucleus. Slices were incubated at 37°C for 30 minutes in oxygen saturated ACSF (119 mM NaCl, 26.2 mM $NaHCO_3$, 2.5 mM KCl, 1mM NaH_2PO4, 1.3 mM $MgCl_2$, 10 mM glucose, 2 mM $CaCl_2$) and then transferred to room temperature for 30 minutes. Slices were maintained at room temperature for all acute slice imaging experiments.

For nanosensor labeling, slices were transferred into a brain slice incubation chamber (Scientific Systems Design, Inc., AutoMate Scientific) containing 5 mL of oxygen-saturated ACSF. Slices were incubated with nanosensor at a final concentration of 2 mg/L SWCNT for 15 minutes. To remove unlocalized nanosensor from brain tissue, slices were rinsed for 5 seconds with oxygen-saturated ACSF through 3 wells of a 24-well plate. Rinsed slices were transferred to the recording chamber and perfused with ACSF for 15 minutes before imaging. All acute slice imaging experiments were performed at 32°C.

3.5.5 Microscope construction and acute slice imaging

Ex vivo slice imaging experiments were conducted using an upright epifluorescent microscope (Olympus, Sutter Instruments) mounted onto a motorized stage. A 785-nm continuous-wave diode-pumped solid-state laser with a maximum power of 300 mW and a near TEM00 top hat beam profile (Opto Engine LLC) was used for nanosensor excitation. The beam was expanded to a diameter of ~1 cm using a Keplerian beam expander composed of two plano-convex lenses (*f* = 25 and 75 mm; AR coating B, Thorlabs). The beam was passed through a fluorescence filter cube [excitation: 800 nm shortpass (FESH0800), dichroic: 900 longpass (DMLP990R), and emission: 900 longpass (FELH0900); Thorlabs] to a 60× Apo objective (numerical aperture, 1.0; working distance, 2.8 mm; water dipping; high nIR transmission; Nikon CFI Apo 60XW nIR). Emission photons collected from the sample were passed through the filter cube, focused onto a two-dimensional InGaAs array detector [500 to 600 nm: 40% quantum efficiency (QE); 1000 to 1500 nm: >85% QE; Ninox 640, Raptor Photonics], and recorded with Micro-Manager Open Source Microscopy Software[166].

3.5.6 Exogenous oxytocin and electrical stimulation evoke oxytocin imaging with nIR microscopy

During exogenous oxytocin imaging, a total of 600 frames were acquired at nominally 4 frames per second in the dorsal striatum. After collecting 100 frames of baseline, 100 μM oxytocin was injected into the 3 mL recording chamber. Oxytocin was then removed with ACSF perfusion at frame 400.

To electrically stimulate oxytocin release, a bipolar stimulation electrode (MicroProbes for Life Science Stereotrodes Platinum/Iridium Standard Tip) was positioned within the putative paraventricular nucleus using a 4x objective (Olympus XLFluor 4x/340). The stimulation electrode was introduced into the top of the brain slice and an imaging field of view nominally 50 μm from the stimulation electrode was chosen using a 60x objective. A total of 600 frames were acquired at nominally 4 frames per second, where stimulations were applied after 200 frames of baseline. Each stimulation was repeated three times within a field of view. Stimulation pulses were applied for 1 millisecond at 0.5 mA. During drug screening, imaging experiments were first conducted in drug-free ACSF. Then using the same field of view, either quinpirole or atosiban was added to the imaging chamber through ACSF perfusion. The slice was incubated in 1 μM of either drug for 15 minutes before imaging. Drug screening imaging experiments were acquired in biological duplicate.

3.5.7 Image processing and data analysis of nanosensor fluorescence response

Imaging movie files were processed using a custom MATLAB application (https://github.com/jtdbod/Nanosensor-Brain-Imaging). ROIs were identified by first applying a 25x25 pixel grid mask to the image stack. The median pixel intensity and a median filter convolution within each ROI was then calculated. Post-stimulation and exogenous oxytocin fluorescence responses were calculated as $\Delta F/F_o = (F - F_o)/F_o$, where F_o is the average intensity for the first 5% of frames and F is the dynamic fluorescence intensity. Significant $\Delta F/F_o$ traces were identified by thresholding with Otsu's methods to differentiate ROIs from the background. For stimulation experiments, decay time constants (τ) were computed for significant ROIs by fitting each $\Delta F/F_o$ trace to a first-order decay process. Latency to peak was calculated as $t_{peak} - t_{stim}$, where t_{peak} is the time at which maximum fluorescence occurs, and t_{stim} is time of stimulation. The $\Delta F/F_o$ traces where latency to peak is greater than 5 seconds were assumed to result from stimulation artifacts and were thus removed from analysis. The maximum $\Delta F/F_o$ of each significant ROI trace was identified, and the $\Delta F/F_o$ of a stimulation or exogenous oxytocin wash was reported as the median of these values. For stimulation experiments, ROI size was determined by first identifying F_{max} within a significant ROI. All pixels with an intensity value >50% of F_{max} were included within the boundaries of an ROI. ROIs with a radius <1 μm were removed.

3.6 Supporting information

3.6.1 Supporting equations

The LOD of nIROx for oxytocin is calculated as the lowest oxytocin concentration that is statistically different from the blank using the equation below:

$$\text{LOD} = (\text{mean } \Delta F/F_o)_{\text{blank}} + 3(\text{STD } \Delta F/F_o)_{\text{blank}}$$

For the concentrations of oxytocin tested, the LOD is calculated as $\Delta F/F_o = 0.161$ This $\Delta F/F_o$ value corresponds to 235 nM oxytocin based on the cooperative binding model fit.

nIROx nanosensor kinetic parameters were quantified by fitting dose response data to the cooperative binding model below:

$$\frac{F-F_o}{F_o}=a\,\frac{(K_d[S])^n}{(K_d[S])^n+1}+b$$

Kinetic parameters were calculated as $n=1.33\pm0.51$, $b=0.14\pm0.29$, $a=4.94\pm0.5$, and $K_d=5.73\pm1.68$ μM and are reported with 95% confidence intervals using the t-distribution.

3.6.2 Supporting figures

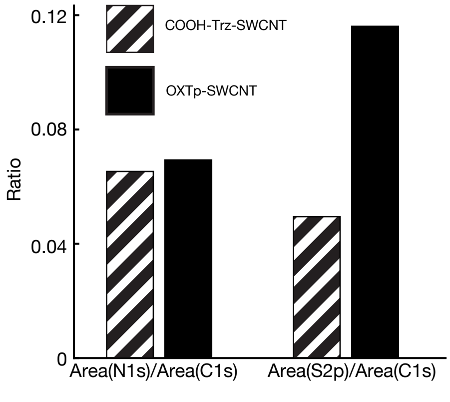

Figure 3.6 | nIROx nanosensor synthesis validation. Verification of oxytocin peptide (OXTp) attachment through x-ray photoelectron spectroscopy (XPS). The sulfur 2p/carbon 1s ratio increases from 0.05 to 0.12 after OXTp conjugation due to the cysteine residue in the oxytocin peptide sequence. The nitrogen 1s/carbon 1s ratio remains unchanged.

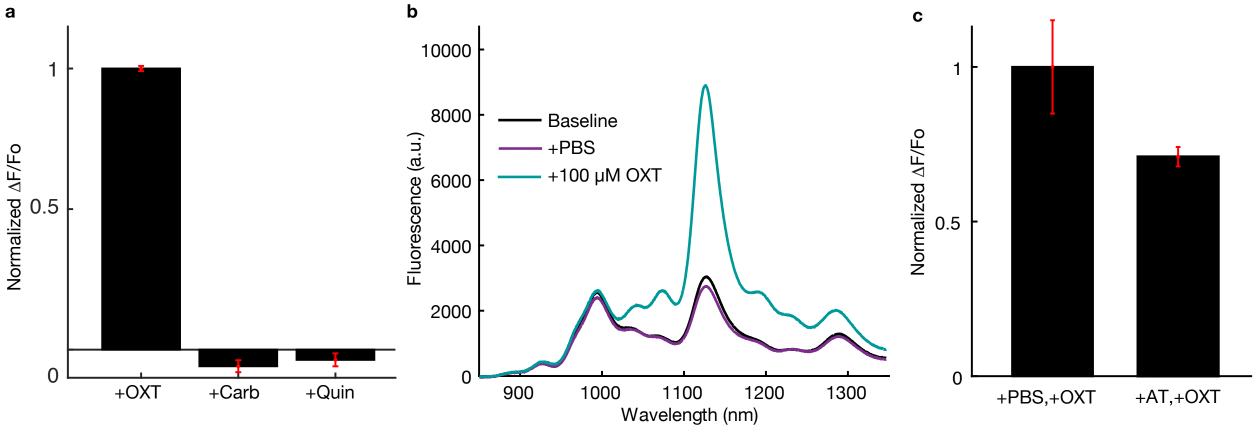

Figure 3.7 | nIROx *in vitro* pharmacological agent compatibility screening. a, nIROx optical response to 50 μM oxytocin (OXT), carbetocin (Carb), and quinpirole (Quin). Black bars represent the mean $\Delta F/F_o$ at 1126 nm from n=3 replicates normalized to OXT response, with standard deviation of these replicates shown in red. **b,** Full fluorescence spectra of nIROx before (black) and after the addition of PBS (purple), followed by the addition of 100 μM OXT (blue). **c,** nIROx optical response to 100 μM oxytocin after the addition of either 1X PBS or 100 μM atosiban (AT), an OXT receptor antagonist. Black bars represent the mean peak $\Delta F/F_o$ at 1126 nm from n=3 replicates, and red error bars represent the standard deviation from these replicates. nIROx response to OXT decreases by 28% upon incubation with atosiban.

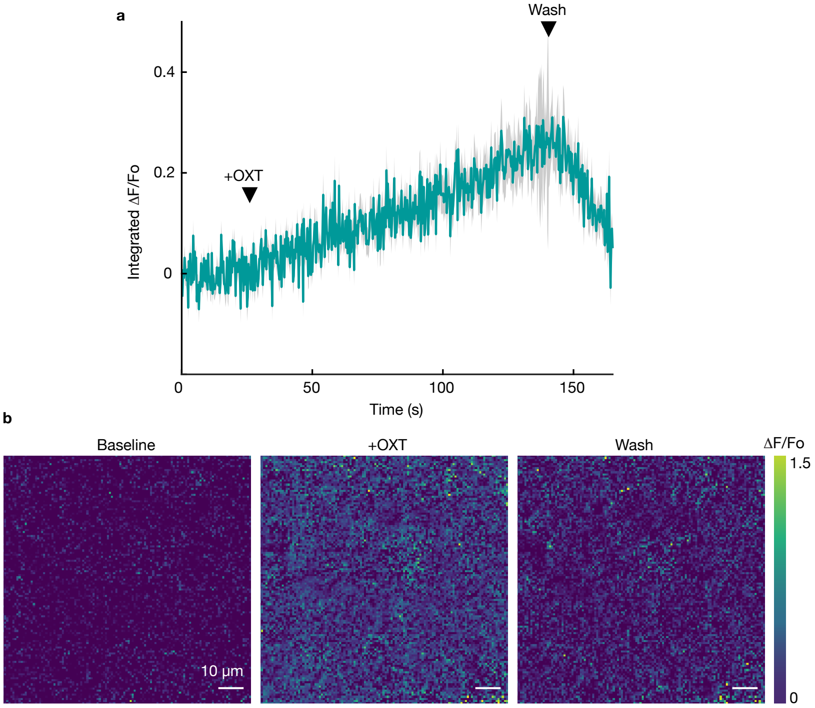

Figure 3.8 | nIROx nanosensor reversibility in brain tissue. a, *In slice,* mean time trace (blue) and standard deviation (gray) of integrated $\Delta F/F_o$ for nanosensors imbedded in an acute brain slice and exposed to an exogenous wash of 100 µM OXT. OXT was manually injected after 100 frames of baseline, and the slice was washed with an ACSF perfusion after 400 frames. nIROx sensitivity and reversibility upon immobilization is recapitulated in brain tissue. **b,** Three images within the same field of view of integrated $\Delta F/F_o$ of nIROx in the dorsal striatum. Three frames are represented: "baseline" is before the addition of oxytocin, "+OXT" after the addition of 100 µM exogenous oxytocin, and "wash" is after washing the slice with ACSF to remove oxytocin. Scale bars represent 10 µm.

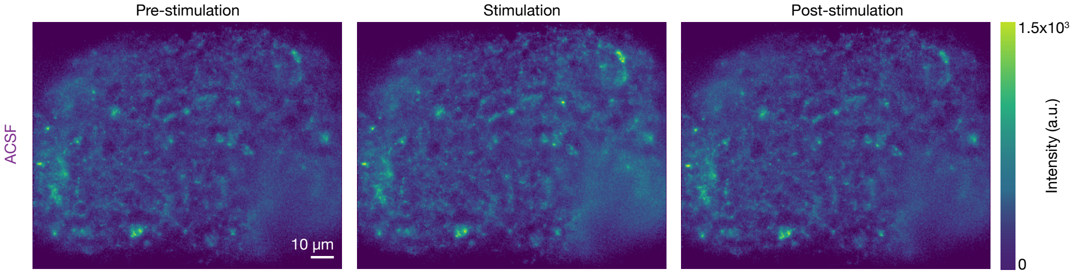

Figure 3.9 | Imaging oxytocin release evoked by electrical stimulation. *In slice,* three images within the same field of view of nIROx-labeled acute brain slices following a 0.5 mA single-pulse electrical stimulation in standard ACSF in the PVN. "Pre" is the baseline before electrical stimulation, "stim" is immediately following electrical stimulation, and "post" is after nanosensor fluorescence has returned to baseline. Scale bars represent 10 µm.

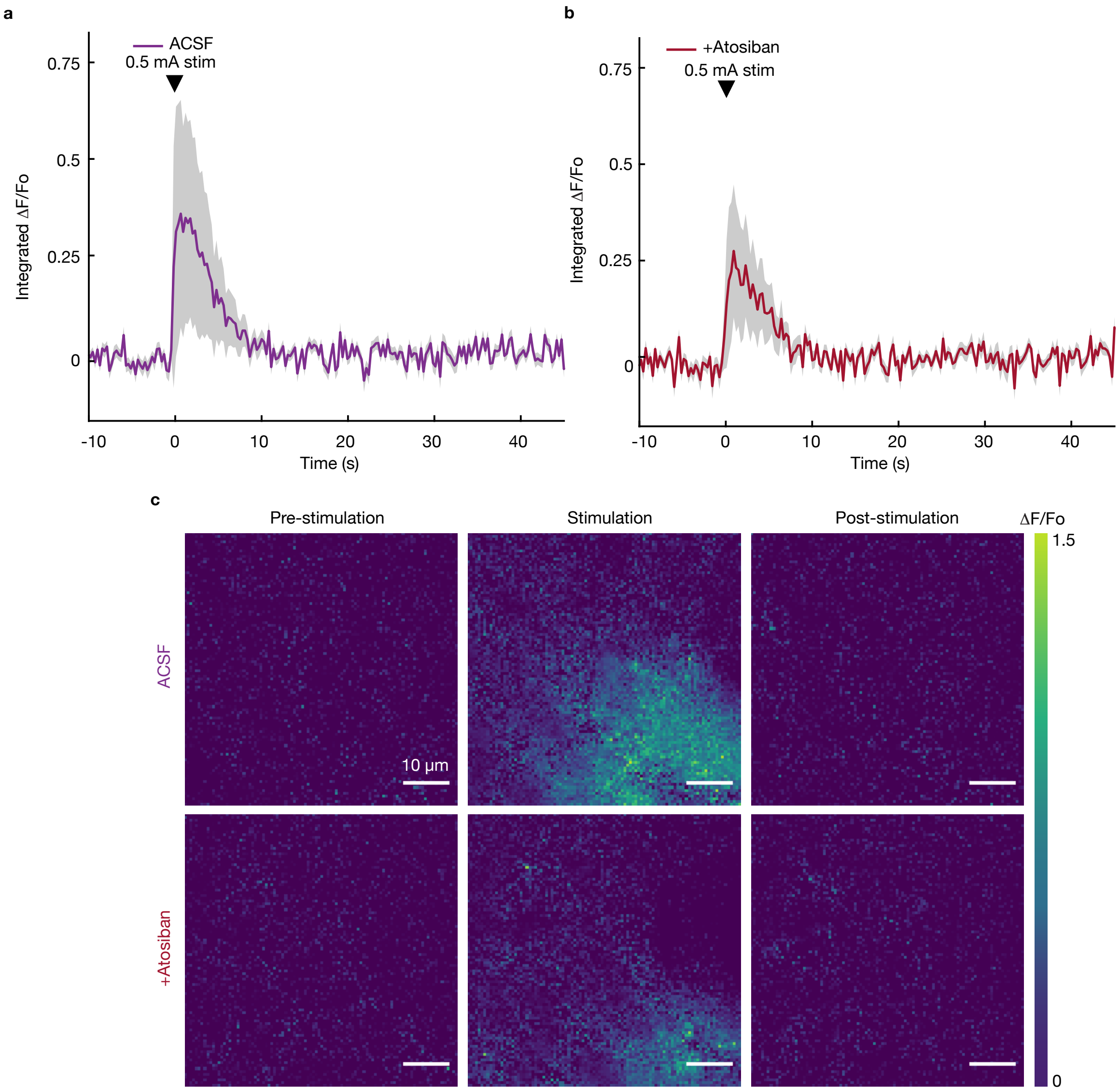

Figure 3.10 | Analysis of oxytocin release evoked by electrical stimulation and the effect of an oxytocin receptor antagonist in the paraventricular nucleus. a, *In slice,* mean time trace (purple) and standard deviation (gray) of integrated nanosensor $\Delta F/F_o$ for a single 0.5 mA electrical pulse stimulation in the PVN in standard ACSF. **b,** For the same brain slice, mean time trace (red) and standard deviation (gray) of integrated $\Delta F/F_o$ for a single 0.5 mA electrical pulse stimulation in 1 μM atosiban in ACSF. **c,** Three images within the same field of view of integrated $\Delta F/F_o$ of nanosensor after 0.5 mA electrical stimulation in standard ACSF (top) and 1 μM atosiban in ACSF (bottom). Three frames are represented: "pre" is the baseline before electrical stimulation, "stim" is immediately following electrical stimulation, and "post" is after nanosensor fluorescence has returned to baseline. Scale bars represent 10 μm.

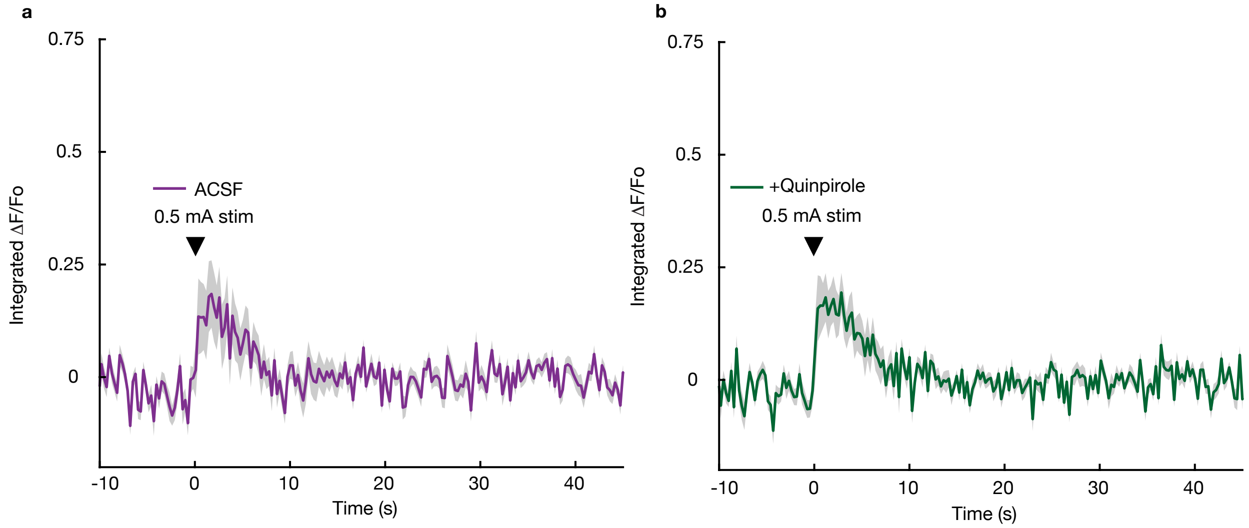

Figure 3.11 | Analysis of oxytocin release evoked by electrical stimulation and the effect of an D2/D3 receptor agonist in the paraventricular nucleus. a, *In slice,* mean time trace (purple) and standard deviation (gray) of integrated nanosensor $\Delta F/F_o$ for a single 0.5 mA electrical pulse stimulation in PVN in standard ACSF. **b,** Mean time trace (green) and standard deviation (gray) of integrated $\Delta F/F_o$ for a single 0.5 mA electrical pulse stimulation in PVN with 1 µM quinpirole in ACSF.

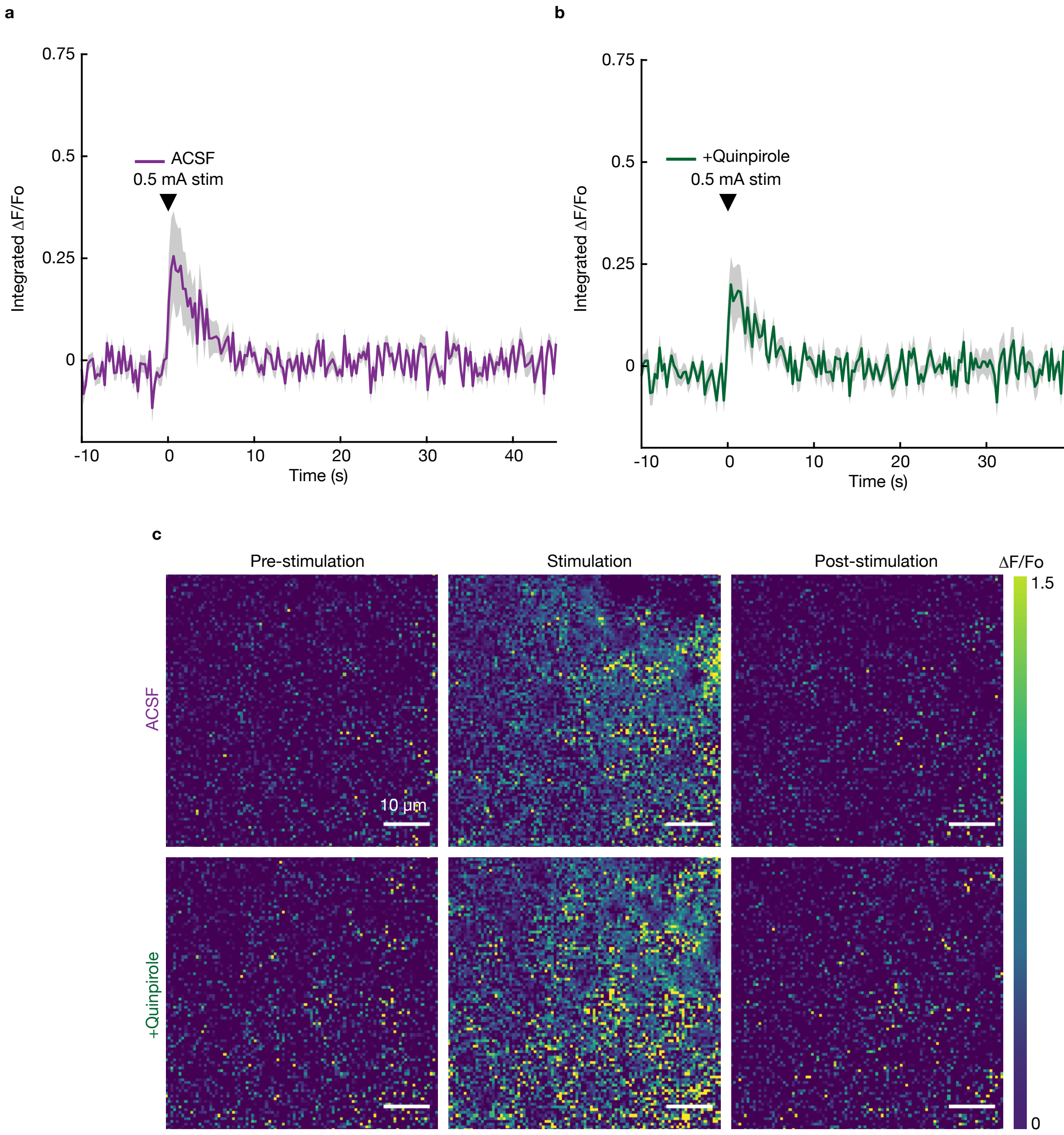

Figure 3.12 | Analysis of oxytocin release evoked by electrical stimulation and the effect of an D2/D3 receptor agonist in the paraventricular nucleus. a, *In slice,* mean time trace (purple) and standard deviation (gray) of integrated nanosensor $\Delta F/F_o$ for a single 0.5 mA electrical pulse stimulation in PVN in standard ACSF. **b,** Mean time trace (green) and standard deviation (gray) of integrated $\Delta F/F_o$ for a single 0.5 mA electrical pulse stimulation in PVN with 1 μM quinpirole in ACSF. **c,** Three images within the same field of view of integrated nanosensor $\Delta F/F_o$ following a single pulse 0.5 mA electrical stimulation in standard ACSF (top) and in 1 μM quinpirole in ACSF (bottom). Three frames are represented: "pre" is the baseline before electrical stimulation, "stim" is immediately following electrical stimulation, and "post" is after nanosensor fluorescence has returned to baseline. Scale bars represent 10 μm.

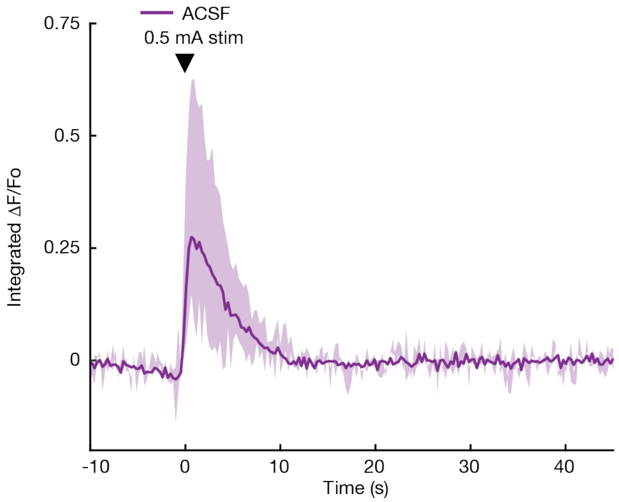

Figure 3.13 | Analysis of oxytocin release evoked by electrical stimulation. The range of mean integrated $\Delta F/F_o$ traces for twelve 0.5 mA electrical pulse stimulations across 4 biological replicates in standard ACSF are shown (light purple) to demonstrate variation in oxytocin release across stimulations and across acute slices in the PVN. The mean of these traces is shown in dark purple.

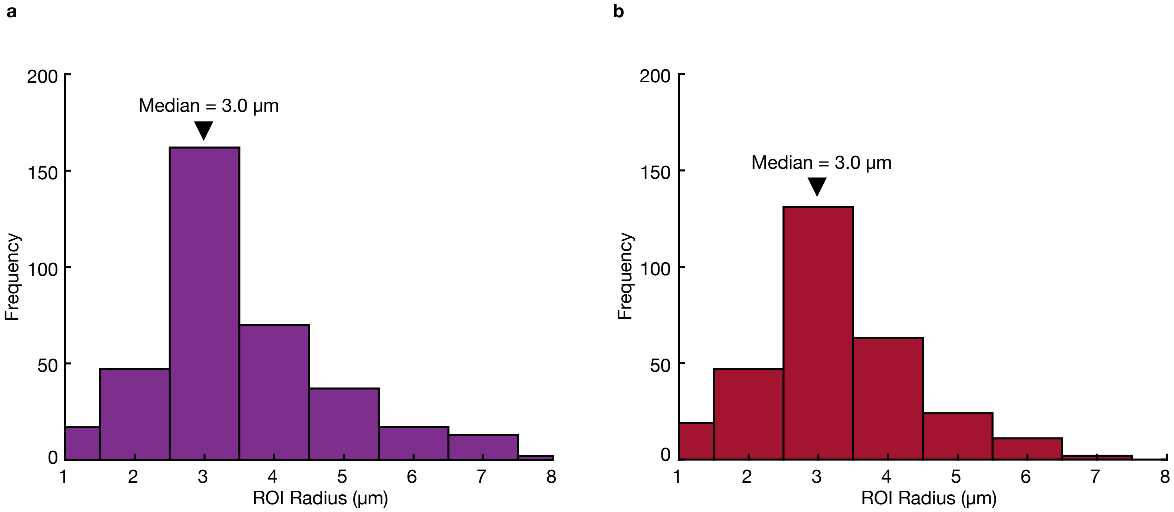

Figure 3.14 | Region of interest (ROI) analysis of acute slice images to characterize oxytocin release site features. a, Frequency histogram of ROI sizes across 6 stimulations of the PVN in ACSF. There are 366 total ROIs with a median size of 3 µm. **b,** Frequency histogram of ROI sizes across 6 stimulations of the PVN in 1 µM atosiban in ACSF. There are 297 total ROIs with a median size of 3 µm.

3.7 Future directions

While near-infrared oxytocin nanosensors (nIROx), as described above, are effective probes for imaging oxytocin release in acute brain slices, these nanosensors have two primary limitations: 1) dim baseline fluorescence which challenges nanosensor labeling and imaging in brain tissue and 2) poor selectivity against dopamine which limits the utility of nIROx to non-dopaminergic brain regions. It is our contention that nIROx imaging limitations are due to the use of the C_{12} ssDNA wrapper as a nanosensor dispersant. The recognition element of nIROx is an extremely hydrophobic peptide fragment of the endogenous oxytocin receptor. When covalently attached to the surface of SWCNT, this peptide alone is insufficient to disperse hydrophobic SWCNT in aqueous solutions. To impart colloidal stability, OXTp-SWCNT are noncovalently modified with single-stranded DNA. Via probe tip sonication, C_{12} ssDNA is adsorbed to the surface of OXTp-SWCNT to form nIROx nanosensors.

Oxytocinergic regions of the brain, such as the paraventricular nucleus of the hypothalamus (PVN) and supraoptic nucleus of the hypothalamus (SON), do not release large quantities of dopamine and are thus compatible with nIROx. However there are many oxytocinergic regions of interest, such as the nucleus accumbens[167] and hippocampus[168, 169], that are also dopaminergic[170, 171]. These regions could be potentially imaged with nIROx in conjunction with a dopamine-repressing pharmacological agent such as the D2 receptor agonist, quinpirole. Quinpirole treatment, however, may have unforeseen impacts on oxytocin signaling, as interplay between dopamine and oxytocin signaling has been previously demonstrated[172, 173].

Nearly all DNA wrapped SWCNT constructs respond to dopamine for reasons that are not fully understood[111, 174], and DNA is not the most effective dispersant of SWCNT[175]. A high-affinity non-DNA dispersant could potentially improve selectivity and simultaneously increase nanosensor baseline fluorescence to enhance nanosensor performance in brains. We propose the use of a peptide to replace the C_{12} wrapper of nIROx. Unlike surfactants, such as sodium cholate and sodium dodecyl benzenesulfonate, that are commonly used to disperse SWCNT in aqueous solutions, peptides are biocompatible and easily customizable.

Previous work has demonstrated the utility of peptides as SWCNT dispersants in various aqueous solutions and on solid phase. Hirano and colleagues demonstrated that poly-L-arginine can effectively disperse SWCNT in water, even when varying the pH[176]. Their molecular dynamics (MD) simulations indicated that the guanidinium group of each arginine residue aligns itself in parallel to the SWCNT sidewall to facilitate π- π interactions. Several phage-display studies have also been conducted to reveal new peptides and peptide motifs that have a high affinity for SWCNT. Peptides with the motif $X_1THX_2X_3PWTX_4$, where X_1 = G/H, X_2 = H/D/null, X_3 = R/null, X_4 = K/null, were shown to bind SWCNT[177]. Within the peptide library sharing this motif, the UW-1 peptide (LLADTTHHRPWT) and UW-4 peptide (CGIHPWTKC) were the best SWCNT dispersants in TBS buffer at 0.1% Tween-20. MD simulations of these peptide-SWCNT constructs showed that aromatic and hydrophobic peptide residues cluster to promote π- π interactions with SWCNT. Other phase display studies revealed that histidine- and tryptophan-containing peptides such as HWSAWWIRSNQS could disperse SWCNT in Tris buffer/Tween-20[178], and the A2 peptide (IFRLSWGTYFS) could disperse SWCNT better than both SDS and SC surfactants[179]. These phage display studies along with peptide modification studies have revealed the importance of aromatic residues, particularly tryptophan, for binding SWCNT. Samarajeewa et. al. evaluated the SWCNT-binding affinity of constructs containing an amphiphilic surfactant peptide ([X(V)$_5$(K)$_2$] and various terminal aromatic moieties to pin the peptide to the nanotube surface. Their finding suggest that the HOMO of the aromatic moieties acts as an electron donor and furthermore interact with the LUMO of SWCNT to facilitate binding[180]. Of all the aromatic moieties tested, tryptophan was shown to have the highest affinity for SWCNT. By modifying tryptophan residues to alanine in the UW-1 peptide, Su et. al. further supported these findings and determined that the HOMO of tryptophan interacts with the LUMO of SWCNT to pin the peptide to the nanotube surface[181].

Based on the studies above, we evaluated the viability of tryptophan-containing peptides as dispersants in nIROx. We prepared peptide-SWCNT constructs via probe tip sonication with the following peptides in water: A2 (IFRLSWGTYFS), UW-1 (LLADTTHHRPWT), and P1 (HWSAWWIRSNQS) (Figure 3.15). Both the UW-1 and P1 peptides failed to disperse SWCNT in water without the addition of surfactants, making them inviable for use in biological systems. The A2 peptide produced colloidally stable SWCNT with high yield. The resulting A2-SWCNT construct was not responsive to 50 μM dopamine when compared to C_{12}-SWCNT (Figure 3.16). Upon incorporation into nIROx, the baseline fluorescence was more than 500% brighter than that of nIROx prepared with the C_{12} wrapper (Figure 3.17). A2-nIROx constructs were unresponsive to dopamine at 100 μM, as expected, but were also insensitive to oxytocin at the same concentration (Figure 3.18). It is possible that the A2 peptide interfered with binding between the OXTp recognition element and oxytocin. Additionally, A2-SWCNT and A2-nIROx aggregated upon the addition of salt (0.1X PBS, 1X PBS, and 100 mM NaCl). These constructs were thus unusable as oxytocin nanosensors *in vivo.*

We suggest modification of the A2 peptide with a highly soluble terminal motif such as poly-glutamate (EEEE) to improve SWCNT dispersibility in biologically relevant ionic solutions. We also suggest the exploration of surfactant peptides for use in nIROx such as X(V)$_5$(K)$_2$ and E(QL)$_6$E. Identification of a peptide that can 1) effectively disperse SWCNT in ionic solutions, 2) does not interact with dopamine when bound to SWCNT, and 3) does not interfere with the molecular recognition of oxytocin in nIROx, would vastly expand the utility of nIROx as an oxytocin nanosensor in brains. With an increased baseline fluorescence and selectivity, nIROx can be leveraged to image oxytocin release throughout the brain in oxytocinergic/dopaminergic regions such as the nucleus accumbens and hippocampus. This would enable us to characterize oxytocin signaling throughout the brain and understand the physiological underpinnings of oxytocin-related neurological disorders.

A2

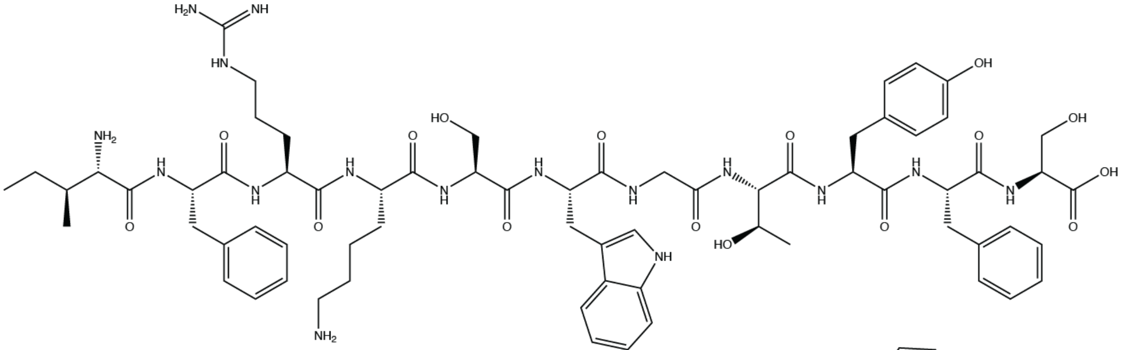

UW-1

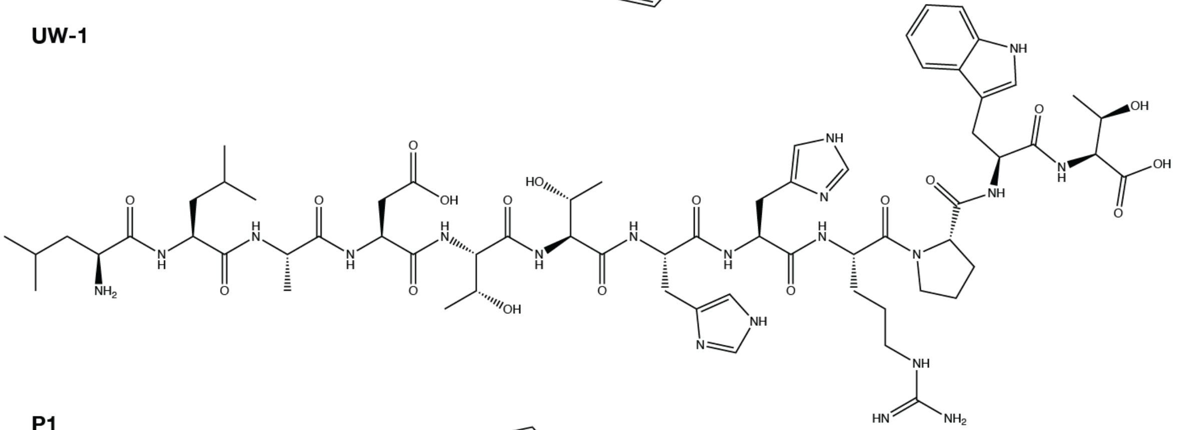

P1

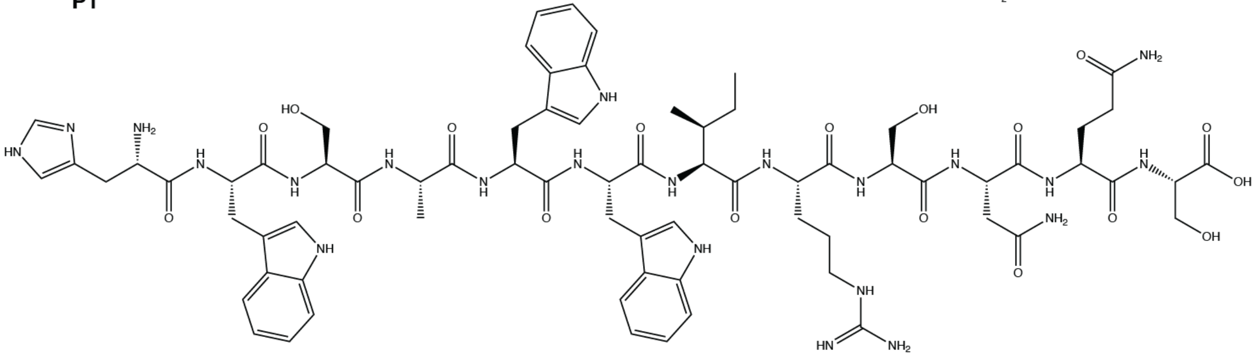

Figure 3.15 | SWCNT binding peptides. Sequence and structure of the A2, UW-1, and P1 peptides.

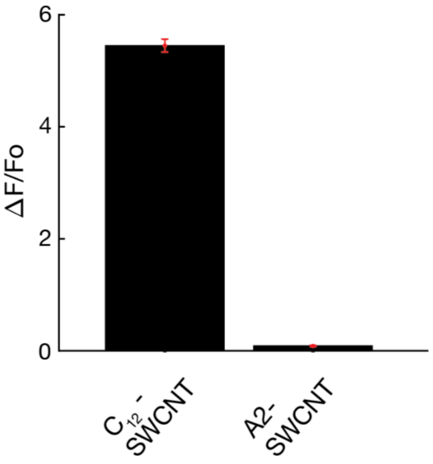

Figure 3.16 | C_{12}-SWCNT versus A2-SWCNT dopamine response. Nanosensor optical response to 50 μM dopamine in water. Black bars represent the mean peak $\Delta F/F_o$ at 1126 nm from n=3 replicates, and red error bars represent the standard deviation from these replicates. A2-SWCNT response to dopamine is negligible.

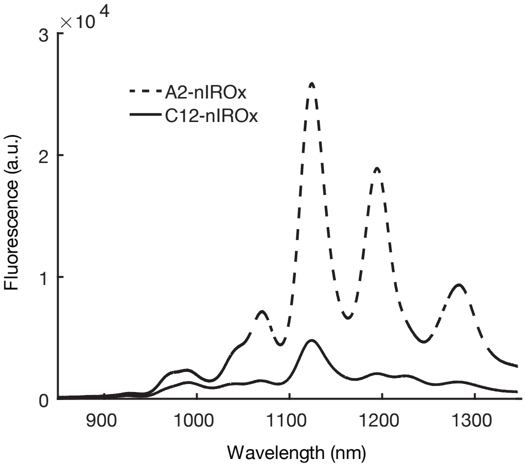

Figure 3.17 | Baseline fluorescence of nIROx prepared with C_{12} ssDNA or A2 peptide. Full fluorescence spectra of nIROx prepared with C12 ssDNA in 1X PBS (black dotted) or A2 peptide in water (black solid). nIROx prepared with A2 peptide is ~500% brighter than the original nanosensor.

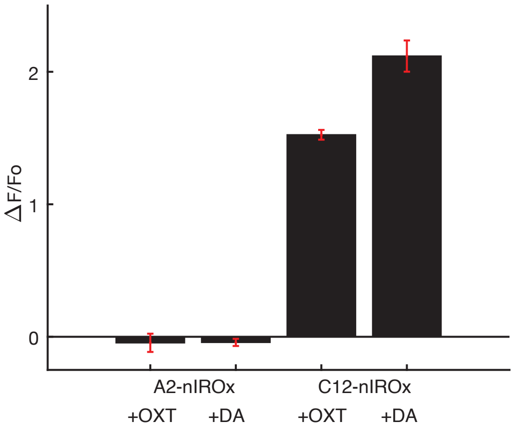

Figure 3.18 | Nanosensor oxytocin and dopamine response. Nanosensor optical response to 100 μM oxytocin and dopamine. Black bars represent the mean peak $\Delta F/F_o$ at 1126 nm from n=3 replicates, and red error bars represent the standard deviation from these replicates. A2-nIROx response to both oxytocin and dopamine is negligible.

Chapter 4

High throughput evolution of near-infrared oxytocin nanosensors

4.1 Abstract

While the importance of neuropeptide oxytocin in mediating our social well-being is widely understood, we currently lack effective tools for imaging oxytocin signaling in the brain. To characterize oxytocin function and its role neurological health and disease requires real-time imaging probes with the spatiotemporal resolution compatible with endogenous oxytocin release and reuptake dynamics. To address this challenge, we have leveraged an evolution-based platform, SELEC, to identify a synthetic oxytocin imagine probe, nIROSE (near-infrared oxytocin nanosensor identified by SELEC). nIROSE nanosensors utilize an evolved ssDNA molecular recognition moiety adsorbed to the surface of near-infrared fluorescent single-walled carbon nanotubes (SWCNT) to image oxytocin. nIROSE nanosensors are easy to synthesize, demonstrate nanomolar sensitivity to oxytocin, and are compatible with oxytocin receptor-targeted pharmacology. Preliminary imaging experiments in acute tissue slices suggest that nIROSE can reversibly image electrically stimulated oxytocin release in brains. nIROSE and nIROx (Chapter 3) nanosensors are complementary tools, and together may enable real-time imaging of oxytocin signaling throughout the brain.

4.2 Introduction

As illustrated in Chapters 3 and 4, neuropeptide oxytocin plays a critical role in mediating our social cognition and behaviors. In recent years, incredible progress has been made towards understanding oxytocin function in the brain, from brain-wide mapping of oxytocin neuronal circuitry[182] to solving the crystal structure of the human oxytocin receptor[140] and characterizing the therapeutics effects of oxytocin on individuals with autism spectrum disorder (ASD)[183]. Immunohistochemistry, mRNA, and receptor binding studies of brain tissue have revealed where and when oxytocin and its receptor are expressed over the course of development, between the sexes, and among different mammalian species[184, 185]. Even with these strides, however, fundamental questions about oxytocin signaling remain unanswered. To fully characterize the spatiotemporal dynamics of oxytocin release and reuptake in the brain requires an imaging platform with the selectivity, sensitivity, and resolution requisite to capture endogenous oxytocin signaling events.

Towards this end, we have developed a near-infrared oxytocin nanosensor (nIROx) as described in Chapter 3[123]. This covalent peptide-SWCNT conjugate is the first real-time synthetic imaging probes capable of distinguishing between vasopressin and oxytocin in the brain. Unlike currently available GPCR-based sensors, nIROx can image oxytocin release events with selectivity over neuropeptides that also bind its receptor. The strategy used to develop nIROx, however, does not easily translate to other neuropeptide targets. To synthesize nIROx, we covalently conjugated a previously identified oxytocin receptor peptide fragment that binds oxytocin with high affinity. Such neuropeptide-binding peptides have not been identified for all neuropeptide targets. nIROx also requires a complicated multi-day synthesis and is only stable for 8 days after synthesis. nIROx synthesis may therefore be intractable for users without synthetic organic chemistry expertise and tools, and nanosensors would be difficult to synthesize and share across labs within its viability window.

To address these challenges, we have leveraged an evolution-based strategy to identify ssDNA-SWCNT constructs with high affinity for oxytocin. These nanosensors are easy to synthesize, stable for months, and perform comparably to the nIROx nanosensors described in Chapter 3. Furthermore, we demonstrate that our evolution-based strategy can be easily modified and translated to structurally complex targets to enable the identification of nanosensors for any neurochemical of interest.

4.3 Results and discussion

4.3.1 SELEC enables high-throughput screening of ssDNA-SWCNT for neuropeptide oxytocin sensitivity

Prior work has demonstrated the utility of noncovalent ssDNA-SWCNT as nanosensors for neurochemical imaging applications[118]. Traditionally, constructs with optical sensitivity to neurochemicals of interest have been identified through a low-throughput screening approach, where a library of ssDNA aptamer-SWCNT constructs are individually synthesized and subsequently screened for fluorescence response to the analyte[142, 174]. This strategy has yielded nanosensors for analytes such as catecholamines. $(GT)_6$-SWCNT (nIRCats) can image dopamine release in striatal brain tissue[19, 143] and, more recently, at single dopamine release sites in neuronal soma and dendrites[144]. Structurally complex targets, such as neuropeptides, have heretofore eluded heuristic, guess-and-test approaches.

More recently, our lab has developed a high-throughput screening approach, termed SELEC, that enables co-evolution of molecular recognition ssDNA sequences with signal-transducing SWCNT[120]. This approach has been employed successfully to develop ssDNA-SWCNT nanosensors for selective and reversible serotonin imaging in brain slices. Machine learning strategies, using the sequencing and optical screening data from SELEC, have yielded nanosensors with even higher sensitivity towards serotonin[186]. To show SELEC can be applied to large biopolymer targets that have eluded low-throughput screening approaches, we adapted our original SELEC protocol to evolve ssDNA-SWCNT for neuropeptide oxytocin sensing (Figure 4.1).

Systematic evolution of ssDNA ligands by exponential enrichment following adsorption to carbon nanotubes (SELEC) was inspired by the SELEX protocols developed in 1990[187, 188]. We implemented SELEC to identify ssDNA-SWCNT constructs that both bind and optically respond to oxytocin. We designed our initial library with 6.9×10^{10} unique and random 18-mer DNA aptamers flanked by polycytosine (C_6) and PCR primers. The 6-mer polycytosine region was introduced to pin ssDNA aptamers to the SWCNT surface; this sequence was previously demonstrated to have a high affinity for carbon nanotubes[147]. The PCR primers were included to enable enzymatic amplification and enrichment of oxytocin- and SWCNT-binding ssDNA aptamers.

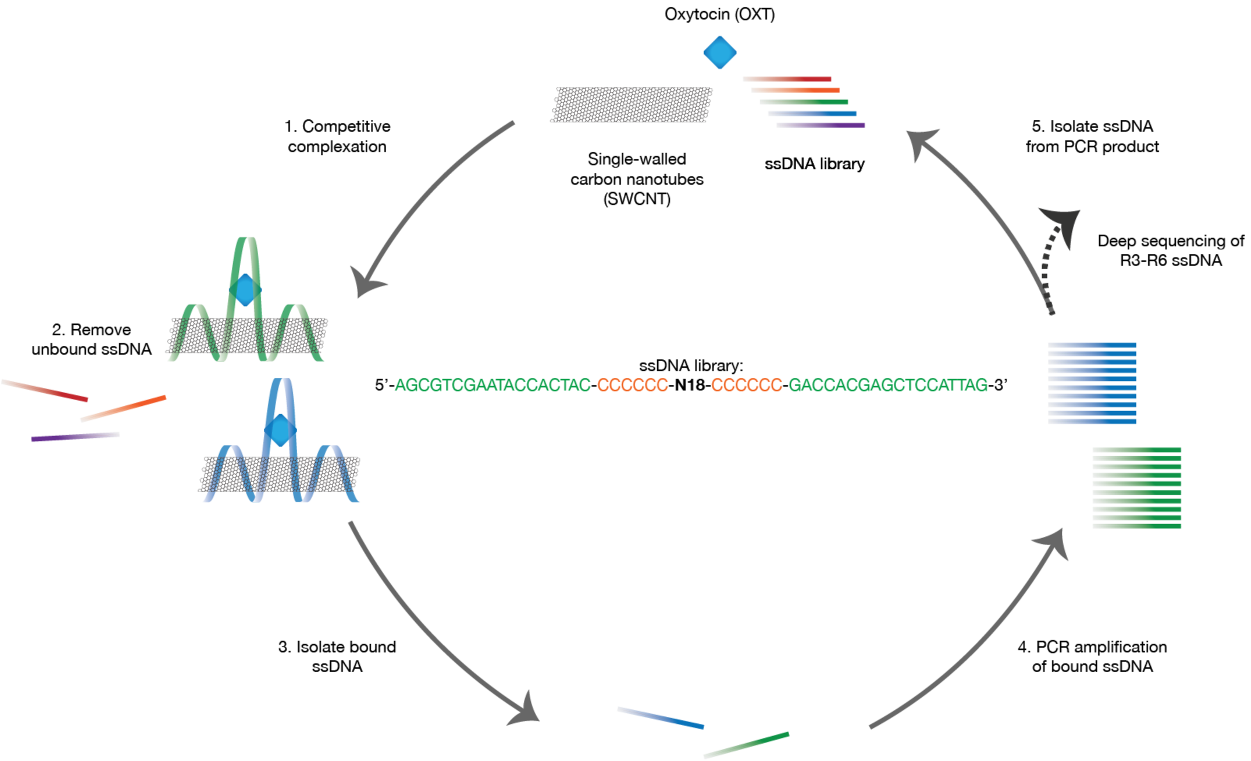

Figure 4.1 | SELEC schematic and ssDNA library composition. In one round of SELEC, ssDNA is mixed with SWCNT and oxytocin. The mixture is probe-tip sonicated to competitively complex ssDNA to the SWCNT surface. Unbound ssDNA is removed, and bound ssDNA is isolated for PCR amplification. ssDNA is isolated from the dsDNA PCR product and prepared for the next round of SELEC. ssDNA sequences from rounds 3-6 are prepared and submitted for deep sequencing.

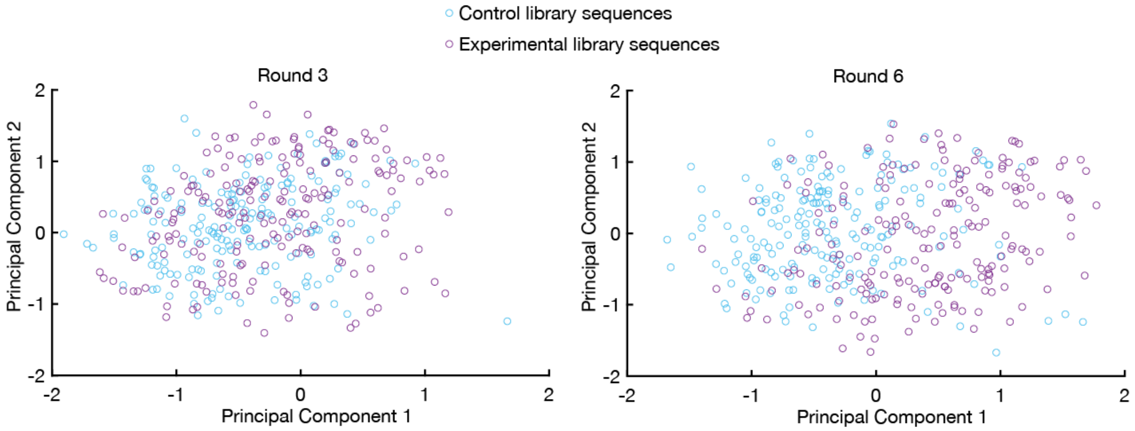

Figure 4.2 | Principal component analysis of experimental and control libraries. Plot of principal component 2 versus principal component 1 of experimental and control library ssDNA sequences from rounds 3 (left) and 6 (right) of SELEC. Each circle represents a single ssDNA sequence. In round 3, the sequence composition between the experimental and control libraries is similar, but by round 6, these libraries begin to diverge. This divergence is likely due to the presence of oxytocin and is indicative of successful library evolution.

Using an excess of ssDNA, the aptamer library was adsorbed onto SWCNT via sonication in the presence of oxytocin. This protocol was designed to both 1) promote competitive complexation of aptamers to SWCNT and 2) enrich ssDNA aptamers with a high affinity for oxytocin when bound to the SWCNT surface. Following competitive complexation, unbound ssDNA sequences were removed. Bound ssDNA sequences were subsequently desorbed, amplified by PCR, and isolated before use in subsequent rounds of SELEC. We found that six rounds of SELEC were sufficient to enable divergence between the control and experimental libraries (Figure 4.2) and to identify oxytocin nanosensor candidates. ssDNA sequences from rounds 3-6 of SELEC were prepared and submitted for deep sequencing with an Illumin HiSeq 4000. Previous work was conducted to produce and sequence a control library, wherein SELEC was conducted in the absence of a target analyte. Control SELEC was used to identify ssDNA aptamers that only have a high affinity for the SWCNT surface, not the target analyte, or are subject to PCR biases[189].

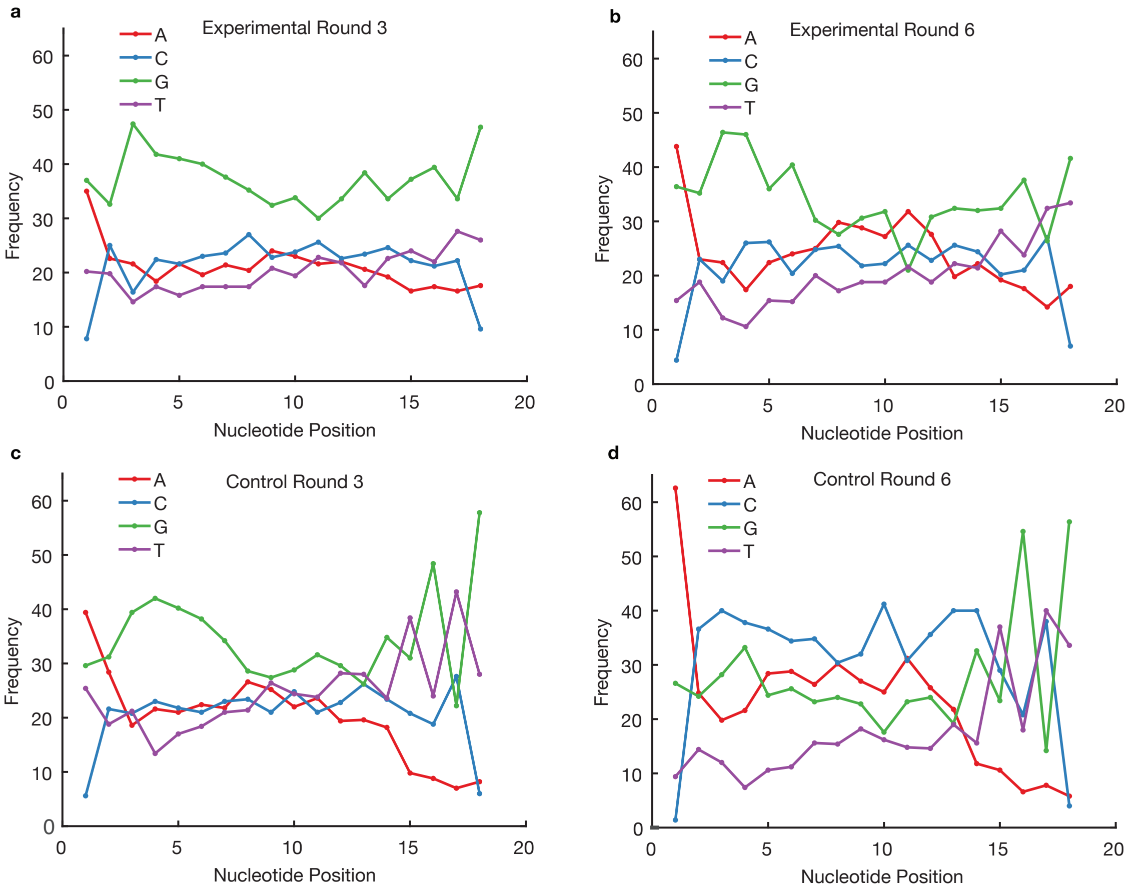

Figure 4.3 | Nucleotide frequency by position. a-d, The percent frequency of each nucleotide, A (adenosine), C (cytosine), G (guanine), and T (thymine), was calculated as a function of position along the 18-mer in the top 500 most enriched sequences in SELEC rounds 3 and 6 in both experimental and control libraries. This analysis provides insight into the aptamer characteristics that enable binding of oxytocin versus the carbon nanotube surface.

The most enriched 500 sequences from each round of SELEC were identified after filtering sequences that did not contain the expected 18-mer, polycytosine, and PCR primer regions. The top 50 sequences from both experimental and control rounds 3-6 and can be found in Tables 4.1, 4.2, 4.3, and 4.4; the polycytosine and PCR primer regions have been excluded for clarity. Comparative analyses between control and experimental ssDNA sequences were conducted to identify nucleotides and nucleotide motifs that may be important for oxytocin molecular recognition.

We first calculated nucleotide frequency as a function of position along the 18-mer (Figure 4.3) to understand the aptamer characteristics associated with oxytocin versus SWCNT binding. Furthermore, this type of analysis may facilitate the intelligent design of a ssDNA-SWCNT oxytocin nanosensor, as discussed in Chapter 4.7 Future Directions. Across all rounds and libraries, a few trends were observed in the top 500 ssDNA sequences, namely a strong preference for adenosine at position 1 and guanosine at position 18 and a low occurrence of cytosine at positions 1 and 18. As these trends are agnostic to the presence of oxytocin, they provide insight into the aptamer characteristics that facilitate SWCNT-binding, not oxytocin affinity. While guanosine frequency is high at positions 3 and 4 in round 3 of both libraries, this trend is diminished by round 6 of the control library and sustained by round 6 of the experimental library. It is likely that the presence of guanosine at these positions is critical to oxytocin binding.

We conducted additional analyses in which we identified high frequency 3-mer motifs and tracked their frequency, enrichment, and position across rounds of evolution. The incidence of trimer motifs in the top 500 ssDNA sequences is summarized in Tables 4.5-4.6 and their percent enrichment between rounds of SELEC is summarized in Tables 4.7-4.8. From this analysis, a few notable trends emerge. Polycytosine was selected as a flanking sequence and aptamer anchor due to its high affinity for SWCNT but was not present at high frequency in either experimental or control libraries. The CAC motif was present in the control libraries at high frequency and was greatly enriched across rounds of control SELEC. This motif likely has a high affinity for the SWCNT surface, but not oxytocin. Across all rounds of SELEC in the experimental library, GTG is the most prevalent trimer. This motif is also among the top 10 most prevalent motifs in the control library across SELEC rounds 3, 4, and 6. Many high frequency trimers are shared across control and experimental libraries, including ACG and GCA, suggesting their importance for both SWCNT and oxytocin binding.

Trimer motifs such as GGC and AGG, however, are enriched in all rounds of the experimental library, but are not present in top 25 most frequent motifs after round 3 in the control library. The increase in enrichment of GGC and AGG trimers throughout experimental SELEC rounds and decrease in enrichment in control SELEC rounds, indicate the importance of these trimers for oxytocin molecular recognition. As shown in Figure 4.4, the frequency of GGC and AGG is position dependent. The GGC and AGG motifs are most enriched at positions 1-3 of the 18-mer, with a frequency greater than 1% at these positions. The frequencies of a subset of 3-mer motifs as a function of position in control and experimental ssDNA libraries are summarized in Tables 4.9-4.16. These analyses have enabled identification of high frequency trimer motifs, and furthermore, may facilitate the intelligent design of ssDNA-SWCNT oxytocin nanosensors with higher oxytocin sensitivity than that of the nanosensors identified by SELEC and described herein.

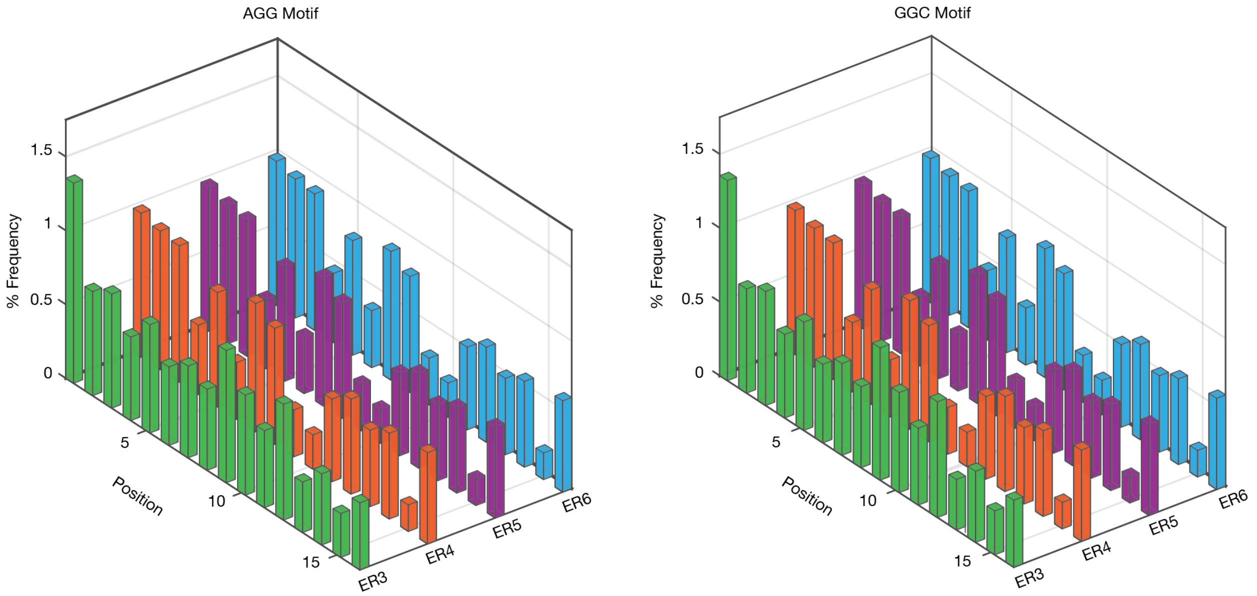

Figure 4.4 | Frequency versus position for 3-mer motifs. The percent frequency of the AGG motif (left) and GGC motif (right) across rounds of SELEC in the experimental libraries. Both motifs are observed at high frequency in the experimental libraries, but not the control libraries. These motifs likely have a high affinity for the target analyte, oxytocin, when adsorbed to the SWCNT surface.

4.3.2 In vitro characterization of oxytocin nanosensors

We then evaluated the sensitivity of evolved ssDNA aptamers towards oxytocin when adsorbed to the SWCNT surface. The sequences from experimental rounds are denoted as EN#M and those from control rounds are denoted as CN#M where N is the round of evolution (3-6) and M is the order of frequency (1-10). The sequence E6#4 is therefore the 4th most enriched ssDNA aptamer in the experimental library from the 6th round of evolution with SELEC. ssDNA-SWCNT nanosensor candidates were synthesized with C3-6#1-5, E3-4#1-5, and E5-6#1-10 sequences. The top 10 ssDNA sequences from rounds 5 and 6 of experimental SELEC were used for nanosensor synthesis as sequences from these rounds were expended to have higher affinity for oxytocin than those from rounds 3 and 4. Nanosensor candidates were synthesized with the 18-mer and polycytosine sequences but without the PCR primer region to increase the density of molecular recognition moieties on the SWCNT surface. Previous work demonstrated that nanosensors synthesized with C_6-N18-C_6 have a higher sensitivity for the target analyte than those synthesized with primer-C_6-N18-C_6-primer sequences[120].

ssDNA-SWCNT nanosensor candidates were prepared by mixing ssDNA aptamer (100 μM, C_6-N18-C_6) with SWCNT (0.2 mg) in 1X PBS and adsorbing aptamers to the SWCNT surface via probe-tip sonication. All ssDNA sequences successfully suspended SWCNT in high yield. The nanosensors were then diluted to 5 mg/L SWCNT in PBS before use in fluorescence experiments. Nanosensor optical response is reported as $\Delta F/F_o = (F - F_o)/F_o$, where F_o is the peak fluorescence after PBS incubation, and F is the peak fluorescence after analyte incubation. Nanosensor response to oxytocin was wavelength-dependent (Figure 4.5), where the highest sensitivity to oxytocin was observed at the 1195 nm peak. This wavelength corresponds to the (8,6) SWCNT chirality[190] and was used for all $\Delta F/F_o$ calculations for consistency.

The response of nanosensor candidates as a function of SELEC round in both experimental and control libraries is summarized in Figure 4.6. Nanosensors prepared with control library sequences responded to oxytocin with a mean $\Delta F/F_o = 0.15 \pm 0.05$ and a maximum $\Delta F/F_o = 0.28 \pm 0.05$, while those prepared with experimental library sequences responded to oxytocin with a mean $\Delta F/F_o = 0.41 \pm 0.19$ and a maximum $\Delta F/F_o = 1.05 \pm 0.04$. The high responsivity of nanosensors prepared with sequences from the experimental library compared to those from the control library indicate that these sequences were successfully evolved via SELEC to bind oxytocin. All ssDNA-SWCNT constructs with a $\Delta F/F_o > 50\%$ were identified through SELEC rounds 5 and 6, with E6#4-SWCNT demonstrating the largest optical response to oxytocin. These data show that across rounds of SELEC, experimental sequences evolve a stronger affinity for and a larger optical response to oxytocin.

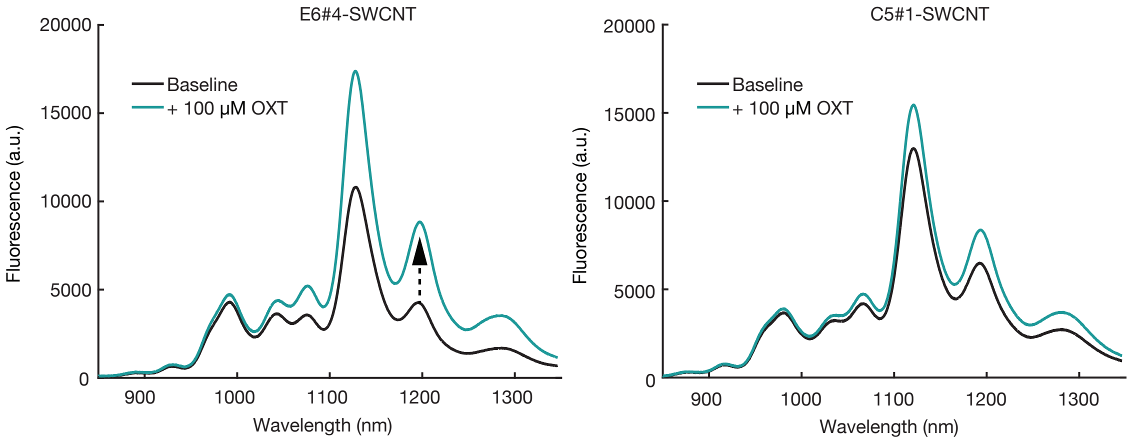

Figure 4.5 | Nanosensor fluorescence spectra and oxytocin optical response. The full fluorescence spectrum of E6#4-SWCNT (left) and C5#1-SWCNT (right) before (black) and after (blue) the addition of 100 μM oxytocin (OXT) in PBS. E6#4-SWCNT and C5#1-SWCNT are the two most responsive ssDNA-SWCNT constructs from the experimental and control libraries, respectively. The maximum turn-on fluorescence response is observed at the center wavelength of the (8,6) SWCNT chirality (~1195 nm).

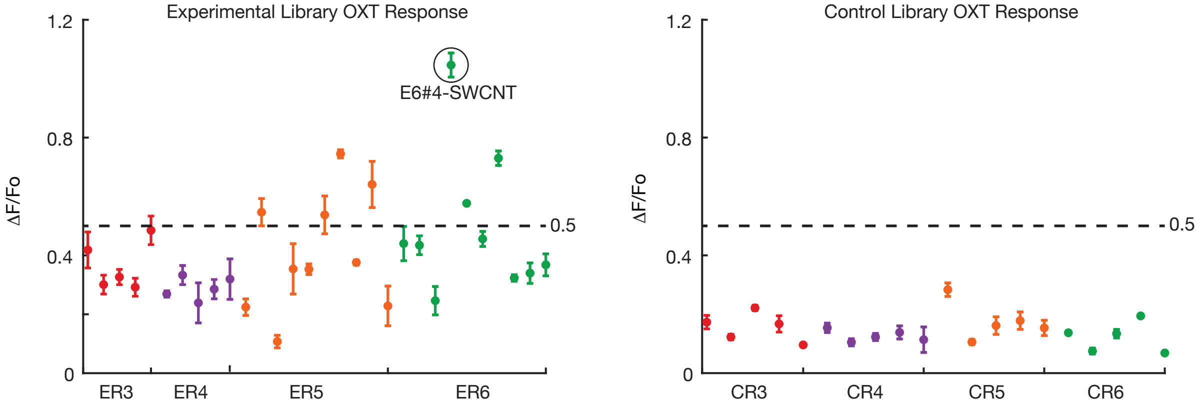

Figure 4.6 | Initial screening of nanosensor candidates. Nanosensors were prepared with the most enriched sequences from SELEC round 3 (red), round 4 (purple), round 5 (orange), and round 6 (green) of the experimental (left) and control (right) libraries. Circles represent the mean $\Delta F/F_o$ at 1195 nm from n=3 replicates with standard deviation of these replicates shown. $\Delta F/F_o$ is reported 20 minutes after incubation with 100 μM oxytocin (OXT). Seven nanosensor candidates, all from experimental SELEC rounds 5 and 6, responded with $\Delta F/F_o > 50\%$.

As the most responsive nanosensor candidate, E6#4-SWCNT was used for all subsequent optical characterization and renamed nIROSE (near-infrared oxytocin nanosensor identified by SELEC). nIROSE nanosensors respond to oxytocin in a concentration-dependent manner with nanomolar sensitivity (Figure 4.7a). We next calculated nanosensor kinetic parameters by fitting nIROSE response versus oxytocin concentration to a cooperative binding model[149], resulting in an equilibrium dissociation constant (K_d) of 4.93 μM (Chapter 4.6.1 Supporting Equations). These data suggest that nIROSE bind to oxytocin with even higher affinity than nIROx (described in Chapter 3).

To characterize nanosensor selectivity, nIROSE optical response was evaluated for a panel of neurochemicals including: vasopressin, dopamine, ɣ-aminobutyric acid (GABA), glutamate, and thyrotropin-releasing hormone (TRH) (Figure 4.7b, Figure 4.12). As expected, nIROSE responded significantly to dopamine relative to oxytocin [$\Delta F/F_o = 1.17 \pm 0.07$ (mean ± SD)]. Nearly all ssDNA-SWCNT constructs demonstrate optical sensitivity to dopamine, which limits nIROSE use to either nondopaminergic brain regions or requires dopamine-suppressing pharmacology when probing dopaminergic regions. nIROSE is moderately sensitive to the oxytocin analogue vasopressin $\Delta F/F_o = 0.30 \pm 0.21$ (mean ± SD), giving this probe comparable neuropeptide selectivity to all currently developed endogenous oxytocin imaging platforms but with the real-time temporal resolution offered by SWCNT-based neuroimaging probes. nIROSE is selective against thyrotropin-releasing hormone [$\Delta F/F_o = 0.056 \pm 0.018$ (mean ± SD)], which is co-released in hypothalamus alongside oxytocin[150, 151].

To explore nIROSE compatibility with pharmacology, nanosensor optical response was tested for four oxytocin receptor-targeted drugs (Figure 4.7b, Figure 4.12). While nIROSE fluorescence was quenched upon incubation with TC-OT 39, an oxytocin receptor agonist [$\Delta F/F_o = -0.48 \pm 0.02$ (mean ± SD)], quenching was diminished over time (Figure 4.10). These data suggest that nIROSE may be compatible with longer incubation of TC-OT 39 (>60 minutes). nIROSE fluorescence modulation was negligible upon treatment with atosiban, an oxytocin receptor antagonist, carbetocin, an oxytocin analogue and receptor agonist, and L-368,899, an oxytocin receptor antagonist, with a mean $\Delta F/F_o \leq 10\%$. These data suggest that our nanosensor can be leveraged to explore potential oxytocin signaling changing induced by these pharmacological agents.

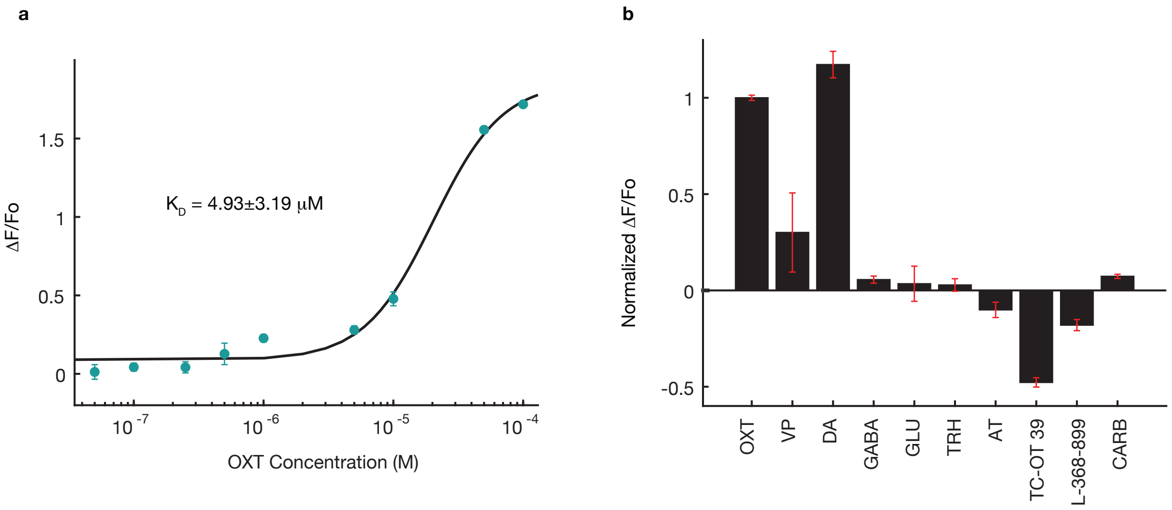

Figure 4.7 | Characterization of nIROSE nanosensors. a, Dose response curve of nIROSE for OXT. Blue circles and error bars represent the mean of n=3 experimental measurements and the standard deviation of these measurements, respectively. $\Delta F/F_o$ is calculated from the normalized change in peak intensity at 1195 nm after 20 minutes. The black line represents the cooperative binding model fit to experimental data. The K_d value is reported with 95% confidence intervals using the t-distribution. **b,** nIROSE selectivity screening at 50 μM oxytocin (OXT), vasopressin (VP), dopamine (DA), glutamate (GLU), γ-aminobutyric acid (GABA), thyrotropin-releasing hormone (TRH), atosiban (AT), TC OT 39, L-368,899, and carbetocin (CARB). Black bars represent the mean $\Delta F/F_o$ at 1195 nm from n=3 replicates normalized to OXT response after 20 minutes, with standard deviation of these replicates shown in red.

4.3.3 Nanosensor immobilization on glass and acute brain slices

Before introducing nIROSE into brain slices, nanosensors were immobilized on glass using a previously described drop-casting method[149] to evaluate their utility as oxytocin imaging probes on solid substrates. We tracked the integrated fluorescence of nIROSE during an initial wash with 1X phosphate buffered saline (PBS), followed by addition of 50 μM oxytocin (Figure 4.8). As expected, PBS had a negligible effect on nIROSE fluorescence, while the addition of oxytocin resulted in an immediate and sustained increase in integrated fluorescence [$\Delta F/F_o = 0.45 \pm 0.11$ (mean ± SD)]. Each nanosensor, represented by grey traces in Figure 4.8a, maintained its fluorescence over continuous laser illumination over the course of the 300 second experiment without photobleaching. These data suggest that nIROSE can bind and optically respond to oxytocin without signal attenuation on solid substrates.

nIROSE were then introduced into the paraventricular nucleus (PVN) of mouse brain slices. The PVN was selected for imaging experiments due its high density of oxytocinergic neurons as detailed in Chapter 3.3.2. Acute coronal mouse brain slices were prepared and imaged as described in Chapter 3.3.2. nIROSE nanosensors successfully and evenly labeled the PVN and maintained a baseline fluorescence nearly 500% brighter than that achieved with nIROx (Figure 4.9a). While nIROx demonstrates superior selectivity towards oxytocin, nIROSE has a stronger fluorescence signal in tissue. These SWCNT-based nanosensors can thus be used as complimentary tools with advantages for different applications. nIROx nanosensors may be advantageous in regions of the brain where oxytocin release, and thus fluorescence modulation, is expected to be high, whereas nIROSE might be preferable in regions where oxytocin is released in smaller quantities and are therefore signal limited.

To investigate nIROSE imaging efficacy following electrically stimulated oxytocin release, we employed a bipolar stimulating electrode and applied a 0.5 mA, 1 millisecond single square pulse within the PVN for 1 technical replicate. Electrical stimulation evoked an instantaneous increase in nIROSE fluorescence [$\Delta F/F_o = 0.16 \pm 0.19$ (means ± SD); $n = 58$] as shown in Figure 4.9b. While nIROSE response to oxytocin in slice was lower than that observed with nIROx nanosensors, the stimulating electrode used during nIROSE experiments was likely damaged, providing a weaker electrical pulse than expected. These slice data also demonstrate that nIROSE binding and response to oxytocin is reversible, which can enable imaging of multiple oxytocin release events. This single replicate serves as a proof of concept that nIROSE can image electrically stimulated oxytocin release in slice but is not representative of nIROSE performance under normal experimental conditions. Further technical and biological replicates are needed to fully characterize nIROSE performance in acute brain slices.

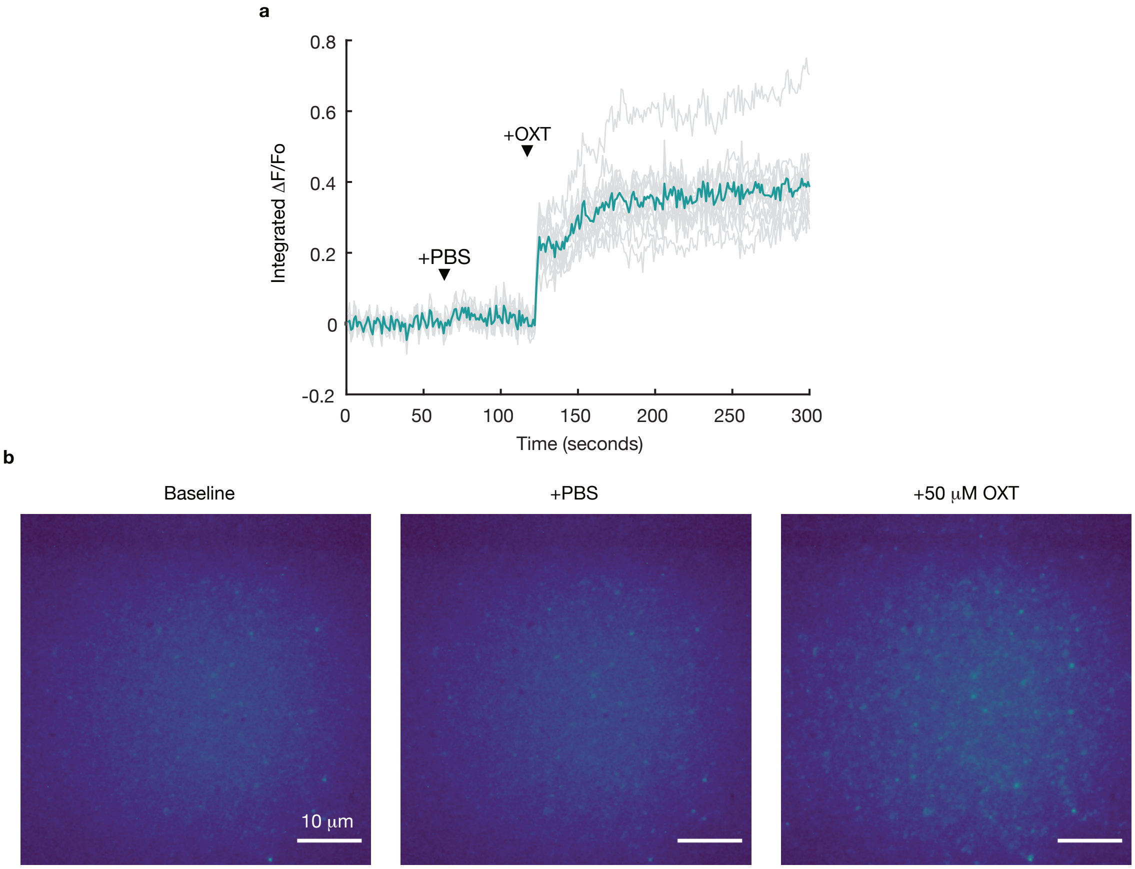

Figure 4.8 | Oxytocin imaging on solid substrates. a, *In vitro* integrated $\Delta F/F_o$ traces from single ROIs (gray) and the mean $\Delta F/F_o$ trace (blue) from two washes of 50 μM OXT on glass-immobilized nIROx ($n = 13$). nIROSE nanosensors retains their sensitivity to oxytocin after substrate immobilization. **b,** *In vitro* three intensity heat maps within the same field of view from one wash of PBS and one of 50 μM OXT on glass-immobilized nIROx. Three frames are represented: "Baseline" before PBS addition, "+PBS" after addition of 1X PBS, "+OXT" after the addition of 50 μM OXT. Scale bars represent 10 μm.

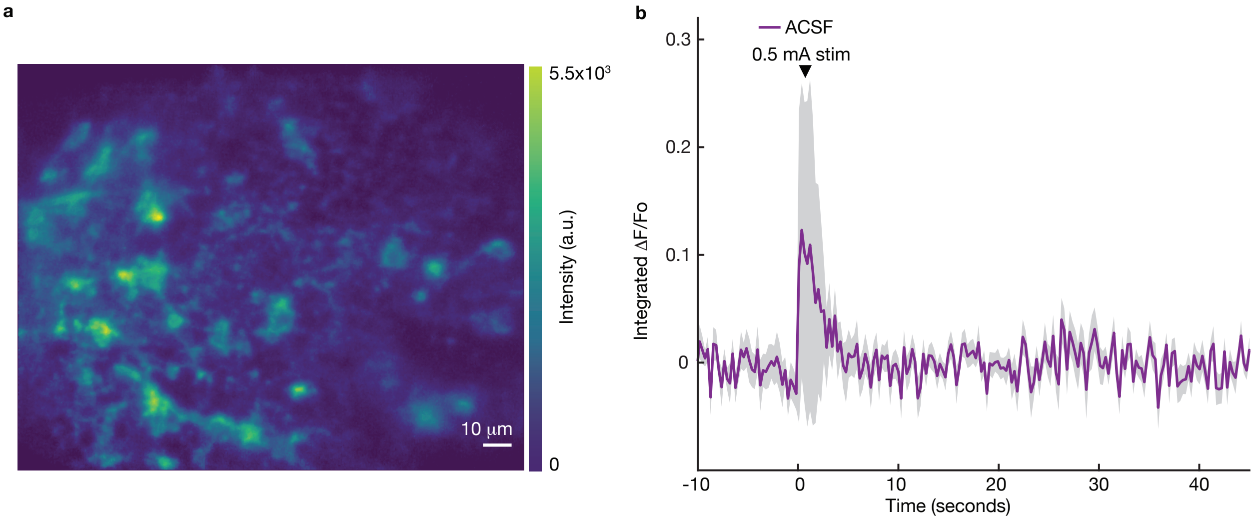

Figure 4.9 | Imaging oxytocin release evoked by electrical stimulation in the paraventricular nucleus (PVN) of acute mouse brain slices. a, *In slice,* field of view of nIROSE-labeled acute brain slices in standard ACSF in the PVN. Scale bar represents 10 μm. **b,** *In slice,* mean time trace (purple) and standard deviation (gray) of integrated nanosensor $\Delta F/F_o$ for a single 0.5 mA electrical pulse stimulation in PVN in standard ACSF.

4.4 Conclusions

While ssDNA-SWCNT nanosensors have been successfully developed and utilized for neurochemical imaging in brains, the traditional heuristic approaches for identifying these constructs have heretofore proved unsuccessful for structurally complex targets such as oxytocin. Our lab recently developed SELEC, an evolution-based platform inspired by SELEX, which enables co-evolution of ssDNA-based molecular recognition moieties with near-infrared fluorescent SWCNT to identify neurochemical nanosensors. We modified and leveraged SELEC to identify sensitive, easily synthesizable ssDNA-SWCNT nanosensors for neuropeptide oxytocin. This work also serves to demonstrate that SELEC is an adaptive strategy for potentially any neuro-target of interest regardless of size or structural complexity. Through SELEC, we identified nIROSE, the 4th most enriched nanosensor candidate from the final round of evolution, which responds optically to oxytocin with nanomolar sensitivity. nIROSE is compatible with oxytocin receptor-targeted pharmacological agents, and preliminary experiments in slice suggest that our nanosensor can reversibly image electrically stimulated oxytocin release in brain tissue. nIROSE demonstrates neuropeptide selectivity that is on par with receptor-based oxytocin imaging probes, but with the real-time temporal resolution requisite to capture endogenous oxytocin release. In comparison to nIROx, the peptide-SWCNT oxytocin nanosensor described in Chapter 3, nIROSE is easier and faster to synthesize and nearly 500% brighter when immobilized in brain tissue. While more work is required to fully characterize nIROSE, as described in Chapter 4.7 Future Directions, our data suggest that nIROx and nIROSE imaging probes are complementary tools. Either oxytocin imaging probe can be selected based on the application and whether maximum selectivity, pharmacological compatibility, or signal-to-noise is required. Together these tools can be leveraged to elucidate oxytocin signaling in the brain and provide insight into the physiological mechanisms that underpin oxytocin-associated neurological disorders.

4.5 Materials and methods

4.5.1 Reagents

Small diameter HiPCo™ single-walled carbon nanotubes (SWCNT) were purchased from NanoIntegris. Oxytocin acetate salt hydrate, [Arg^8]-vasopressin acetate salt, dopamine-HCl, thyrotropin-releasing hormone (TRH), glutamate, γ-aminobutyric acid, and atosiban were purchased from Millipore Sigma. Quinpirole and carbetocin were purchased from Tocris Bioscience. All ssDNA sequences, including the random library used for SELEC, were purchased from Integrated DNA Technologies, Inc.

4.5.2 Systematic evolution of ligands by exponential enrichment on single-walled carbon nanotubes (SELEC)

The SELEC protocol described herein was adapted from Jeong *et al.*[120]. The control sequence library from Jeong *et al.* was preserved. A new control sequence library (evolved in the absence of a target analyte) was thus not developed in this study. The initial ssDNA library used for aptamer evolution consisted of 18 random nucleotides flanked by 1) two 6-mer polycytosines and 2) two 18-mer PCR primer regions: AGCGTCGAATACCACTAC-CCCCCC-N18-CCCCCC-GACCACGAGCTCCATTAG. During the first round of evolution, 100 nmoles of the ssDNA library (200 μL, 0.5 mM) were mixed with acetate buffer pH 5 (200 μL, 20 mM) and SWCNT (10 μg). The mixture was bath sonicated for 5 minutes and subsequently heated at 95°C for 5 minutes to denature the ssDNA. The mixture was then cooled to room temperature for 20 minutes. Oxytocin was added (100 μL, 1 mM) and to bring the final volume to 500 μL. The mixture was incubated at room temperature for 10 minutes and then probe-tip sonicated (Cole-Parmer Ultrasonic Processor, 3-mm tip) for 20 minutes in an ice bath (30% amplitude, 2 W). The resulting suspension was centrifuged for 60 minutes at 16,000*g*, and the supernatant containing ssDNA-SWNCT complexes was collected. The suspension was spin-filtered (Amicon Ultra 100K MWCO 0.5 mL centrifugal filter) six times with nuclease-free water to remove free, unbound ssDNA. The suspension was then mixed with 0.1 % (w/v) SDBS in 1X PBS (200 μL) and heated at 95°C for 5 minutes to detach bound ssDNA from the SWCNT surface. The mixture was centrifuged for 60 minutes at 16,000*g* to pellet SWCNT, and the supernatant containing ssDNA was collected. The mixture was spin-filtered (Amicon Ultra 3K MWCO 0.5 mL) four times with nuclease-free water to remove SDBS. The filtered solution was then stored at -20°C.

The collected ssDNA was amplified by PCR, using a previously described protocol[191], with a FAM-modified forward primer (FAM-AGCGTCGAATACCACTAC) and biotinylated backward primer (biotin- CTAATGGAGCTCGTGGTC). The following PCR mixture was prepared for both preliminary and preparative PCR: Hot Start Taq DNA polymerase (2.75 units , New England Biolabs), 1X Hot Start Taq reaction buffer, forward primer (1 μM), backward primer (1 μM), dNTP (500 μM), ssDNA library template (~10 ng/mL). The total PCR mixture volume for each preliminary PCR reaction tube and preparative PCR well was 100 μL. DNAse-free water was used to dilute the PCR mixture to the desired volume. The following standard cycling conditions were used: initial denaturation for 900 s at 95°C; N cycles of denaturation for 30 s at 95°C and annealing for 30 s at 50°C and extension for 30 s at 72°C; final extension for 180 s at 72°C; hold at 4°C.

The number of PCR cycles was identified through preliminary PCR to maximize dsDNA yield without producing non-specific amplicons. Two PCR reaction tubes, with and without ssDNA library template, was collected at the following cycles: 10, 15, 20, 25 and 30. A 4% agarose gel was prepared by heating 1X TBE buffer (30 mL) and low range ultra agarose (1.2 g, Bio-Rad) in a microwave oven. Electrophoresis was performed on all 10 preliminary PCR samples (100 V, 18 minutes). The gel was stained with SYBR gold, and the DNA bands were observed under UV. The cycle number that yielded the brightest DNA band without nonspecific amplicons was selected for preparative PCR.

For preparative PCR, a total of 10 mL PCR mixture was prepared. Preparative PCR was used to produce a large quantity of DNA for use in the subsequent round of evolution. 100 μL of PCR mixture was added to 95 of 96 reaction wells, and a negative control well was prepared without ssDNA library template.

The preparative PCR product from a single reaction well was collected, purified with a GeneJet PCR purification kit (Thermo Scientific), and stored at -20°C for sequencing preparation. The remaining preparative PCR product was spin-filtered (Amicon Ultra 10K MWCO 15 mL centrifugal filter). ssDNA was extracted from the PCR product using the following protocol: Streptavidin Sepharose beads (2.5 mL, GE Healthcare) was added to a mounted sintered Buchner funnel (<10 μm pore size); beads were washed with PBS (10 mL); PCR product was incubated with beads for 30 minutes, passed through the funnel (3 times); the beads were washed with PBS (10 mL). To elute and collect FAM-labeled ssDNA, NaOH solution (8 mL, 0.2 M) was added slowly.

To desalt the ssDNA, a NAP10 desalting column (GE Healthcare) was washed with deionized water (20 mL). ssDNA solution (1 mL) was added and drained. DNAse-free water was added (1.5 mL) and the eluate was collected. Desalted ssDNA was spin-filtered (Amicon Ultra 3K MWCO 15 mL centrifugal filter) to concentrate and dried using a DNA Speedvac.

For subsequent rounds of SELEC, the dried ssDNA was reconstituted in acetate buffer pH 5, and the concentration was determined by measuring the UV/Vis absorbance at 260 nm.

4.5.3 High-throughput sequencing and analysis

To prepare sequencing libraries from ssDNA, two sequencing PCR steps were used[192] to add Illumina TruSeq universal adapter sequences and sequencing indices. Libraries from SELEC rounds 3 to 6 were sequenced with an Illumina HiSeq 4000 at the Genomic Sequencing Laboratory at the University of California, Berkeley. From the ~20 million raw sequences generated from each round, we removed sequences that did not contain the correct fixed regions (flanking 18-mer PCR primers and 6-mer polycytosine). The FASTAptamer toolkit was used to filter and count sequence frequencies[193].

4.5.4 Nanosensor synthesis

To prepare aptamer-SWCNT, SWCNT slurry (900 μL, 0.22 mg/mL in 1X PBS) and aptamer (100 μL, 1 mM in DNAse-free water) were mixed. The mixture was vortexed for 3 seconds, bath sonicated for 10 minutes, and probe-tip sonicated (Cole-Parmer Ultrasonic Processor, 3-mm tip) for 10 minutes (50% amplitude, 5 W) in an ice bath. The resulting suspensions were centrifuged at 16,000*g* for 60 minutes to pellet unsuspending SWCNT. The supernatant (900 μL) was centrifuged again at 16,000*g* for 30 minutes, and the supernatant (850 μL) was used transferred to a new tube. The concentration of nanosensors was calculated by measuring absorbance at 632 nm (NanoDrop One, Thermo Scientific) with an extinction coefficient of $\varepsilon = 0.036\ (\mathrm{mg/L})^{-1}\ \mathrm{cm}^{-1}$[142]. Nanosensors were then diluted to 5 mg/L SWCNT in 1X PBS and stored at 4°C for further use. Nanosensors were not used in experiments for at least 24 hours after dilution. Nanosensor suspensions are were stable for at least 6 months after synthesis if stored at 4°C. The SWCNT slurry was prepared by mixing hydrated SWCNT (500 mg, 1 g SWCNT/50 mL water) with 1X PBS (50 mL). The mixture was bath-sonicated for 60 minutes and then probe-tip sonicated (Cole-Parmer Ultrasonic Processor, 6-mm tip) for 20 minutes (25% amplitude) in an ice bath. The SWCNT slurry was stored at room temperature. Prior to use in nanosensor synthesis, SWCNT slurry was vortexed for 3 seconds and bath sonicated for 10 minutes prior to use. Aptamers were heated at 55°C for 5 minutes and cooled to room temperature before use.

4.5.5 Optical characterization and analyte screening

Near-infrared fluorescence spectra were collected using a custom built spectrometer and microscope as described previously[165]. Measurements were obtained with a 20X objective on an inverted Zeiss microscope (Axio Observer.D1) coupled to a spectrometer (SCT 320, Princeton Instruments) and liquid nitrogen cooled InGaAs linear array detector (PyLoN-IR, Princeton Instruments). Nanosensor suspensions were excited with a 721 nm laser (OptoEngine LLC) inside a polypropylene 384 well-plate (Greiner Bio-One microplate).

For analyte screening, the baseline near-infrared fluorescence spectrum of each nanosensor-containing well was collected. Either PBS or analyte diluted in PBS was added, and post-analyte fluorescence spectra were collected at 5-minute time points until the maximum oxytocin fluorescence response was achieved (~20 minutes). Responses were calculated and reported as $\Delta F/F_o = (F - F_o)/F_o$, where F_o is the peak fluorescence after PBS incubation, and F is the peak fluorescence after analyte incubation. The peak fluorescence corresponds to the (8,6) SWCNT chirality, which has a maximum near-infrared fluorescence at ~1195 nm.

For selectivity screening, all analytes were added at a final concentration of 50 μM. During oxytocin screening of various nanosensor constructs, oxytocin was added at a final concentration of 50 μM. For dose response experiments, final oxytocin concentration ranged from 1 μM to 100 μM.

For *in vitro* experiments, nanosensor suspensions were prepared at 5 mg/L in PBS. All measurements were obtained in triplicate, and reported results include the means and standard deviations of these measurements.

For immobilization experiments on glass, nanosensors were immobilized on MatTek glass-bottom microwell dishes (35 mm petri dish with 10 mm microwell). To immobilize nanosensors, the dish was washed twice with PBS (150 μL). Nanosensors (100 μL, 2.5 mg/L in PBS) were then added, incubated for 10 minutes, and removed. The dish was washed twice again with PBS (150 μL). Surface-immobilized nanosensors were imaged on an epifluorescence microscope (100x oil immersion objective) and a Ninox VIS-SWIR 640 camera (Raptor) and excited with a 721 nm laser. For each imaging experiment, the z-plane was refocused and 120 μL PBS was added prior to recording. Image stacks were collected with a 950 ms exposure time and 1 Hz frame rate for 5 minutes. PBS was added at frame 60 and oxytocin was added a final concentration of 50 μM at frame 120. Image stacks were processed in ImageJ by applying a median filter (0.5-pixel radius) and rolling ball background subtraction (300-pixel radius). ROIs were manually identified and characterized using the ROI analyzer tool. Responses were calculated and reported as $\Delta F/F_o = (F- F_o)/ F_o$, where F_o is the mean integrated fluorescence after PBS incubation, and F is the peak fluorescence at each timepoint after oxytocin addition. The means and standard deviation of all 13 ROI $\Delta F/F_o$ values are reported.

4.5.6 Imaging electrically stimulated oxytocin release in acute brain slices

To electrically stimulate oxytocin release, a bipolar stimulation electrode (MicroProbes for Life Science Stereotrodes Platinum/Iridium Standard Tip) was positioned within the putative paraventricular nucleus using a 4x objective (Olympus XLFluor 4x/340). The stimulation electrode was introduced into the top of the brain slice and an imaging field of view nominally 50 μm from the stimulation electrode was chosen using a 60x objective. A total of 600 frames were acquired at nominally 4 frames per second, where stimulations were applied after 200 frames of baseline. Stimulation pulses were applied for 1 millisecond at 0.5 mA.

4.5.7 Image processing and data analysis of nanosensor fluorescence response in acute brain slices

Imaging movie files were processed using a custom MATLAB application (https://github.com/jtdbod/Nanosensor-Brain-Imaging). ROIs were identified by first applying a 25x25 pixel grid mask to the image stack. The median pixel intensity and a median filter convolution within each ROI was then calculated. Post-stimulation and exogenous oxytocin fluorescence responses were calculated as $\Delta F/F_o = (F- F_o)/ F_o$, where F_o is the average intensity for the first 5% of frames and F is the dynamic fluorescence intensity. Significant $\Delta F/F_o$ traces were identified by thresholding with Otsu's methods to differentiate ROIs from the background. For stimulation experiments, decay time constants (τ) were computed for significant ROIs by fitting each $\Delta F/F_o$ trace to a first-order decay process. Latency to peak was calculated as $t_{\text{peak}} - t_{\text{stim}}$, where t_{peak} is the time at which maximum fluorescence occurs, and t_{stim} is time of stimulation. The $\Delta F/F_o$ traces where latency to peak is greater than 5 seconds were assumed to result from stimulation artifacts and were thus removed from analysis. The maximum $\Delta F/F_o$ of each significant ROI trace was identified, and the $\Delta F/F_o$ of a stimulation or exogenous oxytocin wash was reported as the median of these values.

4.6 Supporting information

4.6.1 Supporting equations

nIROSE (E6#4-SWCNT) nanosensor kinetic parameters were quantified by fitting dose response data to the cooperative binding model below:

$$\frac{F-F_o}{F_o}=a\,\frac{(K_d[S])^n}{(K_d[S])^n+1}+b$$

Kinetic parameters were calculated as n=1.63±0.976, b=0.087±0.092, a=1.77±0.483, and K_d=4.93±3.19 µM and are reported with 95% confidence intervals using the t-distribution.

4.6.2 Supporting tables

Table 4.1 | ssDNA sequences from SELEC round 3.

Rank	**ER3 (Experimental SELEC Round 3)**		**CR3 (Control SELEC Round 3)**	
	Sequence	**# of Reads**	**Sequence**	**# of Reads**
1	GGGGTTACTATATGACAT	20	ACAGACCGACGTGTGCTG	5
2	CCCCCCCCCCCCCCCCCC	12	TGGGAGCCATCTTGTGCG	5
3	AGGGGAGCGTGCGGAGGC	12	GTTCAGCCTTTTCGTTCG	5
4	GACTTGGGCTCATGCTGT	10	GGAATCTCCGGCGTCTAT	5
5	TAGACAGGGCTGACTGTG	10	TAGCACAGGTCGTCTATT	5
6	GGCGGACAGACTCTAATG	10	GCCAATATAGCCCTTCCG	5
7	GGGGGCACAGGGCGATAC	9	AATCACTGCAATGGTCGT	5
8	TGACGTCCTGACATGTTC	9	AACACATTGACGTGCACT	5
9	GTGTAGTACATGGCGGCG	9	GGGCTGTGCCGTCATGCG	5
10	CAGGAATCCGACATGGCT	9	GATGGGGAATCATGCGTG	5
11	CAAGCTGGAGTGGCAAGG	9	AATGATACGGTGACGGTG	4

12	AACGATACAGTGGGGTGC	9	GGAGGTAAAAGGACATGT	4
13	ACGTGCTCTATGTTTCTA	9	AGCTGCAGCCGCACTGTG	4
14	TGGTGCGCCAGGGCCGTG	9	GGCAGCGGGATGACACGG	4
15	GGGGCAAGGAGACAGCAT	8	GCTGGACCTCGTACATGT	4
16	GATCGGGCGGTGGGATCG	8	GGGGCATGATACTTGGTC	4
17	TGTGCGGCCCTGGTCGTC	8	TAGGGCTTAGATGACGGT	4
18	TGGCGTGCTTGTTTGGAG	8	GACCCGTACTCTTCCATA	4
19	GGAGCAGTGGCGGAGAGA	8	GGAGTTTCCACGTGCGAT	4
20	ATTAGACGTTTAAGAGTG	8	GTAGTGGGCATCACTTCG	4
21	AGGGATGCGCCCCCGTGT	8	AAGCGGAAGGACATTGTG	4
22	AGGGGATACGCGTCGTCG	8	TTGGACTCTCTAGTGTGC	4
23	TCGTGAGGTTTCATCGAT	8	CTGGAACTCGCTCTCGTT	4
24	GACGTGGGGAGGCGGTCC	8	AAGCGGGCTGGGAGTGCG	4
25	GGGAGTAGTAGTCATCAT	8	GATCACGTAATGCGCGCT	4
26	ATCAAGGCTATATCGTGC	8	ACATGACGTATGCTCCTC	4
27	ATAGGTGTGTGCATTCGG	8	GACAAGGGTCACGGATGG	4
28	TTGACTGCTCGCGATATA	8	CATAGGGACATGACGGCG	4
29	AGGCAGGAAACGACGAGG	7	GGCGGCCGCTATTGCTTT	4
30	ATTGGACGGACTACGTAT	7	ATACGCGTGCTACATGTG	4
31	GCGTGGCGTGATATATCG	7	AGTGGGTTATACGTGTTC	4
32	GGGTTAGAGTTGCGAAAT	7	GATGGCGTCAGCTGGCGT	4
33	AACGGGCTAACAGATAGG	7	TCAGCGGAGGATGTGTTA	4

34	CAAGCAGGACGGGACTAG	7	GGAGTGCGTGCCGTGTAG	4
35	GTGGTGGTACCGGCCCGA	7	GCTGCTGCTCGATGTGCG	4
36	GTACATGGGGAGAACAGT	7	AGGCATCTTCGTGCGGTG	4
37	ACGTTGCGGGTATCTGAT	7	AGACGAGAGCTCCATCCG	4
38	GGGCGGGCACCCACGACA	7	ATGCCAACGTGGACTGTG	4
39	TGGGTAGGTACGGTCATG	7	AGCGGTGATCAACGTGTG	4
40	AGGGCTAAGATCGAGGTT	7	ACTGACCAGCGTTGTGTG	4
41	TGTGCCGATCCTTACACA	7	GTTGGGTATCAGTATACG	4
42	GACAGTGGCTAGTGCGTG	7	GACTACGCGGATGACTGG	4
43	GCCGTGTCCGCTGATATA	7	ACTGCCCACTCTGGTGCT	4
44	GTTCTCATGGGACTAGGT	7	TCACCAGTTCATCGTGTC	4
45	TGGTTAGATGAGGCGTGG	7	AGCCATGGTACCGTGTGG	4
46	AACAGGGCGTCGGCCGTG	7	GGGGCGACACAGCATGCA	4
47	AGCTATGCCGCCGCCGTT	7	AACCAGGAGTCATCCGTT	4
48	GGAGGCGAATTTGGTGGA	7	TGCACCGGACTTCCGACT	4
49	TCGATGTCAGCCGCGCGT	7	AATGATGCAGATGACGTG	4
50	AGCAGAGGAGGCGGCGGA	7	AGGGTGTCCAACTCGCCT	4

Table 4.2 | ssDNA sequences from SELEC round 4.

Rank	**ER4 (Experimental SELEC Round 4)**		**CR4 (Control SELEC Round 4)**	
	Sequence	**# of Reads**	**Sequence**	**# of Reads**
1	ATCATCATCATCATCATC	14	ACACAGCATCATTCCGCT	7
2	GTGGGTGCATTTGCTGTA	12	GCACCAACCAGCCGTCTG	6
3	GACGGCATTCAGGCACGT	12	TCACCACATTCGACGGCG	5

4	TGTAGTGCTCGGCTGCCG	10	ACCACAAGTGACTGTCCT	5
5	AGGCTGCGTAAGTCTGCT	10	GCCGACATGACTCCTCCT	5
6	ATGTAGTGTTCTAGTCGT	9	ACACACCAATGACCTGTG	5
7	GGGGCGAGCCATATCGTG	9	TACCCACACCACACACTG	5
8	TCGGGCAGGTTTCACGGT	9	ACTGCACATCGACGCGCG	5
9	ATGTGGGATAGGGACAGG	9	ATTGCCGCCATCCTCATG	5
10	GACGATGGGTGTACGGTA	9	AGGCCACCGTCGCACGTG	5
11	GGGAATAGTGTCGTGCGC	8	GCACAGCACGCTCCCGAT	5
12	CGGGCAAGGATTACAGCG	8	ACAGTACCAACACGTGCG	5
13	CAGCATGGAGGGTTGTAC	8	GCACACACCAGCCGTCTG	5
14	GTTACGAGGGAGGAGGCG	8	AACACCACACACGGCGCT	5
15	TGCACCAAGCATCAGCGG	8	GCACACAGCGAGATGCCT	5
16	GGCGGGGTAACCACTGCA	8	ATCCACCACCACCGTGCT	4
17	ATACTCGCCCATACGCCG	8	TTAATGACTGACGTTGTG	4
18	CATTCGGTGCGGCCCGGG	8	ATCCGACAGTCTCCGGTG	4
19	TAAGGCGAAGTACCAGTG	8	AACAGCACCATCACGTGT	4
20	CCCCCCCCCCCCCCCCCC	8	AGCACCATGCATCCTGTG	4
21	TGGGTATCACGGGAAAGT	8	ACACCCACTCACTGTGCT	4
22	AGTTGGTTCCGGCTGGAG	8	GCGGCATACCAGTGTGCT	4
23	GATACTGCCGTTGACGGT	8	GCACACCCTAACTCCGCT	4
24	CTATGGAGCAACAGTGAT	8	GATCCGGTCGTGCATCCG	4
25	TAGCGTAAGGTCCATGTT	8	ACAGTACGACCTGTGCCT	4

26	GCAGGGCAAGTGAAGGTG	8	TCGCGTGACTGGCCTGTA	4
27	AATCCACCACCTGCTGCT	8	GGCACACCGATACGCCAA	4
28	GCATCAGCTGGCTTAGCG	8	AGGCACAGACCGCATGCT	4
29	AATGGAAGGAGTGAGATG	8	GCACACTCCTGCCTTCCT	4
30	GGCTAGTAAGGTGTCCTG	8	TACACGACATGCCGCTCG	4
31	ATGAGGCCTTGAGGAGTG	8	ACCACGCATCATCCGTGT	4
32	ATAGGGCGCACCACTCCA	8	TGGACTCAGATCCCGTGT	4
33	GCGGTAGTGCATGCTCCT	8	ACCATGTCACACACGTGT	4
34	GACGGGGCGACGCGGTAA	8	ACACGATACGAGCTGCCT	4
35	ATGGCCGGACTCTTGGCG	8	GAGGAGTCGACGCACGTG	4
36	AACCGGTGTGCTGCGGAT	7	GGACGGTACTCTCCAGTG	4
37	TACGGAGCACACGGCGAA	7	ACACCGTCATACATCGTG	4
38	GGCGACAGTGCCTAATGT	7	AGCCGCTCCATCCTTCCT	4
39	GGTGATGTTCCCGATCTG	7	ACGGCACACAGGACGCTG	4
40	AGGATCCGTCGGGAGCCG	7	ACGAACGGATAGTGTGTG	4
41	GACTGTGGGTGACGCTGG	7	AACACTCGATGTCGCTCT	4
42	AGAGGTGGAAACGTGCTG	7	AAGCTGCCTAAGCGACTG	4
43	TCCCCGAGGGCCGACTTA	7	GGGAGGTAGCAATATCGT	4
44	ACGGGTGAGGTCGGCTGC	7	AACCGATCCTTGCCGCTA	4
45	GCCGGGTTGCCACTAACG	7	ATCGGGCGAAGGACAGAT	4
46	GGATGCTGGGATGAGGTG	7	GCCGTGATTGTTCCGATC	4
47	GGTGCTGGTTCGGTGAAT	7	GCACACCAATACTCGATG	4

48	GGGCGGACACTTTGCGAC	7	ACCACCACTGTCCATGTG	4
49	GGCGATACGGTGAGAGGT	7	AGCACACATCGACGTCCG	4
50	GGTGAACGAGACAAGCTC	7	AACAAACCACGACGCGTA	4

Table 4.3 | ssDNA sequences from SELEC round 5.

Rank	**ER5 (Experimental SELEC Round 5)**		**CR5 (Control SELEC Round 5)**	
	Sequence	**# of Reads**	**Sequence**	**# of Reads**
1	AAGATGTATCGTGTGCTG	9	AACACCACACACGGCGCT	264
2	CCCCCCCCCCCCCCCCCC	9	AGCACACTCCACTCCGCT	232
3	GGGTAAGGGCACAACAGT	9	GCACACACCAGCCGTCTG	216
4	AATACAGCGGTGTTTCTA	9	AACCACACACCGTCCGCT	209
5	TATTACACTAGTGGATGG	8	ACCACACCATCGACGCGT	159
6	AGTTTGGTACTACTTCCG	8	AGCCACACGACGCGCTCT	157
7	TTGAGCGTAACGACAGTG	8	ACGGCACACACCATCGCT	145
8	AGGGTATAACGTCCTTTG	8	ACGACACTGCACGACGCG	139
9	ATAAACAGTCTAGCTGTG	8	ACGGCAACTCCCATTCCG	120
10	AGGAACTACGATCGTGAA	8	ACGACACCACACTGCTCT	119
11	TAACGGGTTATCCATAAT	8	AACCACCTCCACTCCGCT	115
12	TGGGTCACATATAGAGCT	8	ACACAGCATCATTCCGCT	115
13	GGCCAATGGATTCGTGTA	8	ACACCTCACACATCGCCT	114
14	TTATGAGAAGTACGAGCT	8	AACACGGCACACTCACAT	113
15	AAGCAGAAAGTGTTGGCA	7	ACCACTAGCCATTCCGCT	113
16	ATTAGACCTGTCGCCCGT	7	ACACACACACTCTCCGCT	111
17	ACTTCGCGGTTGATAGGC	7	AACACCTCACACTCCGCT	102

18	GGGAACAAGTTGATCGGT	7	ACACAGCCATGCCGCTCG	98
19	ATACTAATGGCGAGACGA	7	AGCACACATCGACGTCCG	98
20	AGATGACTTAGTGACATT	7	GCAGCCACACGTCGCTCG	97
21	ACAAGTATACCGTTAGCT	7	AACACCACCATCACGCCG	97
22	ATCATCATCATCATCATC	7	TCACACCACCACCGTGCG	92
23	AAGCAGTTATACTGGGTA	7	AGCACAACACGGCATCCT	88
24	ACGAGGGCGTAAGTGGCA	7	ACACACCGACTGCCTGTG	87
25	TGAAGAGGTGAACTGTAA	7	ACGACATCCTGCACTCCG	85
26	TAGACGGTAAACTGTGAT	7	ACACCACAACACGCTGTG	85
27	AGGTATCCCCATAGTCCT	7	ACCGCACACCACTCCGAT	85
28	CTTACGGTCATACTGTGT	7	ACACCACACCGACGACTG	84
29	GAATGGCGTTGGTGGTAA	7	AACACACACCGCGCCGAT	83
30	TAGCACCATGGGGTTAAT	7	ACACGAACGCCACTTCCG	82
31	TGGAGAGAGACGGTGTAC	6	ACCACACGACAGACTGCG	81
32	CAAGGGATGGAATTATAG	6	ACACCACACCACTCCGCT	81
33	CAGGAGGAAGGGATACGA	6	ACACCACCACAGACGCGT	80
34	ATGATATATGGCAGTGCT	6	ACACGTCCAGACCATGCG	80
35	GTGTGCAAGAAGACATGT	6	GGCACACGAACGACGCGG	80
36	AATAGGCAACCTACCGAT	6	ACCGCACCATACTCCGCT	80
37	GGAGGTGATTTTGCTTGG	6	AGCACCGTCACACCTGCG	79
38	GACATTGTCTCTTCCGTA	6	ACACAGCAGACGGCGCCA	79
39	AGGGTCATGAGTTCTGGT	6	ACACACAGTCGACGCGTA	79

40	AGGTAGCGACTTTACAAA	6	ATGCCACTACACTCCGCT	78
41	AGATGGTGATACATGGTA	6	ACTGCACATCGACGCGCG	78
42	AGAGAGATGGATGATGGA	6	ACCACACACCACCGTGCT	77
43	GACGATCGTGATTCTGAG	6	AGCACATACCGCTCTCCG	77
44	AAAGGGTAAGCCGTTATT	6	ACGCAACACTGCCTTCCG	77
45	CTTCAACCGCTAGTACGA	6	AACACACCATGCCGCTCT	76
46	AAGTCCGTGTACATTGCG	6	AATGCCACACACGACGCG	75
47	AGGATAACTGCTCTTCAA	6	GCACCAACCAGCCGTCTG	73
48	ATCGGGAAAACTGCCTGT	6	AGCAGCAGCCAGCACACA	73
49	TGGTAAAGACTGTGCACT	6	ACCATGACACCGTGCGCT	73
50	AGGTCTATATGGTGGCGT	6	AACACCACACGACGTGCG	72

Table 4.4 | ssDNA sequences from SELEC round 6.

Rank	**ER6 (Experimental SELEC Round 6)**		**CR6 (Control SELEC Round 6)**	
	Sequence	**# of Reads**	**Sequence**	**# of Reads**
1	CCCCCCCCCCCCCCCCCC	25	ACCGCATCGACATGTGCT	572
2	AGGGCCTAGGGATGACGT	12	ACCGCACGAGCCAGTGTG	480
3	GAGCAACGGGTCAGCATT	11	TCACCACATTCCGCTGTG	381
4	ACGGGACCGCAGATCGAG	11	ACCGAGAGCAGACGATGT	336
5	AAGTAGGGACAGAATACG	9	AACACCACACACGGCGCT	335
6	GGGATTCGGTCATGTCCT	9	GCAGCGTGACTTGACGTG	293
7	TGCATCGCAACAGCAGTT	9	AACACGGCCCTCATGTCG	289
8	GGGGCATTCACTGAGCTG	9	AGCCGTATGCACACCTCA	284
9	GTAGAATGGGCATCGTCG	9	ACACACCGTTCATCCGCG	283

10	AGCGGCGGCGACGGCGAA	9	GCTGATCGACGACACGTG	267
11	ACACTGCGGGTAGCTTGC	9	AACACGACATGCAGTGTG	257
12	TTAGACTGCACTTCACGA	9	GGCCACATACATACGGTG	254
13	GTAGGGTCATGACCAAGG	8	TGCAGCCCACGACATGCG	243
14	TACGTAGCTCAAGGGTAC	8	ATGCGGAGTCCGACTGCG	238
15	TGGGCAGTGCAACTGTTA	8	GCGGCATACCAGTGTGCT	234
16	GAGGCAGTGACAGTGGAG	8	AGCGACCAATGACCGGTG	234
17	GCGCTGCCAGCATGCGGG	8	ACGGCAAGGTGAACGGTG	232
18	GGTTGGGAGCGGCACAGT	8	AGGATGGCTTACGTGCTG	232
19	TGCATACGTGACGGCGCT	8	GACCTCATCCGTGCACGT	227
20	TGGGATCCATCTCAGGAA	8	GTGCCGAATGCAGTGTGC	227
21	CTATCGCGCGTGGACCTA	8	AGGCAGACCGCACCGTGT	226
22	GCGACGATCATGACTGTT	8	GGCCAAGACCAGACGGCG	223
23	ACGGGCAACGAATTAGCA	8	ACTGCTCCTCATCCTGTG	222
24	GTGGGATCGACACTGCCT	8	AGGACACAGTGACATGCT	219
25	TGCGGGCAGACGCGGCAA	8	GCCAAGCCGCGACGTGTA	217
26	ATGGCAGGCCCACAGGTG	7	ATGCAGACAGCCAGTGCG	215
27	AAGCAGGAGACTTGCGTG	7	GGCCAAGACAACGTGTCG	214
28	GCAGTGACACAGACAGCT	7	ACAGATGCGCCATCCGAT	213
29	ATATCGGACCGTGGCGCT	7	GAGCAGCACCAGACATGT	209
30	ATGCAATGGTTCAGCGAT	7	AACGACCGGATGTGTGCT	209
31	AGGCAAAGAGTGTCGTCT	7	TCGACACACATCCGCGTG	209

32	GATGGTAACGGTACATGG	7	ACGTGCGCCACTCCTCCT	208
33	GGTAGGCGCGATGAGGCT	7	AGCCATGTGCCTCCATCG	207
34	ACGGACTGCTGTCAGTGG	7	TCCACACCATTGCGCTCT	207
35	TCATCCGCGTGACGTGCG	7	GCACGATGGTAGACGTGT	207
36	AGCAGAAACGGAGGCAGT	7	AGCCGACTCCACACGTGG	204
37	GACTCAATCAGAAGACTA	7	ATGCACCAACCACGTGCG	201
38	CGCGGGGCACAGGCGCGA	7	GACGGCATACGTCCCGCT	200
39	GTATTAGTGGCGTCTTGT	7	AAGCCGCCACACGCATTG	197
40	ACGGTGGCAGGTAGGTAT	7	ATCCTCACCCAATGTGCG	197
41	ACGGGTTAGGAGGATTAT	7	ACGGACACGTGACTGCAG	195
42	ATCGACGTGTGAGGACTA	7	TGTACATGACGCCGTGCA	193
43	AAAGCGAGTCGGCAAGAG	7	AATGGCCAACTGTGCGCT	193
44	GTGTGCGAAGAGTCTTGT	7	GCGTACGGGAAGTGCTGT	192
45	AGACACATGCATCGACTT	7	AACGCGTCATACCCTGTG	191
46	TACGGTGTGCTCCAGCTG	7	AGCACACATCGACGTCCG	190
47	TGACCGGGAGAGGGCGTT	7	ACGCATCATCGACCTGTG	190
48	ACACAGCACACATCCCCT	7	AGGGACACACACACCGAT	189
49	AACAGGCGGTACTGGAGC	7	ACTGCCCTCACCATGTCG	187
50	ACGGGAATACAGCAGATA	7	GCACAGACGACGTGTACT	187

Table 4.5 | Top 25 3-mer ssDNA motifs in rounds 3-6 of experimental SELEC libraries.

Rank	ER3 Motif	ER3 Reads	ER4 Motif	ER4 Reads	ER5 Motif	ER5 Reads	ER6 Motif	ER6 Reads
1	GTG	1439	GTG	1423	GTG	1121	GTG	1217
2	GGC	1280	GGA	1314	GTA	1063	ACG	1159
3	GGG	1259	CGG	1266	ATG	1024	GCA	1153

4	CGG	1230	GGG	1247	TGG	970	GGC	1153
5	GCG	1181	AGG	1185	GGT	962	AGG	1125
6	GGT	1159	GGC	1158	TGT	936	GGA	1084
7	TGG	1143	GGT	1153	AGT	907	GAC	1064
8	AGG	1136	TGG	1144	TAT	904	CGG	1043
9	GGA	1093	GCG	1142	GGA	858	GGG	991
10	ACG	1000	ACG	1123	ATA	846	CAG	978
11	GAG	984	GAG	1028	AGG	838	TGG	968
12	GCA	937	GCA	1008	TAG	830	GGT	962
13	GAC	896	TGC	985	GGG	762	GCG	911
14	ATG	875	ATG	966	GAT	760	AGC	840
15	CGT	863	CGT	966	GTT	742	ATG	828
16	CAG	857	GAC	936	GAG	732	GAG	805
17	TGC	854	GTA	878	TAC	726	GTA	778
18	GCT	841	AGT	859	CAT	725	AAG	762
19	AGC	797	GCT	831	ACG	722	TGT	757
20	TGT	788	CAG	810	ACA	703	CGT	749
21	CGA	758	TGT	787	CGT	688	GAT	724
22	CTG	729	CTG	763	AAG	684	GCT	718
23	GAT	721	AAG	753	AAT	683	AGA	705
24	AGT	720	AGC	733	TAA	674	CGA	695
25	TCG	709	TAG	717	ATT	665	CAT	684

Table 4.6| Top 25 3-mer ssDNA motifs in rounds 3-6 of control SELEC libraries.

Rank	CR3 Motif	CR3 Reads	CR4 Motif	CR4 Reads	CR5 Motif	CR5 Reads	CR6 Motif	CR6 Reads
1	GTG	975	GTG	826	CAC	22691	GTG	40745
2	TGG	671	ACG	726	ACA	20172	ACG	38591
3	TGT	671	CAC	685	CCA	16624	GAC	36418
4	GGT	656	CGT	653	ACC	16318	CAC	35346
5	GGA	601	GAC	652	CGC	13714	CGT	31042
6	ATG	582	ACA	614	CCG	13418	ACA	30430
7	CGT	566	GCA	611	ACG	13058	CCG	30150
8	ACG	553	ACC	597	GCA	11533	ACC	29376
9	CGG	518	TGC	587	CGA	8850	GCA	28770
10	GAC	516	CCA	555	CAT	8739	TGC	27752
11	GCG	509	CCG	543	GAC	8455	CCA	26797
12	TGC	509	TGT	539	TCC	8354	CGC	26010
13	GGC	502	CGA	518	ACT	7765	CGA	25779
14	AGG	501	CAT	498	AGC	7679	TGT	24469
15	GGG	471	CGC	498	AAC	7661	CAT	24237

16	GAT	450	TCC	484	ATC	7496	CAG	23758
17	GCT	450	CTG	468	GCT	7422	ATG	22980
18	GTA	441	CAG	462	GCC	7352	GCG	22393
19	AGT	438	GCT	439	CGT	7288	TCC	21720
20	CTG	432	ATC	419	CTC	7054	GCT	21555
21	TCG	423	CCT	411	GCG	6361	GCC	19349
22	TAG	417	GCG	407	CAG	6342	ATC	19290
23	CAT	414	ATG	401	CAA	5493	ACT	18612
24	CAG	405	ACT	400	TCG	5092	CTG	18500
25	ACA	382	AGC	396	CTG	4948	AGC	17524

Table 4.7 | Enrichment of 3-mer ssDNA motifs between rounds 3-6 of experimental SELEC libraries.

Rank	ER3-ER4 Enriched	ER3-ER4 % Enrichment	ER5-ER5 Enriched	ER4-ER5 % Enrichment	ER5-ER6 Enriched	ER5-ER6 % Enrichment
1	AAT	55.2	TAT	162.0	CGC	238.0
2	TAA	52.4	TTT	126.5	GCG	134.8
3	AAA	46.1	TTA	119.2	GGC	129.7
4	ACC	41.2	ATA	107.9	GCC	127.9
5	AAC	39.9	ATT	90.0	CGG	121.9
6	GAA	39.6	CTA	48.9	CCC	98.3
7	ATC	32.2	AAT	47.2	GCA	90.3
8	GTA	26.1	AAA	41.4	CCG	72.9
9	TCT	24.5	CTT	40.6	CGA	71.6
10	TAG	21.5	TAC	34.9	CAG	67.5
11	GTT	20.5	TAA	34.8	GAC	63.2
12	GGA	20.2	TTC	34.6	CAC	61.9
13	AGT	19.3	GTA	21.1	ACG	60.5
14	CGC	19.0	TGT	18.9	AGC	46.6
15	CAA	18.2	TTG	18.9	ACC	41.0
16	TTC	17.2	ACT	17.8	CCT	36.4
17	TCC	15.6	ATC	16.7	AGG	34.2
18	TGC	15.3	TAG	15.8	TCG	34.0
19	TCA	12.4	GTT	15.6	CCA	32.2
20	ACG	12.3	TCT	15.5	GAA	31.5
21	ATA	12.1	ACA	13.0	GGG	30.1
22	CGT	11.9	CAT	12.6	GGA	26.3
23	CTC	11.5	GAT	9.2	CTG	25.6
24	AAG	11.1	TCA	8.1	GTC	15.1
25	ATG	10.4	ATG	6.0	AGA	13.9

Table 4.8 | Enrichment of 3-mer ssDNA motifs between rounds 3-6 of control SELEC libraries.

Rank	CR3-CR4 Enriched	CR3-CR4 % Enrichment	CR5-CR5 Enriched	CR4-CR5 % Enrichment	CR5-CR6 Enriched	CR5-CR6 % Enrichment
1	CAC	186.6108787	CAC	3212.555	TGG	8494.828
2	ACC	139.7590361	ACA	3185.342	GGT	4768.148
3	CCA	120.2380952	CCA	2895.315	GTT	2308.333
4	AAC	78.40375587	CGC	2653.815	GGA	2248.705
5	CGC	75.35211268	ACC	2633.333	TTA	2155.556
6	TCC	71.02473498	CCG	2371.087	TAT	2002.273
7	GCA	64.69002695	CTC	2050.61	GGG	1787.805
8	CCT	63.74501992	AAC	1916.053	TTG	1516.803
9	ACA	60.73298429	CAA	1912.088	AGT	1407.235
10	CCC	56.71641791	ACT	1841.25	AGG	1400.5
11	CGA	54.16666667	AGC	1839.141	TAA	1315.484
12	CCG	53.82436261	GCC	1824.607	TAG	1287.845
13	ACT	35.13513514	GCA	1787.561	TGA	1183.443
14	CTC	33.33333333	ACG	1698.623	GTA	1166.494
15	ACG	31.28390597	ATC	1689.021	GAG	1029.672
16	ATC	26.58610272	CAT	1654.819	TGT	1009.705
17	GAC	26.35658915	TCC	1626.033	GTG	849.7669
18	GCC	20.50473186	CGA	1608.494	AAG	806.4298
19	CAT	20.28985507	TCA	1604	ATA	803.9039
20	CAA	19.73684211	GCT	1590.661	ATG	725.7276
21	AGC	19.27710843	GCG	1462.899	AAT	665.0685
22	CGT	15.37102473	CCC	1348.095	AGA	573.2287
23	TGC	15.32416503	TCT	1284	GAT	565.6148
24	CAG	14.07407407	CAG	1272.727	GAA	542.9782
25	CTG	8.333333333	TCG	1243.536	TGC	475.2902

Table 4.9 | Frequency of the ACG motif as a function of position along the 18-mer in experimental and control ssDNA libraries from SELEC rounds 3-6.

ACG Motif								
Position	ER3	ER4	ER5	ER6	CR3	CR4	CR5	CR6
1	0.90	0.76	1.02	1.43	1.44	2.24	2.34	1.36
2	0.55	0.83	0.76	0.38	0.93	1.48	0.10	0.96
3	0.50	0.53	0.42	0.74	0.48	0.97	0.64	0.69
4	0.45	0.35	0.42	0.68	0.37	0.60	0.48	0.58
5	0.51	0.77	0.13	0.80	0.73	0.72	0.24	0.40
6	0.42	0.51	0.24	0.57	0.63	0.76	1.01	0.58

7	0.45	0.22	0.23	0.40	0.57	0.80	0.49	0.55
8	0.35	0.43	0.24	0.71	0.53	0.70	0.38	0.46
9	0.62	0.47	0.43	0.42	0.64	0.94	0.70	0.67
10	0.70	0.56	0.46	0.76	0.67	1.11	0.80	0.56
11	0.34	0.65	0.54	1.11	0.65	1.11	1.15	0.91
12	0.67	0.66	0.29	0.57	0.85	1.93	1.29	1.53
13	0.67	0.75	0.50	0.46	0.70	1.94	1.33	1.10
14	0.64	0.71	0.45	0.64	0.49	1.01	1.12	0.63
15	0.30	0.42	0.33	0.27	0.37	0.42	0.28	0.18
16	0.32	0.18	0.32	0.50	0.16	0.11	0.16	0.18

Table 4.10 | Frequency of the AGG motif as a function of position along the 18-mer in experimental and control ssDNA libraries from SELEC rounds 3-6.

AGG Motif								
Position	ER3	ER4	ER5	ER6	CR3	CR4	CR5	CR6
1	1.35	0.98	1.51	1.86	1.76	1.28	0.22	0.89
2	0.70	0.94	0.58	1.10	0.89	0.55	0.00	0.37
3	0.77	0.92	0.73	1.11	0.94	0.20	0.09	0.22
4	0.57	0.47	0.68	0.65	0.70	0.47	0.07	0.14
5	0.73	0.78	0.76	0.59	0.87	0.16	0.05	0.13
6	0.53	0.38	0.63	0.51	0.43	0.11	0.00	0.05
7	0.62	0.87	0.31	0.53	0.41	0.16	0.00	0.08
8	0.55	0.79	0.48	0.70	0.70	0.16	0.00	0.10
9	0.90	0.32	0.40	0.45	0.64	0.22	0.00	0.00
10	0.68	0.23	0.30	0.40	0.32	0.39	0.00	0.18
11	0.52	0.56	0.09	0.60	0.43	0.11	0.00	0.06
12	0.78	0.64	0.13	0.73	0.38	0.26	0.00	0.03
13	0.34	0.52	0.27	0.41	0.28	0.05	0.00	0.00
14	0.48	0.58	0.63	0.51	0.37	0.15	0.00	0.00
15	0.30	0.18	0.23	0.17	0.10	0.05	0.00	0.00
16	0.45	0.62	0.49	0.40	0.10	0.19	0.00	0.00

Table 4.11 | Frequency of the CAC motif as a function of position along the 18-mer in experimental and control ssDNA libraries from SELEC rounds 3-6.

CAC Motif								
Position	ER3	ER4	ER5	ER6	CR3	CR4	CR5	CR6
1	0.21	0.17	0.00	0.09	0.10	0.22	0.07	0.13
2	0.53	0.47	0.19	0.42	0.37	2.13	4.98	1.34
3	0.15	0.22	0.27	0.30	0.34	2.36	4.14	1.18
4	0.23	0.46	0.32	0.54	0.46	1.41	3.28	1.11

5	0.26	0.18	0.14	0.26	0.21	1.99	4.49	1.30
6	0.38	0.13	0.34	0.27	0.33	1.35	2.68	0.72
7	0.35	0.43	0.14	0.48	0.44	1.03	2.65	0.81
8	0.41	0.24	0.22	0.35	0.52	1.12	2.52	1.08
9	0.35	0.15	0.17	0.69	0.18	1.20	1.82	0.77
10	0.34	0.40	0.20	0.31	0.52	1.62	3.34	1.16
11	0.35	0.44	0.23	0.46	0.20	0.98	1.56	0.83
12	0.22	0.45	0.26	0.18	0.33	0.80	2.25	0.86
13	0.34	0.48	0.13	0.28	0.21	0.69	0.94	0.32
14	0.08	0.21	0.09	0.15	0.11	0.67	0.72	0.21
15	0.27	0.08	0.27	0.13	0.17	0.16	0.25	0.08
16	0.08	0.05	0.00	0.04	0.00	0.00	0.00	0.00

Table 4.12 | Frequency of the CGG motif as a function of position along the 18-mer in experimental and control ssDNA libraries from SELEC rounds 3-6.

CGG Motif								
Position	ER3	ER4	ER5	ER6	CR3	CR4	CR5	CR6
1	0.12	0.44	0.09	0.17	0.00	0.00	0.00	0.00
2	1.16	0.76	0.45	1.25	1.17	0.95	1.06	0.86
3	0.63	0.84	0.72	0.73	1.19	1.45	0.07	0.66
4	0.74	0.85	0.51	0.93	0.97	0.79	0.08	0.45
5	0.48	0.62	0.24	0.62	0.99	0.55	0.17	0.27
6	0.67	0.60	0.31	0.37	0.49	0.59	0.00	0.25
7	0.62	0.47	0.38	0.73	0.21	0.22	0.11	0.18
8	0.60	0.43	0.20	0.21	0.56	0.05	0.03	0.03
9	0.55	0.43	0.04	0.56	0.54	0.27	0.00	0.03
10	0.51	1.01	0.09	0.32	0.57	0.27	0.11	0.08
11	1.04	0.51	0.23	0.43	0.33	0.20	0.09	0.12
12	0.55	0.56	0.18	0.68	0.51	0.24	0.27	0.20
13	0.72	0.48	0.27	0.27	0.67	0.44	0.03	0.22
14	0.90	0.62	0.18	0.66	0.82	0.79	0.56	0.66
15	0.82	0.62	0.24	0.49	0.42	0.22	0.00	0.00
16	0.93	0.78	0.09	0.34	0.57	0.38	0.37	0.27

Table 4.13 | Frequency of the GCA motif as a function of position along the 18-mer in experimental and control ssDNA libraries from SELEC rounds 3-6.

GCA Motif								
Position	ER3	ER4	ER5	ER6	CR3	CR4	CR5	CR6
1	0.70	0.57	0.22	0.75	0.42	1.25	1.13	0.54

2	0.27	0.61	0.22	0.69	0.79	1.30	2.00	0.70
3	1.09	1.00	0.89	1.48	0.52	1.03	0.84	0.91
4	0.65	0.38	0.33	1.10	0.52	1.16	1.51	0.86
5	0.56	0.40	0.63	0.54	0.75	0.87	0.46	0.58
6	0.55	0.96	0.41	1.09	0.57	1.13	0.64	0.51
7	0.35	0.42	0.45	1.08	0.33	0.43	0.26	0.50
8	0.67	0.50	0.35	0.46	0.76	0.64	0.52	0.67
9	0.39	0.54	0.33	0.61	0.37	1.02	0.42	0.55
10	0.32	0.34	0.26	0.52	0.26	0.43	0.14	0.50
11	0.27	0.13	0.05	0.28	0.38	0.43	0.40	0.23
12	0.25	0.76	0.36	0.69	0.37	0.92	0.42	0.24
13	0.28	0.12	0.22	0.31	0.15	0.38	0.28	0.40
14	0.44	0.38	0.18	0.29	0.12	0.27	0.08	0.13
15	0.71	0.39	0.22	0.34	0.16	0.16	0.03	0.21
16	0.43	0.44	0.34	0.30	0.22	0.59	0.43	0.19

Table 4.14 | Frequency of the GCC motif as a function of position along the 18-mer in experimental and control ssDNA libraries from SELEC rounds 3-6.

GCC Motif								
Position	ER3	ER4	ER5	ER6	CR3	CR4	CR5	CR6
1	0.14	0.13	0.14	0.30	0.43	0.46	0.14	0.29
2	0.26	0.13	0.16	0.26	0.37	0.58	0.55	1.04
3	0.34	0.25	0.09	0.40	0.47	0.72	0.57	0.41
4	0.60	0.14	0.26	0.42	0.29	0.55	0.27	0.40
5	0.52	0.42	0.13	0.51	0.45	0.38	0.15	0.27
6	0.37	0.23	0.09	0.36	0.45	0.71	0.44	0.19
7	0.38	0.33	0.22	0.25	0.20	0.51	0.22	0.36
8	0.36	0.41	0.17	0.09	0.31	0.38	0.58	0.40
9	0.43	0.30	0.04	0.26	0.15	0.43	0.31	0.43
10	0.36	0.31	0.32	0.22	0.49	0.22	0.33	0.30
11	0.44	0.00	0.09	0.30	0.51	0.67	0.56	0.40
12	0.41	0.40	0.09	0.40	0.49	0.76	0.43	0.30
13	0.73	0.46	0.20	0.27	0.15	0.22	0.30	0.13
14	0.17	0.26	0.04	0.18	0.38	0.32	0.16	0.05
15	0.09	0.47	0.22	0.32	0.49	0.53	0.77	0.11
16	0.04	0.04	0.00	0.04	0.00	0.00	0.00	0.00

Table 4.15 | Frequency of the GGC motif as a function of position along the 18-mer in experimental and control ssDNA libraries from SELEC rounds 3-6.

GGC Motif								
Position	ER3	ER4	ER5	ER6	CR3	CR4	CR5	CR6
1	0.50	0.58	0.20	0.66	0.58	0.33	0.37	0.51
2	0.73	0.71	0.44	1.04	0.86	0.79	0.27	0.50
3	1.10	0.67	0.55	1.70	1.13	0.86	0.83	0.62
4	1.25	0.83	0.40	1.03	0.77	0.64	0.08	0.37
5	0.81	0.94	0.55	0.72	0.72	0.75	0.08	0.30
6	0.56	0.23	0.28	0.64	0.58	0.16	0.20	0.40
7	0.73	0.48	0.22	0.38	0.63	0.27	0.03	0.09
8	0.57	0.32	0.20	0.39	0.47	0.37	0.11	0.13
9	0.62	0.52	0.37	0.51	0.37	0.16	0.00	0.05
10	0.65	0.09	0.05	0.33	0.34	0.31	0.00	0.06
11	0.67	0.72	0.04	0.45	0.37	0.44	0.11	0.10
12	1.23	0.67	0.18	0.50	0.43	0.11	0.09	0.08
13	0.48	0.69	0.04	0.79	0.37	0.18	0.27	0.23
14	0.69	0.61	0.32	0.55	0.60	0.22	0.03	0.08
15	1.09	0.66	0.52	0.75	0.81	0.60	0.54	0.43
16	0.21	0.25	0.06	0.05	0.17	0.05	0.00	0.03

Table 4.16 | Frequency of the GTG motif as a function of position along the 18-mer in experimental and control ssDNA libraries from SELEC rounds 3-6.

GTG Motif								
Position	ER3	ER4	ER5	ER6	CR3	CR4	CR5	CR6
1	0.88	0.55	0.45	0.73	0.47	0.58	0.00	0.29
2	0.61	0.52	0.22	0.52	0.94	0.22	0.00	0.07
3	0.93	0.57	0.68	0.48	0.91	0.17	0.00	0.22
4	0.90	0.60	0.68	0.88	0.91	0.69	0.00	0.33
5	0.71	1.10	0.68	0.70	0.98	0.51	0.00	0.24
6	0.41	1.13	0.79	0.43	0.93	0.64	0.00	0.38
7	0.68	0.56	0.32	0.56	0.90	0.58	0.02	0.12
8	0.46	0.61	0.69	0.53	0.86	0.56	0.00	0.25
9	0.45	0.49	0.36	0.24	0.96	0.37	0.03	0.41
10	0.57	0.53	0.62	0.48	0.79	0.44	0.00	0.27
11	0.75	0.65	0.51	0.22	0.86	0.83	0.03	0.34
12	0.43	0.48	0.60	0.42	1.47	0.71	0.08	0.72
13	0.92	0.79	0.81	0.90	1.17	0.90	0.05	0.85

14	1.08	0.95	0.97	1.11	3.37	3.04	0.64	2.48
15	1.09	0.73	1.35	1.07	1.57	2.08	0.11	0.82
16	2.28	1.79	1.87	2.07	6.23	6.15	2.16	4.35

4.6.3 Supporting figures

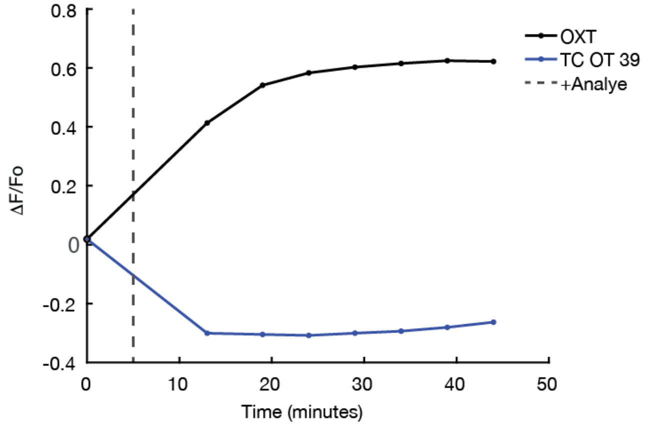

Figure 4.10 | Time-dependent response of nIROSE to TC OT 39. The ΔF/F$_o$ of nIROSE upon incubation with either 50 μM OXT (black) or TC OT 39 (blue). Fluorescence measurements were obtained every 5 minutes up to 40 minutes after the addition of analyte. Circles represent the mean of n=3 experimental measurements. ΔF/F$_o$ is calculated from the normalized change in peak intensity at 1195 nm.

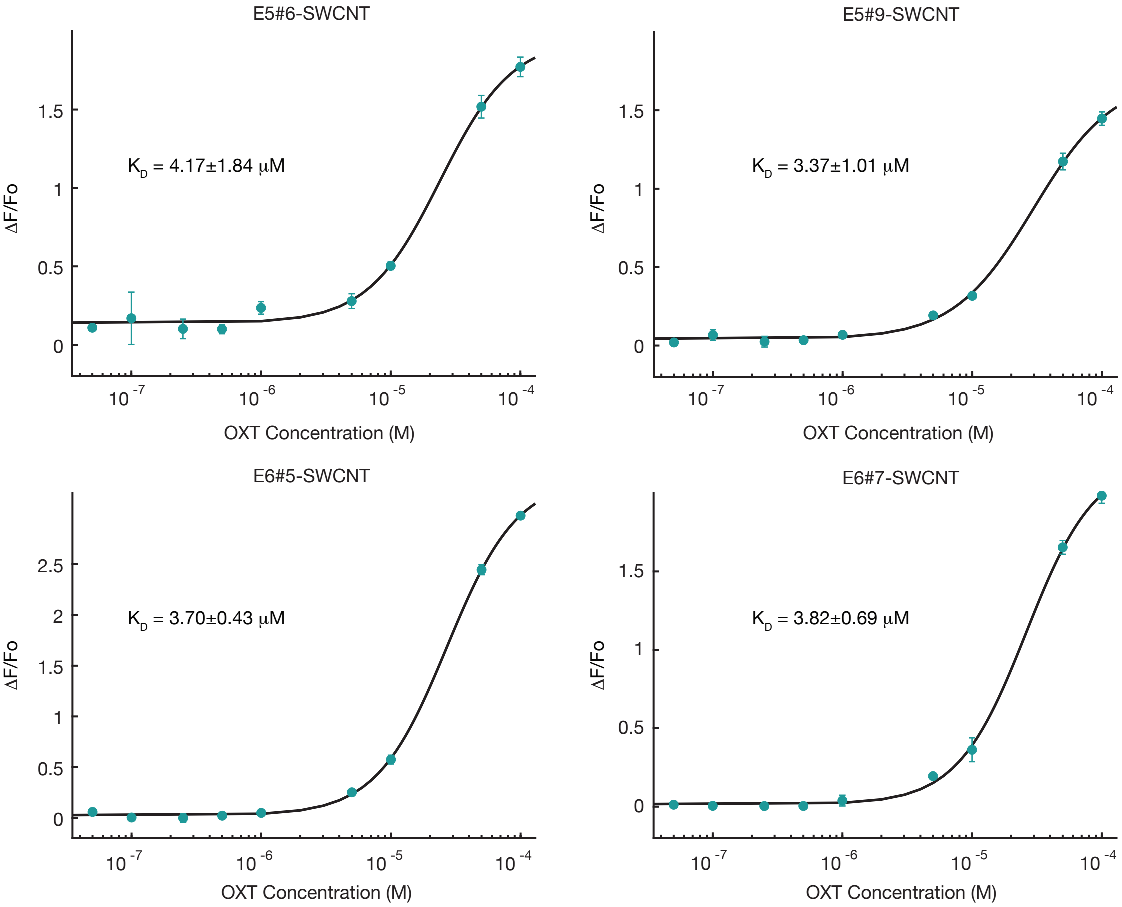

Figure 4.11 | Dose response curve of top ssDNA-SWCNT nanosensor candidates. The oxytocin sensitivity and binding kinetics of four additional nanosensor candidates (E5#6, E5#9, E6#5, and E6#7) were characterized. Blue circles and error bars represent the mean of n=3 experimental measurements and the standard deviation of these measurements, respectively. $\Delta F/F_o$ is calculated from the normalized change in peak intensity at 1195 nm after 20 minutes. The black line represents the cooperative binding model fit to experimental data. The K_d value is reported with 95% confidence intervals using the t-distribution.

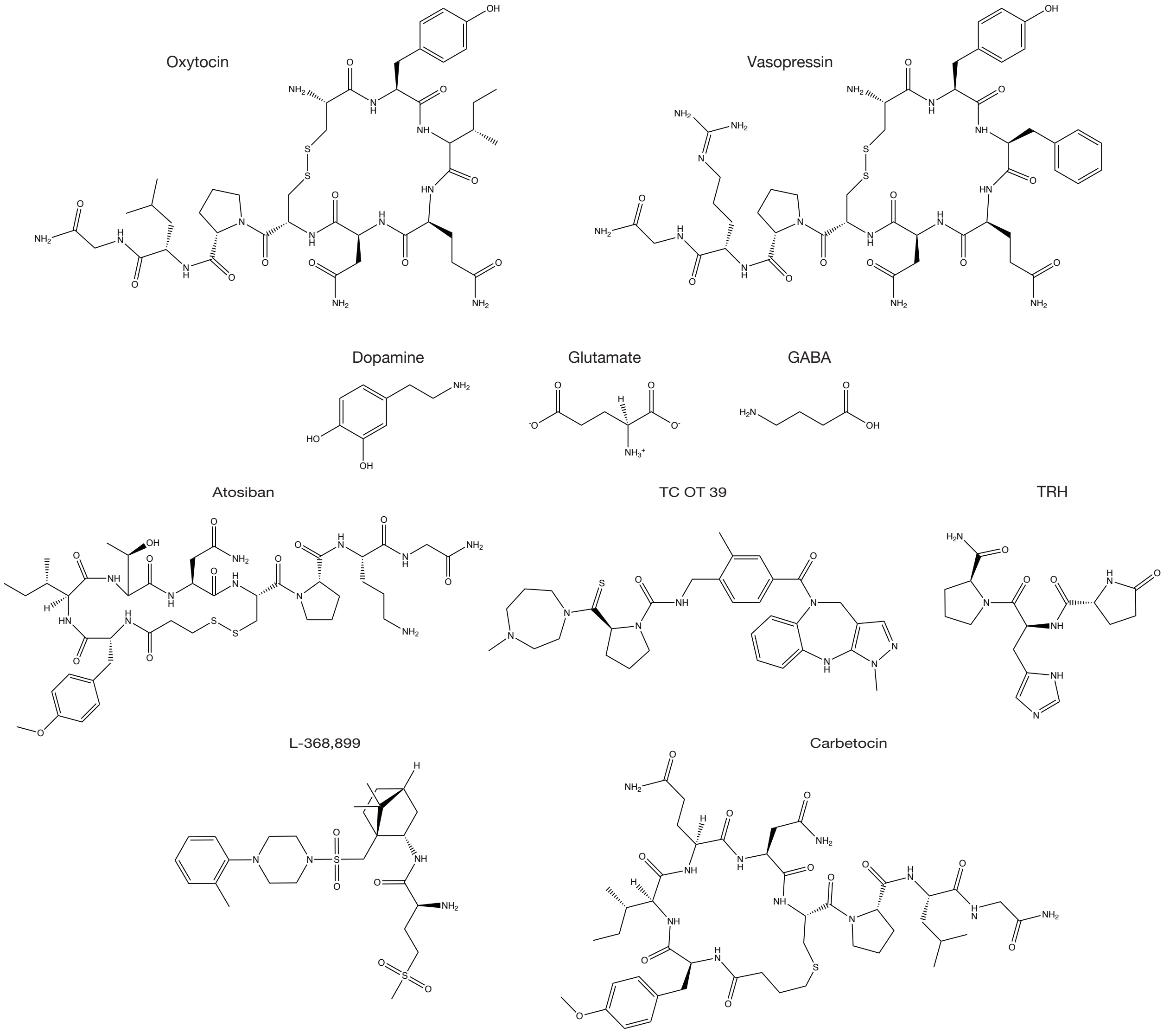

Figure 4.12 | Neurochemicals and oxytocin-receptor targeted pharmacological agents used in nIROSE selectivity screening. Structure of oxytocin, vasopressin, dopamine, glutamate, ɣ-aminobutyric acid (GABA), thyrotropin-releasing hormone (TRH), atosiban, TC OT 39, L-368,899, and carbetocin.

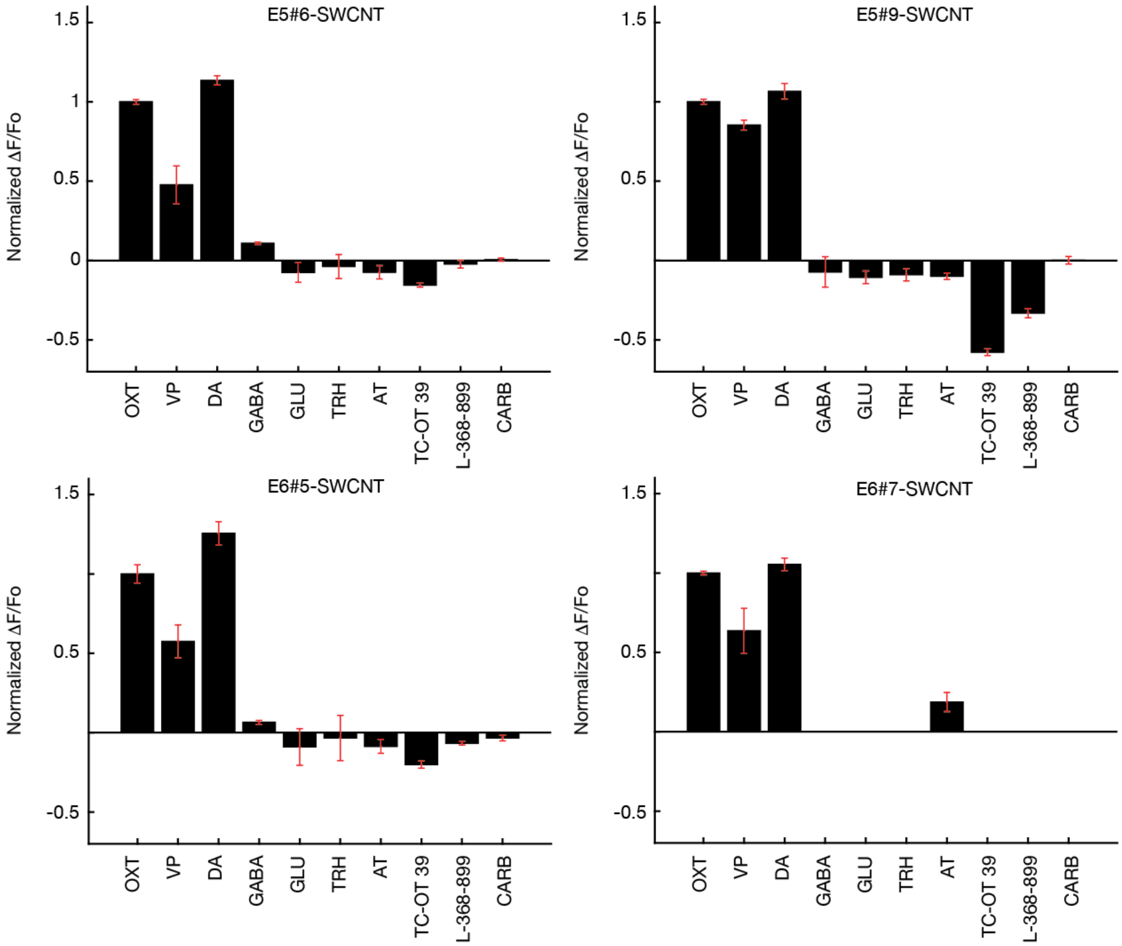

Figure 4.13 | Selectivity of top ssDNA-SWCNT nanosensor candidates. Nanosensor selectivity screening at 50 μM oxytocin (OXT), vasopressin (VP), dopamine (DA), glutamate (GLU), γ-aminobutyric acid (GABA), thyrotropin-releasing hormone (TRH), atosiban (AT), TC-OT 39, L-368,899, and carbetocin (CARB). Black bars represent the mean $\Delta F/F_o$ at 1195 nm from n=3 replicates normalized to OXT response after 20 minutes, with standard deviation of these replicates shown in red. E6#7-SWCNT were not screened for response to glutamate (GLU), γ-aminobutyric acid (GABA), thyrotropin-releasing hormone (TRH), TC OT 39, L-368,899, or carbetocin (CARB).

4.7 Future directions

While the data included above demonstrate that nIROSE is a sensitive oxytocin imaging probe capable of imaging oxytocin release in brain tissue, additional experiments are needed for further *in vitro* and *ex vivo* validation.

For *in vitro* validation, a nanosensor construct containing a scrambled E6#4 construct should be synthesized and screened for oxytocin response. It is expected that this scrambled construct will have a negligible optical response to oxytocin and provide verification that nIROSE response to oxytocin occurs via molecular recognition between the E6#4 aptamer identified via SELEC and neuropeptide oxytocin. nIROSE was shown to respond with oxytocin with nanomolar sensitivity, but the limit of detection (LOD) of this nanosensor must also be quantified. Fluorescence should be tracked for 20 minutes both with and without the addition of PBS; LOD can be calculated from these data using the equation in Chapter 3.6.1. The reversibility of nIROSE-oxytocin binding should also be demonstrated on a glass substrate. To conduct this experiment, nIROSE should be immobilized on glass using the same drop casting procedure detailed in Chapter 4.5.5. Nanosensor integrated fluorescence can then be tracked with repeated incubation with oxytocin followed by washes with PBS. This experiment will explicitly demonstrate that sensing occurs via reversible binding between nIROSE and oxytocin. It is also suggested that additional data points are collected along the nIROSE dose response curve, especially where the slope is steepest (i.e. 25 μM) at near the point of saturation (i.e. 200 μM). Quantification of nIROSE response at these oxytocin concentrations is needed for a more accurate calculation of 1) dynamic range and 2) binding affinity (K_D). As shown through the selectivity screening in Figure 4.7b, nIROSE lacks selectivity against dopamine. Dopamine sensitivity limits the utility of nIROSE to non-dopaminergic regions of the brain such as the PVN or SON or requires the use of dopamine-suppressing agents to explore oxytocin signaling in dopaminergic regions. D2 receptor agonists, such as quinpirole, have been shown to attenuate dopamine release and would enable nIROSE-based oxytocin imaging in regions such as the nucleus accumbens. Prior to these imaging experiments, however, compatibility between nIROSE and dopamine-targeted drugs must be demonstrated. It is suggested that additional selectivity screening is conducted for pharmacological agents such as quinpirole.

For *ex vivo* validation, the next steps of this project include: 1) further validation of nIROSE for imaging electrically stimulated oxytocin release in the PVN of acute brain slices through additional experimental and biological replicates, 2) evaluating the effect of pharmacological agents such as L-368,899 and carbetocin on stimulated oxytocin release in the PVN of acute brain slices 3) validating the use of nIROSE for imaging optogenetically stimulated oxytocin release as a positive control. Because nIROSE is compatible with oxytocin receptor-targeted drugs, these nanosensors can be used to explore if and how pharmacology affects oxytocin release. For example, a reduction in nIROSE response upon incubation with an oxytocin receptor agonist would provide evidence of a feedback loop between receptor uptake of oxytocin and oxytocin release. The bright baseline fluorescence of nIROSE might also enable oxytocin imaging in brain regions that are currently infeasible with nIROx. The low signal-to-noise ratio of nIROx nanosensors limit their use to the PVN, where oxytocin release is highest. nIROSE, on the other hand, might be used to explore how oxytocin dynamics (e.g. the time scale of release and reuptake or quantity of release) differs among regions such as the PVN, SON, and lateral septum. While preliminary experiments suggest that nIROSE can image oxytocin release in brains, it is possible that nIROSE nanosensors are proven incompatible with in slice imaging. In this case, it is suggested that different nanosensor candidates are explored. In addition to E6#4, there are 4 nanosensors that demonstrate similar selectivity and sensitivity for oxytocin, E5#6, E5#9, E6#5, and E6#7 (Figures 4.11 and 4.13).

It is also suggested that additional nanosensor candidates are designed using the nucleotide and motif analysis described in Chapter 4.3.1. Several nucleotide motifs were identified among enriched sequences of the experimental SELEC library; these analyses may enable the intelligent design of a nanosensor construct with improved sensitivity and selectivity over nIROSE. For example, a sequence can be designed which contains repeating GGC and AGG trimers, which were present at high frequencies throughout rounds of SELEC or the highest frequency nucleotide at each position along the 18-mer.

Appendix I

Aptamer-SWCNT for point-of-care SARS CoV-2 detection

The number of deaths caused by the novel coronavirus disease (COVID-19) and the spread of the virus that causes it, SARS CoV-2, led the World Health Organization to declare COVID-19 a global pandemic on March 12, 2020. As of October 21, 2022, the (WHO) has reported nearly 625 million COVID-19 cases globally with nearly 400,000 new global cases reported that day.[194] Scientists around the world worked at unprecedented speeds to characterize the SARS CoV-2 virus, and within two weeks of publishing of its genome, the first COVID-19 diagnostic tests were developed[195]. Since then, these diagnostic tests have helped spread public awareness of the disease, enabled treatment of infected individuals, and identified infected individuals to limit transmission and improve public health outcomes. Some of the diagnostic technologies developed over the course of the pandemic include reverse transcription-quantitative polymerase chain reaction (RT-qPCR), next-generation sequencing, isothermal nucleic acid amplification assays, antigen tests, and serological tests. Based on factors such as cost, sensitivity, and speed, these tests are appropriate in different settings and for different applications. Antigen tests, for example, often demonstrate diminished sensitivity and selectivity, but are rapid, inexpensive, and can be performed by untrained individuals at home.[196, 197] The first antigen tests were FDA approved in December 2020[198] and have since been used globally for point-of-care testing.

Before the FDA approval of antigen tests, our lab began development of SWCNT-based antigen tests for SARS CoV-2. Pinals *et al.* developed a SWCNT-based sensor that harnesses the affinity of the angiotensin-converting enzyme 2 (ACE2) receptor for the receptor binding domain (RBD) of the viral Spike protein[149]. The ACE2-SWCNT sensing platform demonstrated a 12.6 nM limit of detection for Spike RBD and maintained its sensitivity upon surface immobilization, suggesting its potential use for point-of-care testing. This work demonstrated that SWCNT-based technologies are viable viral detection platforms and motivated the development of an ssDNA-SWCNT antigen test as described below.

In June 2020, Song *et al.* used an ACE2 competition-based aptamer selection procedure to identify ssDNA sequences with affinity for the RBD of Spike glycoprotein[199]. They discovered two aptamers, 1C and 4C (Figure A.1), that bind Spike with K_d = 5.8 nM and 19.9 nM, respectively. We sought to leverage the near-infrared fluorescence of SWCNT and the molecular recognition of the 1C/4C DNA aptamers to develop a fluorescent SARS CoV-2 antigen test for resource limited settings. Spike is an ideal target for antigen testing due to its high density on SARS-CoV-2 virions,[200] and a DNA-based sensor would provide a low-cost, high-stability alternative to the ACE2-based sensing platform introduced above.

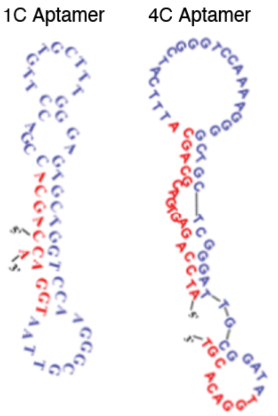

Figure A.1 | Sequence and structure of Spike RBD-binding aptamers. These ssDNA aptamers, 1C (left) and 4C (right) were identified by an ACE2 competition-based aptamer selection procedure and demonstrate nanomolar affinity for Spike RBD. *Reprinted from Song et al. to show aptamer secondary structure*[199].

We first synthesized the 1C/4C aptamers with a terminal polycytosine tail (C_6) to enable adsorption to the SWCNT surface, as described in Chapter 4. Polycytosines were added to the 5' end of the Spike-binding aptamers to produce C1C and C4C aptamers (C1C = CCCCCCCAGCACCGACCTTGTGCTTTGGGAGTGCTGGTCCAAGGGCGTTAATGGACA, C4C = CCCCCCATCCAGAGTGACGCAGCATTTCATCGGGTCCAAAAGGGGCTGCTCGGGATTGCGGATATGGACACGT, Integrated DNA Technologies, Inc). C1C/C4C aptamers were then noncovalently adsorbed to the SWCNT surface using a sonication strategy. SWCNT slurry (900 µL, 0.22 mg/mL in 1X PBS)) was mixed with ssDNA (100 µL, 1 mM) and probe-tip sonicated (3 mm probe tip, 50% amplitude, 5 W) in an ice bath for 10 minutes. Constructs were centrifuged at 16,000xg for 90 minutes, and the concentration of the supernatant was determined by measuring the absorbance at 632 nm. Constructs were diluted to 5 mg/L in 1X PBS before use in fluorescence measurements. This synthesis strategy produced ssDNA-SWCNT constructs with a bright baseline fluorescence (Figure A.2). Upon screening with Spike RBD, however, these constructs were unresponsive (Figure A.3) and thus unsuitable as SARS CoV-2 sensors. We hypothesized that the probe tip sonication protocol may have disrupted the secondary structure of C1C and C4C aptamers and thus diminished their binding affinity for Spike RBD.

To maintain the aptamer secondary structure, we pursued two strategies: 1) refolding of the aptamer after adsorption to the SWCNT surface and 2) adsorption to the SWCNT surface with a gentle ligand exchange protocol. To refold the aptamers after synthesis, C1C/C4C-SWCNT prepared via probe-tip sonication were heated at 95°C for 5 minutes and cooled to room temperature in refolding buffer (1X PBS, 1 mM $MgCl_2$). This protocol was previously demonstrated to enable refolding of adsorbed aptamers on the SWCNT surface without desorption[20]. Refolding of sonicated constructs resulted in an increase in baseline fluorescence (Figure A.2), suggesting a change in aptamer-SWCNT interactions. The refolded constructs were, however, still unresponsive to Spike RBD (Figure A.3), suggesting that refolding after sonication did not return the C1C/C4C aptamers the structure requisite for Spike binding.

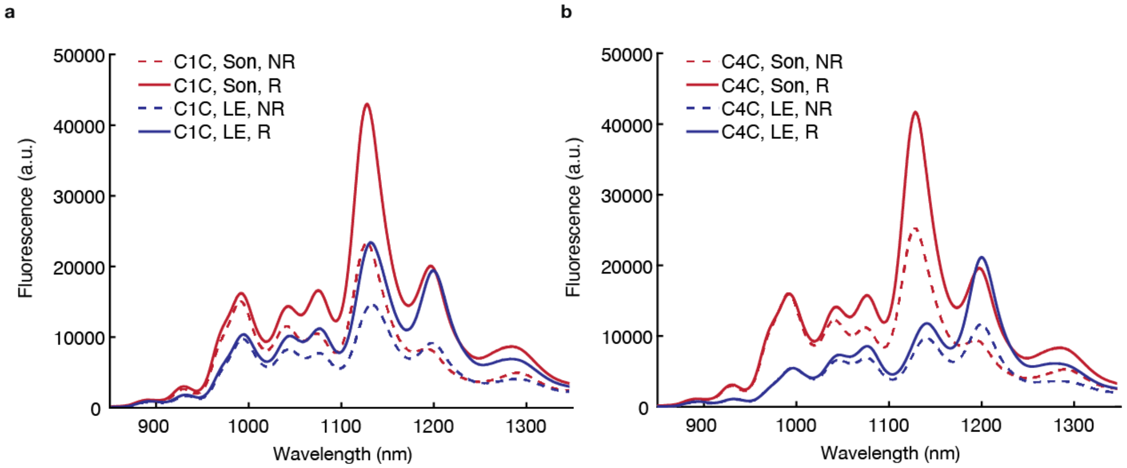

Figure A.2 | Effect of aptamer refolding on nanosensor baseline fluorescence. a,b Full near-infrared fluorescence emission spectra of C1C-SWCNT (left) and C4C-SWCNT (right) prepared by either sonication ("Son", red traces) or ligand exchange ("LE", blue traces). After synthesis, some constructs were heated at 95°C and cooled to room temperature to refold adsorbed aptamers ("R", solid traces). Constructs that were not subjected to the refolding procedure are also shown ("NR", dashed traces). Spectral characteristics vary across synthetic strategy and refolding procedure suggesting differences in aptamer-SWCNT interactions.

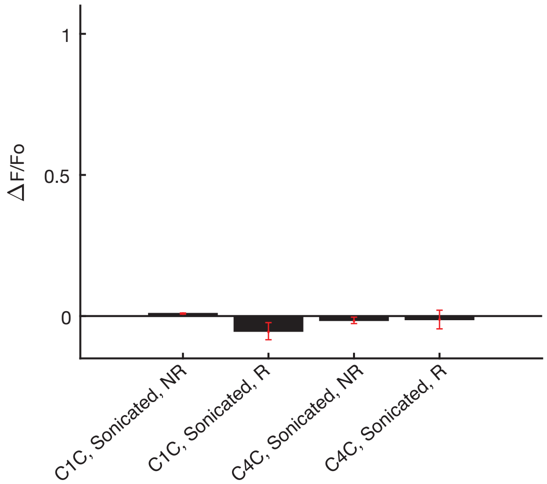

Figure A.3 | Nanosensor response to 1 µM RBD. Black bars represent the mean $\Delta F/F_o$ at 1290 nm from n=3 replicates, with standard deviation of these replicates shown in red. All nanosensors were prepared via probe-tip sonication. After synthesis, some constructs were heated at 95°C and cooled to room temperature to refold adsorbed aptamers ("R"). Constructs that were not subjected to the refolding procedure are also shown ("NR").

We then pursued a second strategy to maintain aptamer secondary structure and prepared ssDNA-SWCNT by ligand exchange[201]. During ligand exchange, sodium cholate is slowly exchanged for a ssDNA aptamer on the SWCNT surface. We hypothesized that ligand exchange would enable construct synthesis without disruption of the aptamer secondary structure. To prepare constructs, sodium cholate (SC)-SWCNT were first prepared by sonication. Sodium cholate (1 g) was mixed with SWCNT (11 mg) in 50 mL water and probe-tip sonicated (6 mm probe tip, 25% amplitude, 1 second on/1 second off pulse) for 20 minutes in an ice bath. SC-SWCNT were centrifuged for 90 minutes at

16,000xg, and the supernatant was collected. The concentration of SC-SWCT was determined by measuring the absorbance at 632 nm. SC is an effective SWCNT dispersant in aqueous solutions[202] that yields constructs with a bright baseline fluorescence when adsorbed to SWCNT (Figure A.4). SC-SWCNT and either the C1C or C4C aptamer were then dialyzed against dialysis buffer to facilitate the exchange of SC for ssDNA on the SWCNT surface. SC-SWCNT and aptamers were mixed in a 1:5 mass/mass ratio in NaCl buffer (0.1 M) and placed in dialysis tubing (3.5 kDa MWCO, 45 mm width, Spectrum Spectra/Por). The mixture was dialyzed for 24 hours at room temperature against NaCl solution (2 L, 0.1 M) with 3 dialysis buffer exchanges. The resulting ligand exchange products were centrifuged at 16,000xg for 90 minutes, and the supernatant was collected. Constructs were diluted to 5 mg/L in 1X PBS before use in fluorescence measurements.

Consistent with previous findings[201], the fluorescence spectra of C1C/C4C-SWCNT were red-shifted from that of SC-SWCNT (Figure A.4). The observed solvatochromatic shift is indicative of the sparser coverage on the SWCNT surface by ssDNA than by small, densely packed sodium cholate molecules. The spectral characteristics of constructs prepared via probe-tip sonication and ligand exchange were significantly different (Figure A.2), indicating that aptamer-SWCNT interactions varied by synthesis strategy.

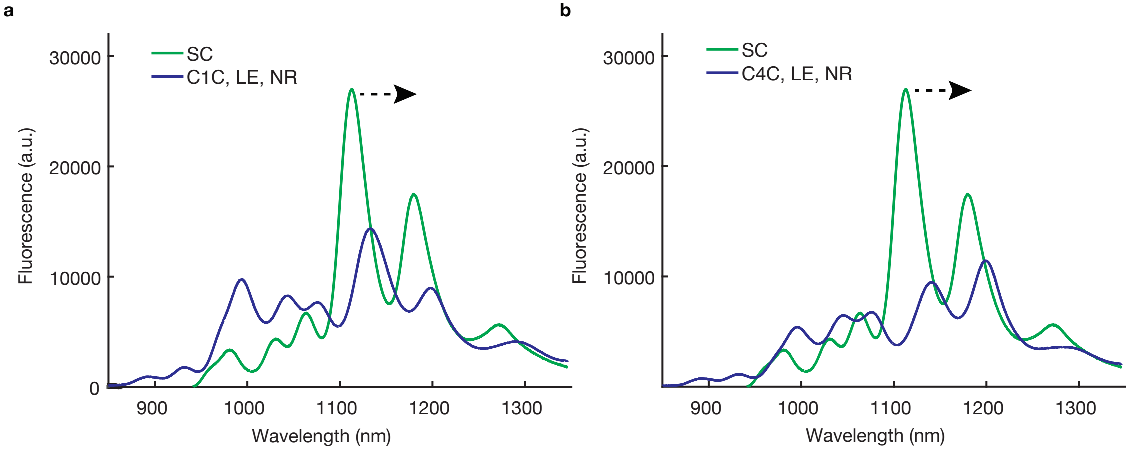

Figure A.4 | Effect of ligand exchange on nanosensor baseline fluorescence. a,b Near-infrared fluorescence emission of sodium cholate (SC)-SWCNT (green) and either C1C-SWCNT (left) or C4C-SWCNT prepared by ligand exchange. ("LE", blue). These sensors were not subjected to the refolding procedure ("NR"). After ligand exchange, sodium cholate was successfully exchanged for RBD-binding aptamers on the surface of SWCNT, as indicated by a red-shift in baseline fluorescence. The observed solvatochromatic shift is due to a decrease in SWCNT surface coverage by ssDNA compared to sodium cholate molecules.

C1C-SWCNT and C4C-SWCNT prepared via ligand exchange were then screened for Spike RBD response (Figures A.5 and A.6). While some C1C-SWCNT nanosensor batches responded strongly to 1 μM Spike RBD with $\Delta F/F_o = 1.17$, some batches demonstrated a negligible response $\Delta F/F_o = -0.02$. These results suggest that aptamer secondary structure on the SWCNT surface varies significantly, batch to batch, even when synthesized with the same ligand exchange protocol.

We next evaluated the dose response of responsive batches to Spike RBD (100 pm-1 μM) and evaluated the utility of aptamer refolding on the SWCNT surface after ligand exchange (Figure). We hypothesized that aptamer refolding may improve nanosensor performance and confer consistency

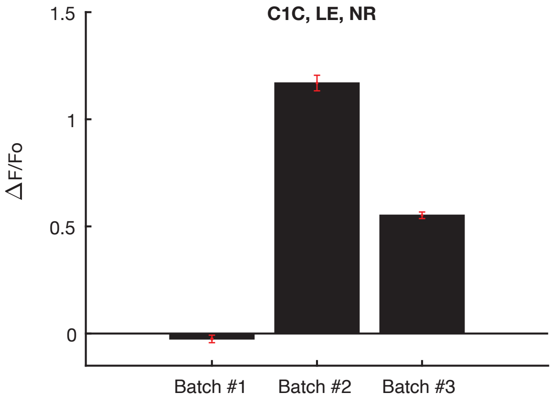

Figure A.5 | C1C-SWCNT response to 1 µM RBD. Black bars represent the mean $\Delta F/F_o$ at 1290 nm from n=3 replicates, with standard deviation of these replicates shown in red. All nanosensors were prepared via ligand exchange. These sensors were not subjected to the refolding procedure. Although all nanosensors were synthesized with the same procedure, there is significant batch to batch variability in RBD response.

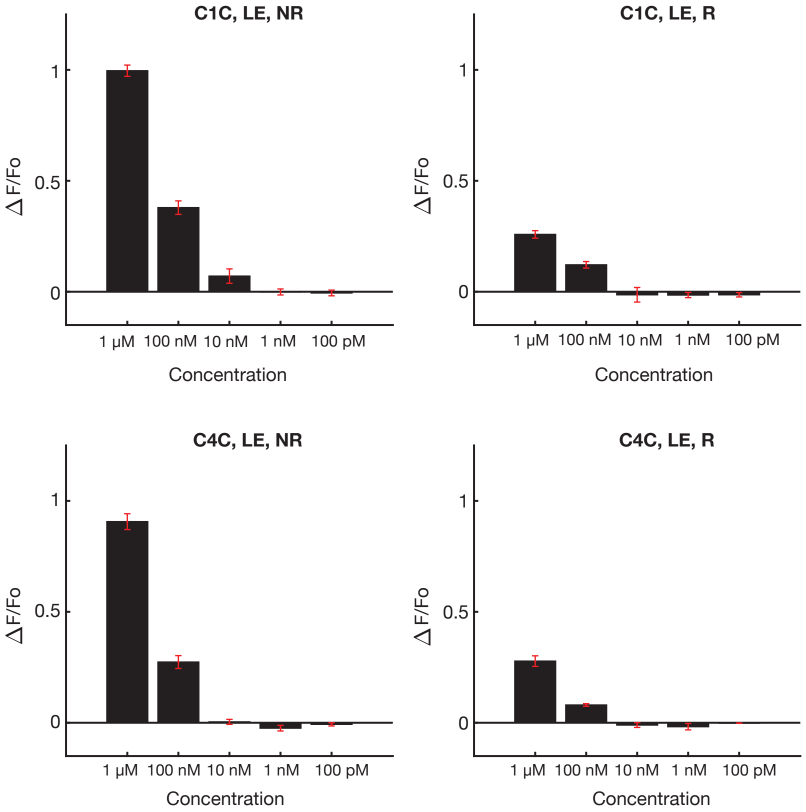

Figure A.6 | Nanosensor dose response to RBD. C1C-SWCNT (top) and C4C-SWCNT (bottom) nanosensors were screened for response to RBD at various concentrations (100 pM-1 µM). Black bars represent the mean $\Delta F/F_o$ at 1290 nm from n=3 replicates, with standard deviation of these replicates shown in red. All nanosensors were prepared via ligand exchange. After synthesis, some constructs were heated at 95°C and cooled to room temperature to refold adsorbed aptamers ("R"). Constructs that were not subjected to the refolding procedure are also shown ("NR"). The refolding procedure did not improve nanosensor response to RBD.

across batches; aptamers were refolded using the same strategy described above. All nanosensors responded in a concentration dependent manner to Spike RBD regardless of refolding strategy, but non-refolded nanosensors demonstrated a larger fluorescence response to RBD than refolded nanosensors. Baseline fluorescence measurements of these constructs suggest that the refolding protocol modulated aptamer-SWCNT interactions after ligand exchange and are thus consistent with the measurements of sonicated constructs before and after refolding (Figure A.2). Taken together, these data suggest that refolding affects aptamer secondary structure on the surface of SWCNT but does not improve nanosensor performance.

Responsive nanosensors prepared via ligand exchange were then evaluated for selectivity over other viral proteins at both 1 μM and 100 nM (Figures A.7 and A.8). Fluorescence response to MERS/CoV-1 RBD and Flu hemagglutinin subunit (HA1) protein varied significantly by nanosensor type, batch, and viral protein concentration. None of the nanosensor batches tested were selective for SARS CoV-2 Spike RBD at 1 μM.

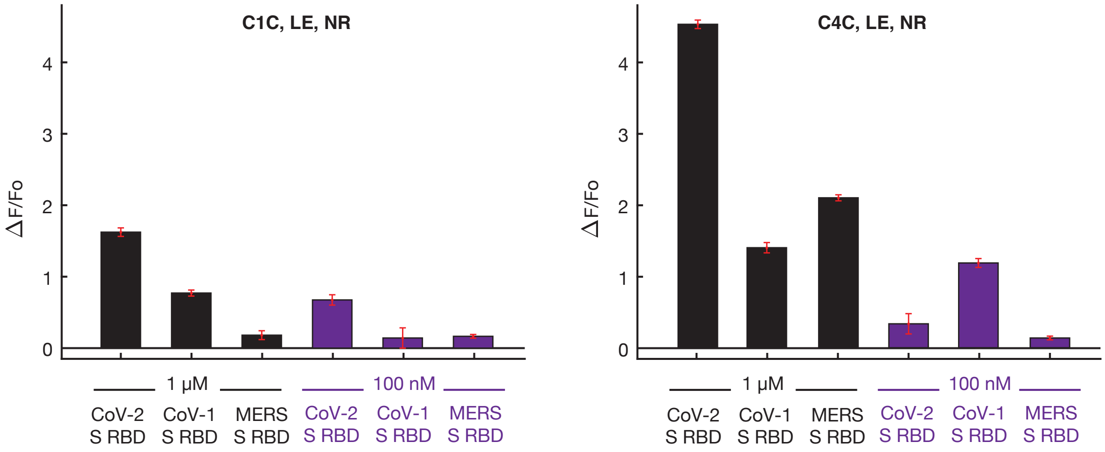

Figure A.7 | Nanosensor selectivity over viral proteins. One batch of C1C-SWCNT (left) and C4C-SWCNT (right) nanosensors were screened for response to viral proteins, SARS CoV-2 Spike RBD, SARS CoV-1 Spike RBD, and MERS Spike RBD at two concentrations, 1 μM (black) and 100 nM (purple). Bars represent the mean $\Delta F/F_o$ at 1290 nm from n=3 replicates, with standard deviation of these replicates shown in red. All nanosensors were prepared via ligand exchange ("LE"). These nanosensors were not subjected to the refolding procedure ("NR").

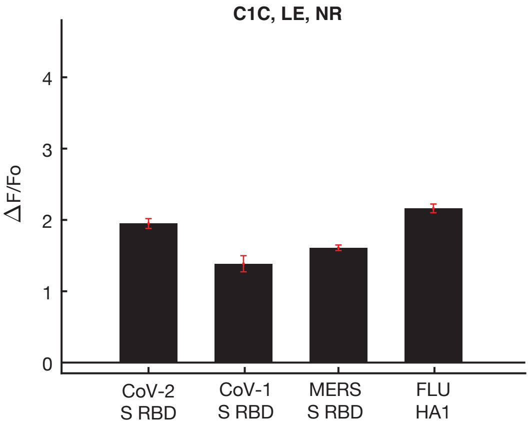

Figure A.8 | C1C-SWCNT selectivity over viral proteins. Another batch of C1C-SWCNT nanosensors were screened for response to viral proteins, SARS CoV-2 Spike RBD, SARS CoV-1 Spike RBD, MERS Spike RBD, and Flu hemagglutinin subunit (HA1) at 1 μM. Black bars represent the mean $\Delta F/F_o$ at 1290 nm from n=3 replicates, with standard deviation of these replicates shown in red. All nanosensors were prepared via ligand exchange ("LE"). These nanosensors were not subjected to the refolding procedure ("NR").

As nanosensor response was challenging to reproduce consistently across batches, and most nanosensor batches did not demonstrate selectivity for SARS CoV-2 Spike RBD, further nanosensor development was halted. Although 1C and 4C aptamers demonstrated high affinity for Spike RBD in previous work, these aptamers did not function reliably as fluorescent nanosensors when adsorbed to SWCNT. It is possible that the addition of polycytosine on the 5'-terminus of the RBD-binding aptamers affected their native secondary structure and furthermore attenuated their affinity for Spike RBD. As a next step, nanosensors should be synthesized via ligand exchange using the original 1C and 4C aptamers. It is also possible that interaction with the SWCNT surface alone induced unfavorable changes in the aptamer secondary structure. ssDNA sequences have been shown to wrap helically around SWCNT[203], and peptides have been shown to spontaneously form hairpin structures when adsorbed to the SWCNT surface even though these biopolymers lack secondary structure in aqueous solution[177]. To address this challenge, the 1C and 4C aptamers can be covalently conjugated to the SWCNT surface via triazine chemistry, as described in Chapter 3. Covalent attachment through a triazine handle may limit aptamer-SWCNT surface interactions and thus maintain aptamer secondary structure.

Should either of these suggested strategies prove successful and consistently produce sensitive and selective Spike RBD nanosensors, this platform could be translated to paper-based testing. Preliminary experiments suggest that SWNCT-based sensors can be immobilized on paper-substrates such as nylon and nitrocellulose while maintaining their fluorescence response to a target analyte. SWCNT-based viral sensors in a paper formfactor may enable inexpensive point-of-care testing with long-term room temperature stability in resource limiting settings.

References

1. Iijima, S., Helical Microtubules of Graphitic Carbon. *Nature* **1991,** *354* (6348), 56-58.

2. Iijima, S.; Ichihashi, T., Single-Shell Carbon Nanotubes of 1-Nm Diameter. *Nature* **1993,** *363* (6430), 603-605.

3. Dresselhaus, M. S.; Dresselhaus, G.; Saito, R., Physics of Carbon Nanotubes. *Carbon* **1995,** *33* (7), 883-891.

4. Inagaki, M.; Kang, F.; Toyoda, M.; Konno, H., Carbon Nanotubes: Synthesis and Formation. In *Advanced Materials Science and Engineering of Carbon*, Inagaki, M.; Kang, F.; Toyoda, M.; Konno, H., Eds. Butterworth-Heinemann: 2014; pp 15-40.

5. Nikolaev, P.; Bronikowski, M. J.; Bradley, R. K.; Rohmund, F.; Colbert, D. T.; Smith, K. A.; Smalley, R. E., Gas-phase catalytic growth of single-walled carbon nanotubes from carbon monoxide. *Chem Phys Lett* **1999,** *313* (1-2), 91-97.

6. Chiang, I. W.; Brinson, B. E.; Huang, A. Y.; Willis, P. A.; Bronikowski, M. J.; Margrave, J. L.; Smalley, R. E.; Hauge, R. H., Purification and characterization of single-wall carbon nanotubes (SWNTs) obtained from the gas-phase decomposition of CO (HiPco process). *Journal of Physical Chemistry B* **2001,** *105* (35), 8297-8301.

7. Zheng, M., Sorting Carbon Nanotubes. *Top Curr Chem (Cham)* **2017,** *375* (1), 13.

8. Yang, F.; Wang, M.; Zhang, D.; Yang, J.; Zheng, M.; Li, Y., Chirality Pure Carbon Nanotubes: Growth, Sorting, and Characterization. *Chem Rev* **2020,** *120* (5), 2693-2758.

9. Wu, Y.; Zhao, X.; Shang, Y.; Chang, S.; Dai, L.; Cao, A., Application-Driven Carbon Nanotube Functional Materials. *ACS Nano* **2021,** *15* (5), 7946-7974.

10. Popov, V. N., Carbon nanotubes: properties and application. *Mat Sci Eng R* **2004,** *43* (3), 61-102.

11. Bachilo, S. M.; Strano, M. S.; Kittrell, C.; Hauge, R. H.; Smalley, R. E.; Weisman, R. B., Structure-assigned optical spectra of single-walled carbon nanotubes. *Science* **2002,** *298* (5602), 2361-2366.

12. O'Connell, M. J.; Bachilo, S. M.; Huffman, C. B.; Moore, V. C.; Strano, M. S.; Haroz, E. H.; Rialon, K. L.; Boul, P. J.; Noon, W. H.; Kittrell, C.; Ma, J.; Hauge, R. H.; Weisman, R. B.; Smalley, R. E., Band gap fluorescence from individual single-walled carbon nanotubes. *Science* **2002,** *297* (5581), 593-6.

13. Boghossian, A. A.; Zhang, J.; Barone, P. W.; Reuel, N. F.; Kim, J. H.; Heller, D. A.; Ahn, J. H.; Hilmer, A. J.; Rwei, A.; Arkalgud, J. R.; Zhang, C. T.; Strano, M. S., Near-infrared fluorescent sensors based on single-walled carbon nanotubes for life sciences applications. *ChemSusChem* **2011,** *4* (7), 848-63.

14. Heller, D. A.; Baik, S.; Eurell, T. E.; Strano, M. S., Single-walled carbon nanotube spectroscopy in live cells: Towards long-term labels and optical sensors. *Adv Mater* **2005,** *17* (23), 2793-+.

15. Dumortier, H.; Lacotte, S.; Pastorin, G.; Marega, R.; Wu, W.; Bonifazi, D.; Briand, J. P.; Prato, M.; Muller, S.; Bianco, A., Functionalized carbon nanotubes are non-cytotoxic and preserve the functionality of primary immune cells. *Nano Lett* **2006,** *6* (7), 1522-8.

16. Galassi, T. V.; Antman-Passig, M.; Yaari, Z.; Jessurun, J.; Schwartz, R. E.; Heller, D. A., Long-term in vivo biocompatibility of single-walled carbon nanotubes. *PLoS One* **2020,** *15* (5), e0226791.

17. Wang, F.; Dukovic, G.; Brus, L. E.; Heinz, T. F., Time-resolved fluorescence of carbon nanotubes and its implication for radiative lifetimes. *Phys Rev Lett* **2004,** *92* (17), 177401.

18. Dresselhaus, M. S.; Dresselhaus, G.; Saito, R.; Jorio, A., Exciton photophysics of carbon nanotubes. *Annu Rev Phys Chem* **2007,** *58*, 719-47.

19. Beyene, A. G.; Delevich, K.; Del Bonis-O'Donnell, J. T.; Piekarski, D. J.; Lin, W. C.; Thomas, A. W.; Yang, S. J.; Kosillo, P.; Yang, D.; Prounis, G. S.; Wilbrecht, L.; Landry, M. P., Imaging striatal dopamine release using a nongenetically encoded near infrared fluorescent catecholamine nanosensor. *Sci Adv* **2019,** *5* (7).

20. Lee, K.; Nojoomi, A.; Jeon, J.; Lee, C. Y.; Yum, K., Near-Infrared Fluorescence Modulation of Refolded DNA Aptamer-Functionalized Single-Walled Carbon Nanotubes for Optical Sensing. *Acs Appl Nano Mater* **2018,** *1* (9), 5327-5336.

21. Landry, M. P.; Vukovic, L.; Kruss, S.; Bisker, G.; Landry, A. M.; Islam, S.; Jain, R.; Schulten, K.; Strano, M. S., Comparative Dynamics and Sequence Dependence of DNA and RNA Binding to Single Walled Carbon Nanotubes. *J Phys Chem C Nanomater Interfaces* **2015,** *119* (18), 10048-10058.

22. Bakota, E. L.; Aulisa, L.; Tsyboulski, D. A.; Weisman, R. B.; Hartgerink, J. D., Multidomain peptides as single-walled carbon nanotube surfactants in cell culture. *Biomacromolecules* **2009,** *10* (8), 2201-6.

23. Zorbas, V.; Smith, A. L.; Xie, H.; Ortiz-Acevedo, A.; Dalton, A. B.; Dieckmann, G. R.; Draper, R. K.; Baughman, R. H.; Musselman, I. H., Importance of aromatic content for peptide/single-walled carbon nanotube interactions. *J Am Chem Soc* **2005,** *127* (35), 12323-8.

24. Setaro, A.; Adeli, M.; Glaeske, M.; Przyrembel, D.; Bisswanger, T.; Gordeev, G.; Maschietto, F.; Faghani, A.; Paulus, B.; Weinelt, M.; Arenal, R.; Haag, R.; Reich, S., Preserving pi-conjugation in covalently functionalized carbon nanotubes for optoelectronic applications. *Nat Commun* **2017,** *8*.

25. Chio, L.; Pinals, R. L.; Murali, A.; Goh, N. S.; Landry, M. P., Covalent Surface Modification Effects on Single-Walled Carbon Nanotubes for Targeted Sensing and Optical Imaging. *Adv Funct Mater* **2020,** *30* (17).

26. Pan, J.; Li, F. R.; Choi, J. H., Single-walled carbon nanotubes as optical probes for bio-sensing and imaging. *J Mater Chem B* **2017,** *5* (32), 6511-6522.

27. US, V. E.; Gaddum, J. H., An unidentified depressor substance in certain tissue extracts. *J Physiol* **1931,** *72* (1), 74-87.

28. Corbiere, A.; Vaudry, H.; Chan, P.; Walet-Balieu, M. L.; Lecroq, T.; Lefebvre, A.; Pineau, C.; Vaudry, D., Strategies for the Identification of Bioactive Neuropeptides in Vertebrates. *Front Neurosci* **2019,** *13*, 948.

29. Hokfelt, T.; Broberger, C.; Xu, Z. Q.; Sergeyev, V.; Ubink, R.; Diez, M., Neuropeptides--an overview. *Neuropharmacology* **2000,** *39* (8), 1337-56.

30. van den Pol, A. N., Neuropeptide transmission in brain circuits. *Neuron* **2012,** *76* (1), 98-115.

31. Hoyle, C. H. V., Neuropeptide families and their receptors: evolutionary perspectives. *Brain Res* **1999,** *848* (1-2), 1-25.

32. Hokfelt, T.; Bartfai, T.; Bloom, F., Neuropeptides: opportunities for drug discovery. *Lancet Neurol* **2003,** *2* (8), 463-72.

33. Nassel, D. R., Neuropeptides in the nervous system of Drosophila and other insects: multiple roles as neuromodulators and neurohormones. *Prog Neurobiol* **2002,** *68* (1), 1-84.

34. Ludwig, M.; Leng, G., Dendritic peptide release and peptide-dependent behaviours. *Nat Rev Neurosci* **2006,** *7* (2), 126-36.

35. Mens, W. B. J.; Witter, A.; Greidanus, T. B. V., Penetration of Neurohypophyseal Hormones from Plasma into Cerebrospinal-Fluid (Csf) - Half-Times of Disappearance of These Neuropeptides from Csf. *Brain Res* **1983,** *262* (1), 143-149.

36. Herkenham, M., Mismatches between neurotransmitter and receptor localizations in brain: observations and implications. *Neuroscience* **1987,** *23* (1), 1-38.

37. Beyene, A. G.; Yang, S. J.; Landry, M. P., Review Article: Tools and trends for probing brain neurochemistry. *J Vac Sci Technol A* **2019,** *37* (4), 040802.

38. Inui, A., Neuropeptide gene polymorphisms and human behavioural disorders. *Nat Rev Drug Discov* **2003,** *2* (12), 986-98.

39. Morton, G. J.; Meek, T. H.; Schwartz, M. W., Neurobiology of food intake in health and disease. *Nat Rev Neurosci* **2014,** *15* (6), 367-78.

40. Brogden, K. A.; Guthmiller, J. M.; Salzet, M.; Zasloff, M., The nervous system and innate immunity: the neuropeptide connection. *Nat Immunol* **2005,** *6* (6), 558-64.

41. Griebel, G.; Holsboer, F., Neuropeptide receptor ligands as drugs for psychiatric diseases: the end of the beginning? *Nature Reviews Drug Discovery* **2012,** *11* (6), 462-478.

42. Sah, R.; Geracioti, T. D., Neuropeptide Y and posttraumatic stress disorder. *Mol Psychiatry* **2013,** *18* (6), 646-55.

43. Davies, P.; Katzman, R.; Terry, R. D., Reduced somatostatin-like immunoreactivity in cerebral cortex from cases of Alzheimer disease and Alzheimer senile dementa. *Nature* **1980,** *288* (5788), 279-80.

44. Song, Y. H.; Yoon, J.; Lee, S. H., The role of neuropeptide somatostatin in the brain and its application in treating neurological disorders. *Exp Mol Med* **2021,** *53* (3), 328-338.

45. Hornberg, H.; Perez-Garci, E.; Schreiner, D.; Hatstatt-Burkle, L.; Magara, F.; Baudouin, S.; Matter, A.; Nacro, K.; Pecho-Vrieseling, E.; Scheiffele, P., Rescue of oxytocin response and social behaviour in a mouse model of autism. *Nature* **2020,** *584* (7820), 252-256.

46. Meyer-Lindenberg, A.; Domes, G.; Kirsch, P.; Heinrichs, M., Oxytocin and vasopressin in the human brain: social neuropeptides for translational medicine. *Nat Rev Neurosci* **2011,** *12* (9), 524-38.

47. Yamasue, H.; Domes, G., Oxytocin and Autism Spectrum Disorders. In *Behavioral Pharmacology of Neuropeptides: Oxytocin*, Hurlemann, R.; Grinevich, V., Eds. Springer International Publishing: Cham, 2018; pp 449-465.

48. Caceda, R.; Kinkead, B.; Nemeroff, C. B., Neurotensin: role in psychiatric and neurological diseases. *Peptides* **2006,** *27* (10), 2385-404.

49. Scanziani, M.; Hausser, M., Electrophysiology in the age of light. *Nature* **2009,** *461* (7266), 930-9.

50. DeLaney, K.; Buchberger, A. R.; Atkinson, L.; Grunder, S.; Mousley, A.; Li, L., New techniques, applications and perspectives in neuropeptide research. *J Exp Biol* **2018,** *221* (Pt 3).

51. Nusbaum, M. P.; Blitz, D. M.; Marder, E., Functional consequences of neuropeptide and small-molecule co-transmission. *Nature Reviews Neuroscience* **2017,** *18* (7), 389-403.

52. Nassel, D. R., Neuropeptide signaling near and far: how localized and timed is the action of neuropeptides in brain circuits? *Invert Neurosci* **2009,** *9* (2), 57-75.

53. Morimoto, R.; Satoh, F.; Murakami, O.; Totsune, K.; Saruta, M.; Suzuki, T.; Sasano, H.; Ito, S.; Takahashi, K., Expression of peptide YY in human brain and pituitary tissues. *Nutrition* **2008,** *24* (9), 878-84.

54. Russo, A. F., Overview of Neuropeptides: Awakening the Senses? *Headache* **2017,** *57*, 37-46.

55. Nordmann, J. J.; Morris, J. F., Method for quantitating the molecular content of a subcellular organelle: hormone and neurophysin content of newly formed and aged neurosecretory granules. *Proc Natl Acad Sci U S A* **1984,** *81* (1), 180-4.

56. Lefevre, A.; Mottolese, R.; Dirheimer, M.; Mottolese, C.; Duhamel, J. R.; Sirigu, A., A comparison of methods to measure central and peripheral oxytocin concentrations in human and non-human primates. *Sci Rep* **2017,** *7* (1), 17222.

57. Poljak, A.; Sachdev, P., The need for a reliable oxytocin assay. *Mol Psychiatry* **2021**.

58. Inutsuka, A.; Ino, D.; Onaka, T., Detection of neuropeptides in vivo and open questions for current and upcoming fluorescent sensors for neuropeptides. *Peptides* **2021,** *136*.

59. McKay, E. C.; Counts, S. E., Oxytocin Receptor Signaling in Vascular Function and Stroke. *Front Neurosci* **2020,** *14*, 574499.

60. Yang, H. H.; St-Pierre, F., Genetically Encoded Voltage Indicators: Opportunities and Challenges. *J Neurosci* **2016,** *36* (39), 9977-89.

61. Svensson, M.; Skold, K.; Svenningsson, P.; Andren, P. E., Peptidomics-based discovery of novel neuropeptides. *J Proteome Res* **2003,** *2* (2), 213-9.

62. Edison, A. S.; Espinoza, E.; Zachariah, C., Conformational ensembles: the role of neuropeptide structures in receptor binding. *J Neurosci* **1999,** *19* (15), 6318-26.

63. Nyberg, F.; Hallberg, M., Localization of neuropeptides by radioimmunoassay. *Methods Mol Biol* **2011,** *789*, 191-201.

64. Allen, R.; Boublik, J.; Hauger, R. L.; Scott, N.; Rivier, J.; Brown, M. R., Neuropeptide Y radioimmunoassay: characterization and application. *Clin Exp Pharmacol Physiol* **1991,** *18* (12), 825-33.

65. Allen, J. M.; Yeats, J. C.; Adrian, T. E.; Bloom, S. R., Radioimmunoassay of neuropeptide Y. *Regul Pept* **1984,** *8* (1), 61-70.

66. Theodorsson-Norheim, E.; Hemsen, A.; Lundberg, J. M., Radioimmunoassay for neuropeptide Y (NPY): chromatographic characterization of immunoreactivity in plasma and tissue extracts. *Scand J Clin Lab Invest* **1985,** *45* (4), 355-65.

67. Allen, Y. S.; Adrian, T. E.; Allen, J. M.; Tatemoto, K.; Crow, T. J.; Bloom, S. R.; Polak, J. M., Neuropeptide Y distribution in the rat brain. *Science* **1983,** *221* (4613), 877-9.

68. Schams, D.; Schmidt-Polex, B.; Kruse, V., Oxytocin determination by radioimmunoassay in cattle. I. Method and preliminary physiological data. *Acta Endocrinol (Copenh)* **1979,** *92* (2), 258-70.

69. Schams, D., Oxytocin determination by radioimmunoassay. III. Improvement to subpicogram sensitivity and application to blood levels in cyclic cattle. *Acta Endocrinol (Copenh)* **1983,** *103* (2), 180-3.

70. Glamsta, E. L.; Morkrid, L.; Lantz, I.; Nyberg, F., Concomitant increase in blood plasma levels of immunoreactive hemorphin-7 and beta-endorphin following long distance running. *Regul Pept* **1993,** *49* (1), 9-18.

71. Hallberg, M.; Johansson, P.; Kindlundh, A. M.; Nyberg, F., Anabolic-androgenic steroids affect the content of substance P and substance P(1-7) in the rat brain. *Peptides* **2000,** *21* (6), 845-52.

72. Massey, S. H.; Backes, K. A.; Schuette, S. A., Plasma Oxytocin Concentration and Depressive Symptoms: A Review of Current Evidence and Directions for Future Research. *Depress Anxiety* **2016,** *33* (4), 316-22.

73. Spanagel, R.; Herz, A.; Shippenberg, T. S., The effects of opioid peptides on dopamine release in the nucleus accumbens: an in vivo microdialysis study. *J Neurochem* **1990,** *55* (5), 1734-40.

74. Maidment, N. T.; Brumbaugh, D. R.; Rudolph, V. D.; Erdelyi, E.; Evans, C. J., Microdialysis of extracellular endogenous opioid peptides from rat brain in vivo. *Neuroscience* **1989,** *33* (3), 549-57.

75. Kendrick, K. M., Microdialysis measurement of in vivo neuropeptide release. *J Neurosci Methods* **1990,** *34* (1-3), 35-46.

76. Chefer, V. I.; Thompson, A. C.; Zapata, A.; Shippenberg, T. S., Overview of brain microdialysis. *Curr Protoc Neurosci* **2009,** *Chapter 7*, Unit7 1.

77. Neumann, I.; Russell, J. A.; Landgraf, R., Oxytocin and vasopressin release within the supraoptic and paraventricular nuclei of pregnant, parturient and lactating rats: a microdialysis study. *Neuroscience* **1993,** *53* (1), 65-75.

78. Al-Hasani, R.; Wong, J. T.; Mabrouk, O. S.; McCall, J. G.; Schmitz, G. P.; Porter-Stransky, K. A.; Aragona, B. J.; Kennedy, R. T.; Bruchas, M. R., In vivo detection of optically-evoked opioid peptide release. *Elife* **2018,** *7*.

79. Kushikata, T.; Hirota, K., Neuropeptide microdialysis in free-moving animals. *Methods Mol Biol* **2011,** *789*, 261-9.

80. Jaquins-Gerstl, A.; Michael, A. C., A review of the effects of FSCV and microdialysis measurements on dopamine release in the surrounding tissue. *Analyst* **2015,** *140* (11), 3696-708.

81. Sandberg, M.; Weber, S. G., Techniques for neuropeptide determination. *Trends Analyt Chem* **2003,** *22* (8), 522-527.

82. Rafi, H.; Zestos, A. G., Review-Recent Advances in FSCV Detection of Neurochemicals via Waveform and Carbon Microelectrode Modification. *J Electrochem Soc* **2021,** *168* (5).

83. Sames, D.; Dunn, M.; Karpowicz, R. J., Jr.; Sulzer, D., Visualizing neurotransmitter secretion at individual synapses. *ACS Chem Neurosci* **2013,** *4* (5), 648-51.

84. Lacin, E.; Muller, A.; Fernando, M.; Kleinfeld, D.; Slesinger, P. A., Construction of Cell-based Neurotransmitter Fluorescent Engineered Reporters (CNiFERs) for Optical Detection of Neurotransmitters In Vivo. *J Vis Exp* **2016,** (111).

85. Ding, K.; Han, Y.; Seid, T. W.; Buser, C.; Karigo, T.; Zhang, S.; Dickman, D. K.; Anderson, D. J., Imaging neuropeptide release at synapses with a genetically engineered reporter. *Elife* **2019,** *8*.

86. Chen, T. W.; Wardill, T. J.; Sun, Y.; Pulver, S. R.; Renninger, S. L.; Baohan, A.; Schreiter, E. R.; Kerr, R. A.; Orger, M. B.; Jayaraman, V.; Looger, L. L.; Svoboda, K.; Kim, D. S., Ultrasensitive fluorescent proteins for imaging neuronal activity. *Nature* **2013,** *499* (7458), 295-300.

87. Wang, H.; Jing, M.; Li, Y., Lighting up the brain: genetically encoded fluorescent sensors for imaging neurotransmitters and neuromodulators. *Curr Opin Neurobiol* **2018,** *50*, 171-178.

88. Palmer, A. E.; Qin, Y.; Park, J. G.; McCombs, J. E., Design and application of genetically encoded biosensors. *Trends Biotechnol* **2011,** *29* (3), 144-52.

89. Lin, L.; Gupta, S.; Zheng, W. S.; Si, K.; Zhu, J. J., Genetically encoded sensors enable micro- and nano-scopic decoding of transmission in healthy and diseased brains. *Mol Psychiatry* **2021,** *26* (2), 443-455.

90. Bi, X.; Beck, C.; Gong, Y., Genetically Encoded Fluorescent Indicators for Imaging Brain Chemistry. *Biosensors (Basel)* **2021,** *11* (4).

91. Nasu, Y.; Shen, Y.; Kramer, L.; Campbell, R. E., Structure- and mechanism-guided design of single fluorescent protein-based biosensors. *Nat Chem Biol* **2021,** *17* (5), 509-518.

92. Liang, R.; Broussard, G. J.; Tian, L., Imaging chemical neurotransmission with genetically encoded fluorescent sensors. *ACS Chem Neurosci* **2015,** *6* (1), 84-93.

93. Okumoto, S.; Looger, L. L.; Micheva, K. D.; Reimer, R. J.; Smith, S. J.; Frommer, W. B., Detection of glutamate release from neurons by genetically encoded surface-displayed FRET nanosensors. *Proc Natl Acad Sci U S A* **2005,** *102* (24), 8740-5.

94. Masharina, A.; Reymond, L.; Maurel, D.; Umezawa, K.; Johnsson, K., A fluorescent sensor for GABA and synthetic GABA(B) receptor ligands. *J Am Chem Soc* **2012,** *134* (46), 19026-34.

95. Marvin, J. S.; Shimoda, Y.; Magloire, V.; Leite, M.; Kawashima, T.; Jensen, T. P.; Kolb, I.; Knott, E. L.; Novak, O.; Podgorski, K.; Leidenheimer, N. J.; Rusakov, D. A.; Ahrens, M. B.; Kullmann, D. M.; Looger, L. L., A genetically encoded fluorescent sensor for in vivo imaging of GABA. *Nat Methods* **2019,** *16* (8), 763-770.

96. Sun, F.; Zeng, J.; Jing, M.; Zhou, J.; Feng, J.; Owen, S. F.; Luo, Y.; Li, F.; Wang, H.; Yamaguchi, T.; Yong, Z.; Gao, Y.; Peng, W.; Wang, L.; Zhang, S.; Du, J.; Lin, D.; Xu, M.; Kreitzer, A. C.; Cui, G.; Li, Y., A Genetically Encoded Fluorescent Sensor Enables Rapid and Specific Detection of Dopamine in Flies, Fish, and Mice. *Cell* **2018,** *174* (2), 481-496 e19.

97. Patriarchi, T.; Cho, J. R.; Merten, K.; Howe, M. W.; Marley, A.; Xiong, W. H.; Folk, R. W.; Broussard, G. J.; Liang, R.; Jang, M. J.; Zhong, H.; Dombeck, D.; von Zastrow, M.; Nimmerjahn, A.; Gradinaru, V.; Williams, J. T.; Tian, L., Ultrafast neuronal imaging of dopamine dynamics with designed genetically encoded sensors. *Science* **2018,** *360* (6396).

98. Jing, M.; Zhang, P.; Wang, G.; Feng, J.; Mesik, L.; Zeng, J.; Jiang, H.; Wang, S.; Looby, J. C.; Guagliardo, N. A.; Langma, L. W.; Lu, J.; Zuo, Y.; Talmage, D. A.; Role, L. W.; Barrett, P. Q.; Zhang, L. I.; Luo, M.; Song, Y.; Zhu, J. J.; Li, Y., A genetically encoded fluorescent acetylcholine indicator for in vitro and in vivo studies. *Nat Biotechnol* **2018,** *36* (8), 726-737.

99. Wan, J.; Peng, W.; Li, X.; Qian, T.; Song, K.; Zeng, J.; Deng, F.; Hao, S.; Feng, J.; Zhang, P.; Zhang, Y.; Zou, J.; Pan, S.; Shin, M.; Venton, B. J.; Zhu, J. J.; Jing, M.; Xu, M.; Li, Y., A genetically encoded sensor for measuring serotonin dynamics. *Nat Neurosci* **2021,** *24* (5), 746-752.

100. Duffet, L.; Kosar, S.; Panniello, M.; Viberti, B.; Bracey, E.; Zych, A. D.; Radoux-Mergault, A.; Zhou, X.; Dernic, J.; Ravotto, L.; Tsai, Y. C.; Figueiredo, M.; Tyagarajan, S. K.; Weber, B.; Stoeber, M.; Gogolla, N.; Schmidt, M. H.; Adamantidis, A. R.; Fellin, T.; Burdakov, D.; Patriarchi, T., A genetically encoded sensor for in vivo imaging of orexin neuropeptides. *Nat Methods* **2022,** *19* (2), 231-241.

101. Mignocchi, N.; Krüssel, S.; Jung, K.; Lee, D.; Kwon, H.-B., Development of a genetically-encoded oxytocin sensor. *bioRxiv* **2020**, 2020.07.14.202598.

102. Qian, T.; Wang, H.; Wang, P.; Geng, L.; Mei, L.; Osakada, T.; Tang, Y.; Kania, A.; Grinevich, V.; Stoop, R.; Lin, D.; Luo, M.; Li, Y., Compartmental Neuropeptide Release Measured Using a New Oxytocin Sensor. *bioRxiv* **2022**, 2022.02.10.480016.

103. Wang, H.; Qian, T.; Zhao, Y.; Zhuo, Y.; Wu, C.; Osakada, T.; Chen, P.; Ren, H.; Yan, Y.; Geng, L.; Fu, S.; Mei, L.; Li, G.; Wu, L.; Jiang, Y.; Qian, W.; Peng, W.; Xu, M.; Hu, J.; Chen, L.; Tang, C.; Lin, D.; Zhou, J.-N.; Li, Y., A toolkit of highly selective and sensitive genetically encoded neuropeptide sensors. *bioRxiv* **2022**, 2022.03.26.485911.

104. Maiti, D.; Tong, X.; Mou, X.; Yang, K., Carbon-Based Nanomaterials for Biomedical Applications: A Recent Study. *Front Pharmacol* **2018,** *9*, 1401.

105. Ramos, A. P.; Cruz, M. A. E.; Tovani, C. B.; Ciancaglini, P., Biomedical applications of nanotechnology. *Biophys Rev* **2017,** *9* (2), 79-89.

106. Huynh, K. H.; Lee, K. Y.; Chang, H.; Lee, S. H.; Kim, J.; Pham, X. H.; Lee, Y. S.; Rho, W. Y.; Jun, B. H., Bioapplications of Nanomaterials. *Adv Exp Med Biol* **2021,** *1309*, 235-255.

107. Altinoglu, E. I.; Adair, J. H., Near infrared imaging with nanoparticles. *Wiley Interdiscip Rev Nanomed Nanobiotechnol* **2010,** *2* (5), 461-77.

108. Demchenko, A. P., Nanoparticles and nanocomposites for fluorescence sensing and imaging. *Methods Appl Fluoresc* **2013,** *1* (2), 022001.

109. Luo, X. L.; Morrin, A.; Killard, A. J.; Smyth, M. R., Application of nanoparticles in electrochemical sensors and biosensors. *Electroanal* **2006,** *18* (4), 319-326.

110. Mayer, K. M.; Hafner, J. H., Localized Surface Plasmon Resonance Sensors. *Chem Rev* **2011,** *111* (6), 3828-3857.

111. Mann, F. A.; Herrmann, N.; Meyer, D.; Kruss, S., Tuning Selectivity of Fluorescent Carbon Nanotube-Based Neurotransmitter Sensors. *Sensors-Basel* **2017,** *17* (7).

112. Tajik, S.; Dourandish, Z.; Zhang, K.; Beitollahi, H.; Le, Q. V.; Jang, H. W.; Shokouhimehr, M., Carbon and graphene quantum dots: a review on syntheses, characterization, biological and sensing applications for neurotransmitter determination. *Rsc Adv* **2020,** *10* (26), 15406-15429.

113. Niyonambaza, S. D.; Kumar, P.; Xing, P.; Mathault, J.; De Koninck, P.; Boisselier, E.; Boukadoum, M.; Miled, A., A Review of Neurotransmitters Sensing Methods for Neuro-Engineering Research. *Appl Sci-Basel* **2019,** *9* (21).

114. Chavez, J. L.; Rieger, K.; Hagen, J. A.; Kelley-Loughnane, N., Biosensor platforms for biomarker detection: plasmonic aptasensors for detection of Neuropeptide Y. *Proc Spie* **2019,** *11020*.

115. Abdallah, M. G.; Buchanan-Vega, J. A.; Lee, K. J.; Wenner, B. R.; Allen, J. W.; Allen, M. S.; Gimlin, S.; Weidanz, D. W.; Magnusson, R., Quantification of Neuropeptide Y with Picomolar Sensitivity Enabled by Guided-Mode Resonance Biosensors. *Sensors-Basel* **2020,** *20* (1).

116. Azzouz, A.; Goud, K. Y.; Raza, N.; Ballesteros, E.; Lee, S. E.; Hong, J.; Deep, A.; Kim, K. H., Nanomaterial-based electrochemical sensors for the detection of neurochemicals in biological matrices. *Trac-Trend Anal Chem* **2019,** *110*, 15-34.

117. Kim, D.; Lee, Y. D.; Jo, S.; Kim, S.; Lee, T. S., Detection and imaging of cathepsin L in cancer cells using the aggregation of conjugated polymer dots and magnetic nanoparticles. *Sensor Actuat B-Chem* **2020,** *307*.

118. Del Bonis-O'Donnell, J. T.; Mun, J.; Delevich, K.; Landry, M. P., Synthetic nanosensors for imaging neuromodulators. *J Neurosci Meth* **2021,** *363*.

119. Kruss, S.; Salem, D. P.; Vukovic, L.; Lima, B.; Vander Ende, E.; Boyden, E. S.; Strano, M. S., High-resolution imaging of cellular dopamine efflux using a fluorescent nanosensor array. *P Natl Acad Sci USA* **2017,** *114* (8), 1789-1794.

120. Jeong, S.; Yang, D.; Beyene, A. G.; Del Bonis-O'Donnell, J. T.; Gest, A. M. M.; Navarro, N.; Sun, X.; Landry, M. P., High-throughput evolution of near-infrared serotonin nanosensors. *Sci Adv* **2019,** *5* (12), eaay3771.

121. Rao, J. H.; Dragulescu-Andrasi, A.; Yao, H. Q.; Yao, H. Q., Fluorescence imaging in vivo: recent advances. *Curr Opin Biotech* **2007,** *18* (1), 17-25.

122. So, M. K.; Xu, C. J.; Loening, A. M.; Gambhir, S. S.; Rao, J. H., Self-illuminating quantum dot conjugates for in vivo imaging. *Nature Biotechnology* **2006,** *24* (3), 339-343.

123. Navarro, N.; Jeong, S.; Ouassil, N.; Mun, J.; Leem, E.; Landry, M. P., Near Infrared Nanosensors Enable Optical Imaging of Oxytocin with Selectivity over Vasopressin in Acute Mouse Brain Slices. *bioRxiv* **2022**, 2022.10.05.511026.

124. Du Vigneaud, V.; Ressler, C.; Trippett, S., The sequence of amino acids in oxytocin, with a proposal for the structure of oxytocin. *J Biol Chem* **1953,** *205* (2), 949-57.

125. Donaldson, Z. R.; Young, L. J., Oxytocin, vasopressin, and the neurogenetics of sociality. *Science* **2008,** *322* (5903), 900-4.

126. Grinevich, V.; Ludwig, M., The multiple faces of the oxytocin and vasopressin systems in the brain. *J Neuroendocrinol* **2021**, e13004.

127. Heinrichs, M.; von Dawans, B.; Domes, G., Oxytocin, vasopressin, and human social behavior. *Front Neuroendocrinol* **2009,** *30* (4), 548-557.

128. Dantzer, R.; Bluthe, R. M.; Koob, G. F.; Le Moal, M., Modulation of social memory in male rats by neurohypophyseal peptides. *Psychopharmacology (Berl)* **1987,** *91* (3), 363-8.

129. Winslow, J. T.; Insel, T. R., Neuroendocrine basis of social recognition. *Curr Opin Neurobiol* **2004,** *14* (2), 248-53.

130. Young, L. J.; Wang, Z., The neurobiology of pair bonding. *Nat Neurosci* **2004,** *7* (10), 1048-54.

131. McCarthy, M. M.; McDonald, C. H.; Brooks, P. J.; Goldman, D., An anxiolytic action of oxytocin is enhanced by estrogen in the mouse. *Physiol Behav* **1996,** *60* (5), 1209-1215.

132. Kirsch, P.; Esslinger, C.; Chen, Q.; Mier, D.; Lis, S.; Siddhanti, S.; Gruppe, H.; Mattay, V. S.; Gallhofer, B.; Meyer-Lindenberg, A., Oxytocin modulates neural circuitry for social cognition and fear in humans. *J Neurosci* **2005,** *25* (49), 11489-93.

133. Labuschagne, I.; Phan, K. L.; Wood, A.; Angstadt, M.; Chua, P.; Heinrichs, M.; Stout, J. C.; Nathan, P. J., Oxytocin attenuates amygdala reactivity to fear in generalized social anxiety disorder. *Neuropsychopharmacology* **2010,** *35* (12), 2403-13.

134. Dodhia, S.; Hosanagar, A.; Fitzgerald, D. A.; Labuschagne, I.; Wood, A. G.; Nathan, P. J.; Phan, K. L., Modulation of resting-state amygdala-frontal functional connectivity by oxytocin in generalized social anxiety disorder. *Neuropsychopharmacology* **2014,** *39* (9), 2061-9.

135. Sundaram, S. M.; Schwaninger, M., Parvocellular Oxytocin Neurons and Autism Spectrum Disorders. *Trends Endocrinol Metab* **2021,** *32* (4), 195-197.

136. Young, L. J.; Barrett, C. E., Can oxytocin treat autism? *Science* **2015,** *347* (6224), 825-826.

137. MacLean, E. L.; Gesquiere, L. R.; Gee, N.; Levy, K.; Martin, W. L.; Carter, C. S., Validation of salivary oxytocin and vasopressin as biomarkers in domestic dogs. *J Neurosci Meth* **2018,** *293*, 67-76.

138. Howe, M. W.; Tierney, P. L.; Sandberg, S. G.; Phillips, P. E.; Graybiel, A. M., Prolonged dopamine signalling in striatum signals proximity and value of distant rewards. *Nature* **2013,** *500* (7464), 575-9.

139. Asai, K.; Ivandini, T. A.; Einaga, Y., Continuous and selective measurement of oxytocin and vasopressin using boron-doped diamond electrodes. *Sci Rep* **2016,** *6*, 32429.

140. Waltenspuhl, Y.; Schoppe, J.; Ehrenmann, J.; Kummer, L.; Pluckthun, A., Crystal structure of the human oxytocin receptor. *Sci Adv* **2020,** *6* (29), eabb5419.

141. Lee, D.; Kwon, H. B., Current and future techniques for detecting oxytocin: Focusing on genetically-encoded GPCR sensors. *J Neurosci Methods* **2022,** *366*, 109407.

142. Zhang, J. Q.; Landry, M. P.; Barone, P. W.; Kim, J. H.; Lin, S. C.; Ulissi, Z. W.; Lin, D. H.; Mu, B.; Boghossian, A. A.; Hilmer, A. J.; Rwei, A.; Hinckley, A. C.; Kruss, S.; Shandell, M. A.; Nair, N.; Blake, S.; Sen, F.; Sen, S.; Croy, R. G.; Li, D. Y.; Yum, K.; Ahn, J. H.; Jin, H.; Heller, D. A.; Essigmann, J. M.; Blankschtein, D.; Strano, M. S., Molecular recognition using corona phase complexes made of synthetic polymers adsorbed on carbon nanotubes. *Nat Nanotechnol* **2013,** *8* (12), 959-968.

143. Yang, S. J.; Del Bonis-O'Donnell, J. T.; Beyene, A. G.; Landry, M. P., Near-infrared catecholamine nanosensors for high spatiotemporal dopamine imaging. *Nat Protoc* **2021,** *16* (6), 3026-3048.

144. Bulumulla, C.; Krasley, A. T.; Cristofori-Armstrong, B.; Valinsky, W. C.; Walpita, D.; Ackerman, D.; Clapham, D. E.; Beyene, A. G., Visualizing synaptic dopamine efflux with a 2D composite nanofilm. *Elife* **2022,** *11*.

145. Suzuki, Y., Development of a fluorescent peptide for the highly sensitive and selective detection of oxytocin. *Sensor Actuat B-Chem* **2018,** *254*, 321-328.

146. Godin, A. G.; Setaro, A.; Gandil, M.; Haag, R.; Adeli, M.; Reich, S.; Cognet, L., Photoswitchable single-walled carbon nanotubes for super-resolution microscopy in the near-infrared. *Sci Adv* **2019,** *5* (9).

147. Landry, M. P.; Vukovic, L.; Kruss, S.; Bisker, G.; Landry, A. M.; Islam, S.; Jain, R.; Schulten, K.; Strano, M. S., Comparative Dynamics and Sequence Dependence of DNA and RNA Binding to Single Walled Carbon Nanotubes. *J Phys Chem C* **2015,** *119* (18), 10048-10058.

148. Long, G. L.; Winefordner, J. D., Limit of Detection. *Anal Chem* **1983,** *55* (7), A712-+.

149. Pinals, R. L.; Ledesma, F.; Yang, D. W.; Navarro, N.; Jeong, S.; Pak, J. E.; Kuo, L. L.; Chuang, Y. C.; Cheng, Y. W.; Sun, H. Y.; Landry, M. P., Rapid SARS-CoV-2 Spike Protein Detection by Carbon Nanotube-Based Near-Infrared Nanosensors. *Nano Letters* **2021,** *21* (5), 2272-2280.

150. Winokur, A.; Utiger, R. D., Thyrotropin-Releasing-Hormone - Regional Distribution in Rat-Brain. *Science* **1974,** *185* (4147), 265-267.

151. Kadar, A.; Sanchez, E.; Wittmann, G.; Singru, P. S.; Fuzesi, T.; Marsili, A.; Larsen, P. R.; Liposits, Z.; Lechan, R. M.; Fekete, C., Distribution of hypophysiotropic thyrotropin-releasing hormone (TRH)-synthesizing neurons in the hypothalamic paraventricular nucleus of the mouse. *J Comp Neurol* **2010,** *518* (19), 3948-61.

152. Engstrom, T.; Barth, T.; Melin, P.; Vilhardt, H., Oxytocin receptor binding and uterotonic activity of carbetocin and its metabolites following enzymatic degradation. *Eur J Pharmacol* **1998,** *355* (2-3), 203-10.

153. Postina, R.; Kojro, E.; Fahrenholz, F., Separate agonist and peptide antagonist binding sites of the oxytocin receptor defined by their transfer into the V2 vasopressin receptor. *J Biol Chem* **1996,** *271* (49), 31593-601.

154. Duvigneaud, V.; Lawler, H. C.; Popenoe, E. A., Enzymatic Cleavage of Glycinamide from Vasopressin and a Proposed Structure for This Pressor-Antidiuretic Hormone of the Posterior Pituitary. *J Am Chem Soc* **1953,** *75* (19), 4880-4881.

155. Piekarski, D. J.; Boivin, J. R.; Wilbrecht, L., Ovarian Hormones Organize the Maturation of Inhibitory Neurotransmission in the Frontal Cortex at Puberty Onset in Female Mice. *Curr Biol* **2017,** *27* (12), 1735-+.

156. Godin, A. G.; Varela, J. A.; Gao, Z.; Danne, N.; Dupuis, J. P.; Lounis, B.; Groc, L.; Cognet, L., Single-nanotube tracking reveals the nanoscale organization of the extracellular space in the live brain. *Nat Nanotechnol* **2017,** *12* (3), 238-243.

157. Grinevich, V.; Ludwig, M., The multiple faces of the oxytocin and vasopressin systems in the brain. *J Neuroendocrinol* **2021,** *33* (11), e13004.

158. Hattori, T.; Sundberg, D. K.; Morris, M., Central and systemic oxytocin release: a study of the paraventricular nucleus by in vivo microdialysis. *Brain Res Bull* **1992,** *28* (2), 257-63.

159. Vaidyanathan, R.; Hammock, E. A. D., Oxytocin receptor gene loss influences expression of the oxytocin gene in C57BL/6J mice in a sex- and age-dependent manner. *J Neuroendocrinol* **2020,** *32* (2), e12821.

160. Althammer, F.; Grinevich, V., Diversity of oxytocin neurones: Beyond magno- and parvocellular cell types? *Journal of Neuroendocrinology* **2018,** *30* (8).

161. Kim, S. H.; Riaposova, L.; Ahmed, H.; Pohl, O.; Chollet, A.; Gotteland, J. P.; Hanyaloglu, A.; Bennett, P. R.; Terzidou, V., Oxytocin Receptor Antagonists, Atosiban and Nolasiban, Inhibit Prostaglandin F-2 alpha-induced Contractions and Inflammatory Responses in Human Myometrium. *Sci Rep-Uk* **2019,** *9*.

162. Jurek, B.; Slattery, D. A.; Hiraoka, Y.; Liu, Y.; Nishimori, K.; Aguilera, G.; Neumann, I. D.; van den Burg, E. H., Oxytocin Regulates Stress-Induced Crf Gene Transcription through CREB-Regulated Transcription Coactivator 3. *J Neurosci* **2015,** *35* (35), 12248-60.

163. Escobar, A. P.; Cornejo, F. A.; Olivares-Costa, M.; Gonzalez, M.; Fuentealba, J. A.; Gysling, K.; Espana, R. A.; Andres, M. E., Reduced dopamine and glutamate neurotransmission in the nucleus accumbens of quinpirole-sensitized rats hints at inhibitory D2 autoreceptor function. *J Neurochem* **2015,** *134* (6), 1081-90.

164. Tanaka, T.; Vincent, S. R.; Nomikos, G. G.; Fibiger, H. C., Effect of quinine on autoreceptor-regulated dopamine release in the rat striatum. *J Neurochem* **1992,** *59* (5), 1640-5.

165. Beyene, A. G.; Demirer, G. S.; Landry, M. P., Nanoparticle-Templated Molecular Recognition Platforms for Detection of Biological Analytes. *Curr Protoc Chem Biol* **2016,** *8* (3), 197-223.

166. Edelstein, A. D.; Tsuchida, M. A.; Amodaj, N.; Pinkard, H.; Vale, R. D.; Stuurman, N., Advanced methods of microscope control using muManager software. *J Biol Methods* **2014,** *1* (2).

167. Bosch, O. J.; Dabrowska, J.; Modi, M. E.; Johnson, Z. V.; Keebaugh, A. C.; Barrett, C. E.; Ahern, T. H.; Guo, J. D.; Grinevich, V.; Rainnie, D. G.; Neumann, I. D.; Young, L. J., Oxytocin in the nucleus accumbens shell reverses CRFR2-evoked passive stress-coping after partner loss in monogamous male prairie voles. *Psychoneuroendocrino* **2016,** *64*, 66-78.

168. Landgraf, R.; Neumann, I.; Schwarzberg, H., Central and Peripheral Release of Vasopressin and Oxytocin in the Conscious Rat after Osmotic Stimulation. *Brain Res* **1988,** *457* (2), 219-225.

169. Neumann, I.; Landgraf, R., Septal and Hippocampal Release of Oxytocin, but Not Vasopressin, in the Conscious Lactating Rat during Suckling. *Journal of Neuroendocrinology* **1989,** *1* (4), 305-308.

170. McNamara, C. G.; Dupret, D., Two sources of dopamine for the hippocampus. *Trends in Neurosciences* **2017,** *40* (7), 383-384.

171. Garris, P. A.; Kilpatrick, M.; Bunin, M. A.; Michael, D.; Walker, Q. D.; Wightman, R. M., Dissociation of dopamine release in the nucleus accumbens from intracranial self-stimulation. *Nature* **1999,** *398* (6722), 67-69.

172. Jurek, B.; Neumann, I. D., The Oxytocin Receptor: From Intracellular Signaling to Behavior. *Physiol Rev* **2018,** *98* (3), 1805-1908.

173. Liu, Y.; Wang, Z. X., Nucleus accumbens oxytocin and dopamine interact to regulate pair bond formation in female prairie voles. *Neuroscience* **2003,** *121* (3), 537-544.

174. Kruss, S.; Landry, M.; Vander Ende, E.; Lima, B.; Reuel, N. F.; Zhang, J. Q.; Bin Mu, J. N.; Hilmer, A.; Strano, M. S., Neurotransmitter detection using corona phase molecular recognition on fluorescent single-walled carbon nanotube sensors. *Abstr Pap Am Chem S* **2014,** *248*.

175. Li, Z.; Kameda, T.; Isoshima, T.; Kobatake, E.; Tanaka, T.; Ito, Y.; Kawamoto, M., Solubilization of Single-Walled Carbon Nanotubes Using a Peptide Aptamer in Water below the Critical Micelle Concentration. *Langmuir* **2015,** *31* (11), 3482-3488.

176. Hirano, A.; Tanaka, T.; Kataura, H.; Kameda, T., Arginine Side Chains as a Dispersant for Individual Single-Wall Carbon Nanotubes. *Chem-Eur J* **2014,** *20* (17), 4922-4930.

177. Su, Z. D.; Leung, T.; Honek, J. F., Conformational selectivity of peptides for single-walled carbon nanotubes. *Journal of Physical Chemistry B* **2006,** *110* (47), 23623-23627.

178. Wang, S. Q.; Humphreys, E. S.; Chung, S. Y.; Delduco, D. F.; Lustig, S. R.; Wang, H.; Parker, K. N.; Rizzo, N. W.; Subramoney, S.; Chiang, Y. M.; Jagota, A., Peptides with selective affinity for carbon nanotubes. *Nat Mater* **2003,** *2* (3), 196-200.

179. Li, Z.; Uzawa, T.; Tanaka, T.; Hida, A.; Ishibashi, K.; Katakura, H.; Kobatake, E.; Ito, Y., In vitro selection of peptide aptamers with affinity to single-wall carbon nanotubes using a ribosome display. *Biotechnol Lett* **2013,** *35* (1), 39-45.

180. Samarajeewa, D. R.; Dieckmann, G. R.; Nielsen, S. O.; Musselman, I. H., Doping single-walled carbon nanotubes with surfactant peptides containing electron-donor substituents and nitrogen heterocycles. *Carbon* **2013,** *57*, 88-98.

181. Su, Z.; Mui, K.; Daub, E.; Leung, T.; Honek, J., Single-walled carbon nanotube binding peptides: probing tryptophan's importance by unnatural amino acid substitution. *J Phys Chem B* **2007,** *111* (51), 14411-7.

182. Freda, S. N.; Priest, M. F.; Badong, D.; Xiao, L.; Liu, Y.; Kozorovitskiy, Y., Brainwide input-output architecture of paraventricular oxytocin and vasopressin neurons. *bioRxiv* **2022**, 2022.01.17.476652.

183. Quintana, D. S.; Lischke, A.; Grace, S.; Scheele, D.; Ma, Y. N.; Becker, B., Advances in the field of intranasal oxytocin research: lessons learned and future directions for clinical research. *Mol Psychiatr* **2021,** *26* (1), 80-91.

184. Onaka, T.; Takayanagi, Y., The oxytocin system and early-life experience-dependent plastic changes. *J Neuroendocrinol* **2021,** *33* (11), e13049.

185. Hammock, E. A., Developmental perspectives on oxytocin and vasopressin. *Neuropsychopharmacology* **2015,** *40* (1), 24-42.

186. Kelich, P.; Jeong, S.; Navarro, N.; Adams, J.; Sun, X.; Zhao, H.; Landry, M. P.; Vukovic, L., Discovery of DNA-Carbon Nanotube Sensors for Serotonin with Machine Learning and Near-infrared Fluorescence Spectroscopy. *ACS Nano* **2021**.

187. Ellington, A. D.; Szostak, J. W., In vitro selection of RNA molecules that bind specific ligands. *Nature* **1990,** *346* (6287), 818-22.

188. Tuerk, C.; Gold, L., Systematic evolution of ligands by exponential enrichment: RNA ligands to bacteriophage T4 DNA polymerase. *Science* **1990,** *249* (4968), 505-10.

189. Acinas, S. G.; Sarma-Rupavtarm, R.; Klepac-Ceraj, V.; Polz, M. F., PCR-induced sequence artifacts and bias: insights from comparison of two 16S rRNA clone libraries constructed from the same sample. *Appl Environ Microbiol* **2005,** *71* (12), 8966-9.

190. Tu, X.; Manohar, S.; Jagota, A.; Zheng, M., DNA sequence motifs for structure-specific recognition and separation of carbon nanotubes. *Nature* **2009,** *460* (7252), 250-3.

191. Sefah, K.; Shangguan, D.; Xiong, X. L.; O'Donoghue, M. B.; Tan, W. H., Development of DNA aptamers using Cell-SELEX. *Nature Protocols* **2010,** *5* (6), 1169-1185.

192. Ditzler, M. A.; Lange, M. J.; Bose, D.; Bottoms, C. A.; Virkler, K. F.; Sawyer, A. W.; Whatley, A. S.; Spollen, W.; Givan, S. A.; Burke, D. H., High-throughput sequence analysis reveals structural diversity and improved potency among RNA inhibitors of HIV reverse transcriptase. *Nucleic Acids Res* **2013,** *41* (3), 1873-1884.

193. Alam, K. K.; Chang, J. L.; Burke, D. H., FASTAptamer: A Bioinformatic Toolkit for High-throughput Sequence Analysis of Combinatorial Selections. *Mol Ther-Nucl Acids* **2015,** *4*.

194. WHO Coronavirus (COVID-19) Dashboard. https://covid19.who.int (accessed October 24 2022).

195. Sheridan, C., Coronavirus and the race to distribute reliable diagnostics. *Nat Biotechnol* **2020,** *38* (4), 382-384.

196. Mercer, T. R.; Salit, M., Testing at scale during the COVID-19 pandemic. *Nat Rev Genet* **2021,** *22* (7), 415-426.

197. Mina, M. J.; Andersen, K. G., COVID-19 testing: One size does not fit all. *Science* **2021,** *371* (6525), 126-127.

198. Coronavirus (COVID-19) Update: FDA Authorizes Antigen Test as First Over-the-Counter Fully At-Home Diagnostic Test for COVID-19. https://www.fda.gov/news-events/press-announcements/coronavirus-covid-19-update-fda-authorizes-antigen-test-first-over-counter-fully-home-diagnostic (accessed October 24 2022).

199. Song, Y. L.; Song, J.; Wei, X. Y.; Huang, M. J.; Sun, M.; Zhu, L.; Lin, B. Q.; Shen, H. C.; Zhu, Z.; Yang, C. Y., Discovery of Aptamers Targeting the Receptor-Binding Domain of the SARS-CoV-2 Spike Glycoprotein. *Anal Chem* **2020,** *92* (14), 9895-9900.

200. Bar-On, Y. M.; Flamholz, A.; Phillips, R.; Milo, R., SARS-CoV-2 (COVID-19) by the numbers. *Elife* **2020,** *9*.

201. Jeng, E. S.; Moll, A. E.; Roy, A. C.; Gastala, J. B.; Strano, M. S., Detection of DNA hybridization using the near-infrared band-gap fluorescence of single-walled carbon nanotubes. *Nano Lett* **2006,** *6* (3), 371-375.

202. Lin, S.; Blankschtein, D., Role of the bile salt surfactant sodium cholate in enhancing the aqueous dispersion stability of single-walled carbon nanotubes: a molecular dynamics simulation study. *J Phys Chem B* **2010,** *114* (47), 15616-25.

203. Gigliotti, B.; Sakizzie, B.; Bethune, D. S.; Shelby, R. M.; Cha, J. N., Sequence-independent helical wrapping of single-walled carbon nanotubes by long genomic DNA. *Nano Lett* **2006,** *6* (2), 159-64.